Tôhoku Geophys. Journ. (Sci. Rep. Tôhoku Univ., Ser. 5), Vol. 37, No. 1, pp. 1-89, 2005

Development of the observation system for the Jovian synchrotron radiation using an aperture synthesis array

TAKUO WATANABE[1], HIROAKI MISAWA[1], FUMINORI TSUCHIYA[1], YOSHIZUMI MIYOSHI[1,2], TOSHIHIRO ABE[1] and AKIRA MORIOKA[1]

(Received February 17, 2005; accepted February 28, 2005)

Abstract: The Jovian synchrotron radiation (JSR) and its variation have important information on the acceleration, transport, and loss processes of the relativistic electrons in the Jovian inner magnetosphere. Thus, JSR is a favorable tool for the ground-based remote-sensing of Jovian radiation belt, which can not be obtained by in-situ observation because of the radiation damage of spacecraft. The Jovian synchrotron radiation shows three kinds of variations; (a) long-term (11 year), (b) medium-term (month), and (c) short-term (days to weeks). The medium and short-term time variations are not studied well because of the lack of continuous observation. We have developed the observation system to attain the continuous grand-based observation of JSR. The concept of the development is to achieve the optimized and exclusive system for the JSR observation. The system is designed to detect the Jovian synchrotron radiation with sufficient sensitivity. The developed system consists of following 5 units; (1) 9 antennas arranged in the Y formation, each of which consists of 4×2 stacked 27-element cross Yagi antenna, (2) front-end unit with low receiver noise-temperature of about 90 K which is achieved by using a low noise device of GaAs FET, (3) back-end whose function is to down-convert the RF signal to IF signal, and to process the detected data, (4) loop-method calibration system, which calibrates relative phase and gain of signal synthesizing system, and (5) units of antenna control, communication, and personal computer system. From the performance test of each antenna and front-end unit, it was confirmed that the system noise temperature is consistent with the value that was measured in laboratory, and that signals from 9 antennas are suitably synthesized. Using the developed observation system, the signal from Jupiter was successfully detected with the flux of 5 Jy, which is consistent with previous observations. However the effective aperture area of one antenna is smaller than the designed one. It was suggested that the roughness of alignment with 13 cm (corresponding to the phase irregularity of 50°) can be the origin of the smaller aperture area.

[1] Planetary Plasma and Atmospheric Research Center, Graduate School of Science, Tohoku University, Sendai 980-8578

[2] Solar-Terrestrial Environment Laboratory, Nagoya University, Toyokawa 442-8507

1 Introduction

1.1 The giant planet Jupiter

Jupiter is the largest planet in our solar system whose equatorial radius is about 71,492 km (defined as $1R_J$) and heavier than the total mass of the other planets in the solar system. Jupiter is mainly composed of hydrogen and helium gases, in common with Saturn, Uranus, and Neptune, which are called Jupiter-type planet.

Jupiter is also electromagneticaly the most active planet in our solar system. The magnetic moment of Jupiter is 4.2 Gauss R_J^3 with inclination of 10° against rotation axis, which is 20,000 times as large as that of the earth The rotation period of the Jovian magnetic field is $9^h55^m29.711^s$ which is defined as System III rotation period, while System I($9^h50^m30.0034^s$) and System II ($9^h55^m40.6322^s$) are defined as rotation period of atmosphere near equator and pole respectively. The strong magnetic field and rapid rotation make giant and active magnetosphere.

Moreover, Jupiter has ring and satellites near planet that interact with magnetospheric plasma. The four largest satellites, Io (at $5.9R_J$), Europa (at $9.4R_J$), Ganymede (at $15.0R_J$), and Callisto (at $26.4R_J$), called Galilean satellites, interact with magnetospheric plasma. In particular Io has a violent volcanic activity which is the origin of Io plasma torus, and this makes Io the major plasma source of magnetospheric plasma. The Amalthea (at $2.5R_J$) which is the largest among inner moons and the Jovian ring (at 1.7-$1.8R_J$) is known to interact with high energy particles in the radiation belt.

As a result of the above mentioned characteristics, Jovian magnetospheric phenomena are not only highly dynamic but quite different from the Earth's. The previous in-itu and ground-ased observations have revealed unexpected phenomena such as the violent acceleration and strong transportation of particles, powerful emission of radio waves, and dynamic variation of plasma flow.

1.2 Radio waves from Jupiter

The magnetosphere of Jupiter radiates radio waves in various frequencies. Fig. 1 shows the average Jovian radio spectrum (Kaiser, 1993). These radio waves can be classified into thermal and non-thermal radiations and the latter can be further classified into coherent and incoherent radiations.

Above 4 GHz (not shown in the figure), thermal radiation from the Jovian atmosphere is outstanding in the spectrum which follows Plank's radiation law for the atmospheric temperature of 135 K.

Below 100 MHz, non-thermal and coherent radiations from the Jovian polar region are dominant. An intense decameter wavelength emission (DAM) originates in foot print of satellite Io and Io torus, and is controlled by both central meridian longitude (CML), which is the System III longitude directing to the observer, and position of Io (Io-hase) in occurrence probability. Hectometer wavelength emission (HOM) originates in northern and southern polar regions and has correlation with the solar wind. Broad-band kilometer wavelength emission (bKOM) is thought to be radiated in polar region or

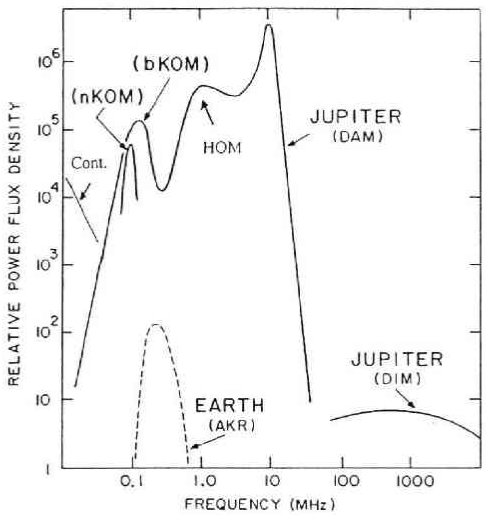

Fig. 1. Spectra of Jovian magnetospheric radiations. The power flux is normalized to constant distance. The spectrum of the Earth's is also shown as a comparison with Jupiter (Kaiser, 1993).

Io torus, but the detail characteristics has not been clarified. Narrowband kilometer wavelength emission (nKOM) is thought to have origin in the outer region of Io torus and has the System IV periodicity (3-5% slower than system III) in occurrence periodicity. Continuum emission has origin near the magnetopause and consists of a structure-less component.

In the frequency range from about 100 MHz to about 4 GHz, Jovian synchrotron radiation (hereafter referred as JSR) is emitted from the relativistic electrons, which is a non-thermal and incoherent radiation. JSR has a flat spectrum which is mainly in the decimeter (DIM) range (see JSR introduction in detail).

1.3 Observation history of the Jovian synchrotron radiation

In 1931, Karl G. Jansky discovered a radio emission from the Milky Way, which was the beginning of radio astronomy (Jansky, 1933). After an interruption by the World War II, many significant discoveries were made in 1950s and 1960s, e.g. the 21 cm line of hydrogen, the quasars, the pulsars, and the cosmic microwave background (Burke and Graham-Smith, 2002).

The Jovian non-thermal radiation was also discovered in this term by Sloanaker (1959). He used an 84-foot (about 26 m) diameter parabolic antenna at a wavelength of 10 cm, and showed that apparent blackbody temperature of Jupiter is 640 K$\pm$85 K which was unexpectedly high value comparing with infrared measurements.

As properties of the radiation (spectrum, polarization) became clear, it was thought that the radiation is caused by synchrotron radiation originating from trapped energetic particles in the Jovian radiation belt (e.g. Field, 1959). The identification of the Jovian

synchrotron radiation means the discovery of extraterrestrial radiation belt by means of the remote sensing, while the Earth's radiation belt was discovered in 1958 by Van Allen with in-situ observation using Explorer 1.

By 1970s, static properties of JSR using single dish antenna were almost confirmed, and from which the basic properties of the Jovian magnetic field were derived such as the magnetic field strength, polarity, tilt angle, and planetary spin period. These are confirmed afterward by the in-situ observations by Pioneer 10, 11.

After 1970s, objects of JSR observation focused on spatial distribution and time variation to study structure and dynamics of the radiation belt. Characteristics of the spatial distribution is described in section 2.4 in detail, while Characteristics of time variation is described in section 2.5 in detail.

1.4 The purpose of this thesis

The Jovian synchrotron radiation reflects information on the radiation belt, in particular its time variation has an important clue to clarify acceleration and transport processes. So far remote sensing using synchrotron radiation is the only method to investigate the Jovian radiation belt precisely because in-situ observation is almost impossible due to the heavy radiation damage to instruments of spacecraft. A few in-situ observation have been performed for the radiation belt, however, the observation gave only temporal static features. We consider that it is essential to develop exclusive observation system which enable us to make continuous observation.

In this thesis, general introduction of Jupiter is described and an introduction for JSR is described. After summarizing of in-situ observation of the Jovian radiation belt, the basic design of the observation is described and the developed system is described precisely. The measurements of parameters to synthesizing of signals is described, the result of test observation is described, discussed, and concluded.

2 Characteristics of the Jovian synchrotron radiation

2.1 Mechanism of synchrotron radiation

Synchrotron radiation is the relativistic counter part to cyclotron radiation. Simple diagram of synchrotron radiation is shown in Fig. 2 (Feynman *et al.*, 1965). For the rotating particle with low speed, an observer looks the position of particle as sinusoidal curve (dashed line of Fig. 2), which produces a sinusoidal electric field whose twice derivation shows the power of electromagnetic wave. However for the rotating particle with nearly light speed, an observer looks the position of the particle as a pulse at the moment when the particle directs toward the observer (solid line of Fig. 2), which produces broadband electromagnetic wave derived by the Fourier transform of the pulse.

The period of the pulse (T) is

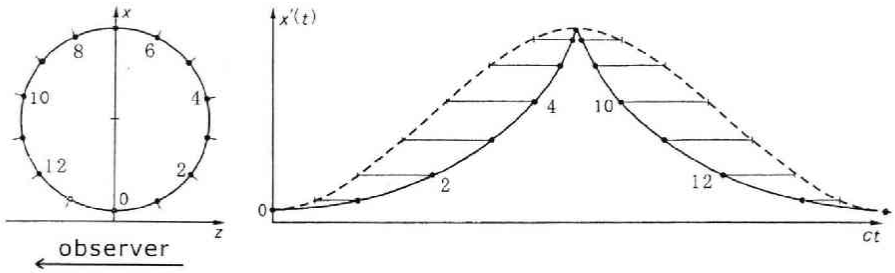

Fig. 2. Schematic diagram of synchrotron radiation. The observed position of a rotating particle becomes sharp at the point toward observer as speed of particle comes to close to speed of light (Feynman, 1965).

$$T=\frac{\gamma}{f_e} \tag{1}$$

and the solid angle (ξ) of the radiation concerning width of the pulse is

$$\xi=\frac{1}{\gamma} \tag{2}$$

where f_e is the cyclotron frequency and γ is the relativistic factor, i. e.,

$$f_e=\frac{eB}{2\pi m_e} \tag{3}$$

$$\gamma=\frac{E}{mc^2} \tag{4}$$

$$=\frac{1}{\sqrt{1-\left(\frac{v}{c}\right)^2}} \tag{5}$$

The transition from cyclotron radiation to synchrotron radiation is shown in Fig. 3 (reproduced from Akabane *et al.*, 1988).

From the analytical calculation the power specta for orthogonal polarizations, which are perpendicular and parallel to magnetic field, are shown as

$$P_{\perp}(f)=\frac{\sqrt{3}e^3B\sin\alpha}{2mc^2}[F(x)+G(x)] \tag{6}$$

$$P_{\parallel}(f)=\frac{\sqrt{3}e^3B\sin\alpha}{2mc^2}[F(x)-G(x)] \tag{7}$$

respectively, where

$$x=f/f_c \tag{8}$$

$$f_c=\frac{3}{2}\gamma^2 f_e \tag{9}$$

$$=\frac{3e}{4\pi m^3c^5}E^2B\sin\alpha \tag{10}$$

$$F(x)=\int_x^{\infty}K_{5/3}(\xi)\,d\xi \tag{11}$$

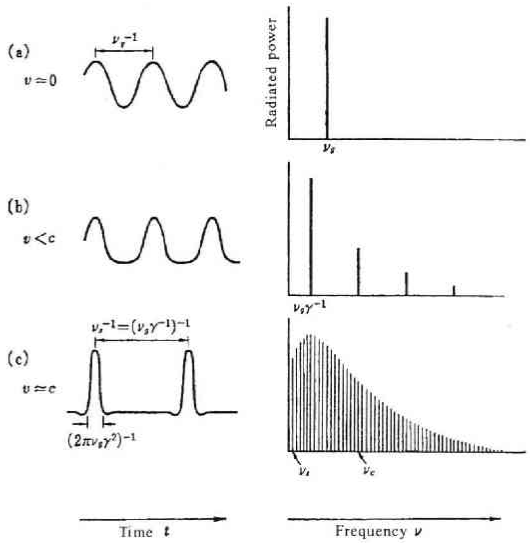

Fig. 3. Transition from cyclotron radiation to synchrotron radiation (from (a) to (c)) in the time domain (left side) and frequency domain(right side). (Adapted from Akabane et al., 1988)

$$G(x)=\int_x^\infty K_{2/3}(\xi)d\xi \tag{12}$$

$K_{5/3}$: modified Bessel function of order 5/3 (13)

$K_{2/3}$: modified Bessel function of order 2/3 (14)

From the differences between Equation (6) and (7), it is clear that the synchrotron radiation is polarized. Polarization is a relationship between rectangular two components of electric field. The Stokes parameters are convenient to display polarization of an electro magnetic wave. The Stokes parameters are set of 4 terms defined as

$$I=E_0^2 \tag{15}$$

$$Q=E_0^2\cos 2\varepsilon\cos 2\tau \tag{16}$$

$$U=E_0^2\cos 2\varepsilon\cos 2\tau \tag{17}$$

$$V=E_0^2\sin 2\tau, \tag{18}$$

where E_0, ε, and τ are total power, axial ratio of polarization ecllipse, and orientation of polarization ecllipse, respectively. The relation of these parameters are shown in Fig. 4.

Using the Stokes parameters, degree of linear polarization (P_L) and degree of circular polarization (P_C) are displayed as

$$P_L=\frac{\sqrt{Q^2+U^2}}{I} \tag{19}$$

$$P_C=\frac{V}{I} \tag{20}$$

and degree of polarization (d) is displayed as

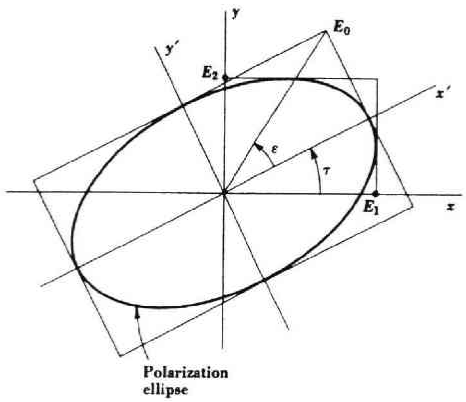

Fig. 4. Relation of polarization ellipse, and definition of ε and τ (Kraus, 1986).

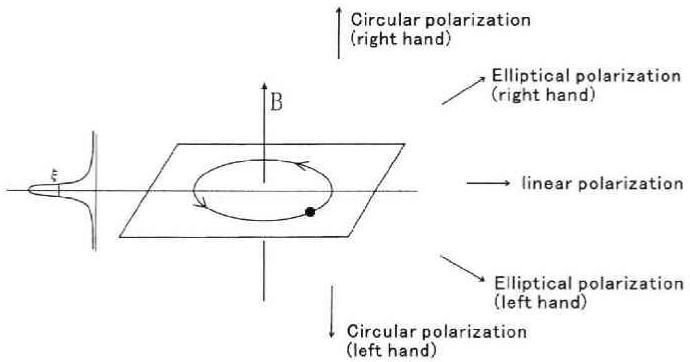

Fig. 5. Directivity of radiated power (left) and polarization (right) of synchrotron radiation from a single electron gyrating perpendicular to the magnetic field.

$$d=\frac{\sqrt{Q^2+U^2+V^2}}{I} \tag{21}$$

$$=\sqrt{P_L^2+P_C^2} \tag{22}$$

Using Equation (6) and (7), the degree of linear polarization (P_L) is derived as

$$P_L=\frac{P_\perp(f)-P_\parallel(f)}{P_\perp(f)+P_\parallel(f)}=\frac{G(x)}{Fx)} \tag{23}$$

which becomes about 0.75 by integrating over all frequencies. The directivity of radiated power and polarization are shown in Fig. 5.

From Equation (6) and (7), the composed power spectrum is obtained as

$$P(f)=P_\perp(f)+P_\parallel(f) \tag{24}$$

$$=\frac{\sqrt{3}e^3B\sin\alpha}{mc^2}F(x) \tag{25}$$

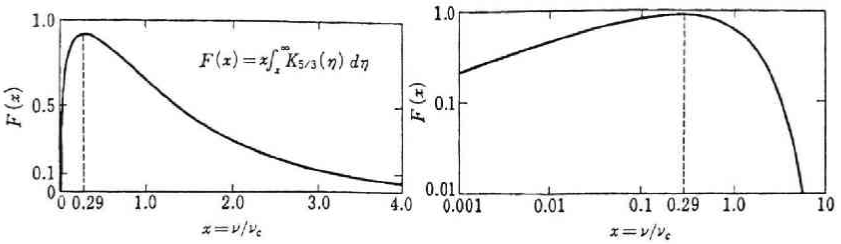

Fig. 6. Theoretical spectrum of synchrotron radiation from a single particle, which is displayed as Equation (11), in linear scale (left) and log scale (right) (Akabane *et al.*, 1988).

The shape of the spectrum, which is the envelope of Fig. 3(c), is defined by function $F(x)$ as shown in Fig. 6 (Akabane *et al.*, 1988). Because function $F(x)$ has a single peak at $x=0.29$, the spectrum of synchrotron radiation also has a peak at $x=0.29$. Thus, from Equation (8) and (9) we obtain a peak frequency as

$$f_{\max}=0.29f_c \tag{26}$$

$$=0.29\frac{3e}{4\pi m^3c^5}E^2B\sin\alpha \tag{27}$$

$$\simeq 4.8E^2B\sin\alpha, \tag{28}$$

where $f_{\max}$ is in [MHz], E is in [MeV], B is in [Gauss] for Equation (28).

The total power emitted by single electron, which is equivalent to energy loss rate, is calculated by integrating $P(f)$ over all frequencies, i.e.

$$P=\int_0^\infty P(f)df \tag{29}$$

$$=\frac{2e^4}{3m^4c^7}E^2B^2\sin^2\alpha \tag{30}$$

$$\simeq 6\times10^{-22}E^2B^2\sin^2\alpha. \tag{31}$$

where P is in [Watt], E is in [MeV], and B is in [Gauss] for Equation (31).

For the case of assembly of electrons, the volume emisivity $\varepsilon(f)$ can be derived by multiplying $P(f)$ and energy spectrum $N(E)$, and integrating it over the energies, i.e.

$$\varepsilon(f)=\frac{1}{4\pi}\int P(f)N(E)dE. \tag{32}$$

The observed flux is the integrated volume emisivity along the line of sight, i.e.,

$$S(f)=\Omega_B\int\varepsilon(f)ds. \tag{33}$$

where Ω_B is the solid angle of antenna beam. The flux $S(f)$ is expressed in Janskey unit ($\mathrm{Jy}=10^{-26}\mathrm{Wm^{-2}Hz^{-1}}$).

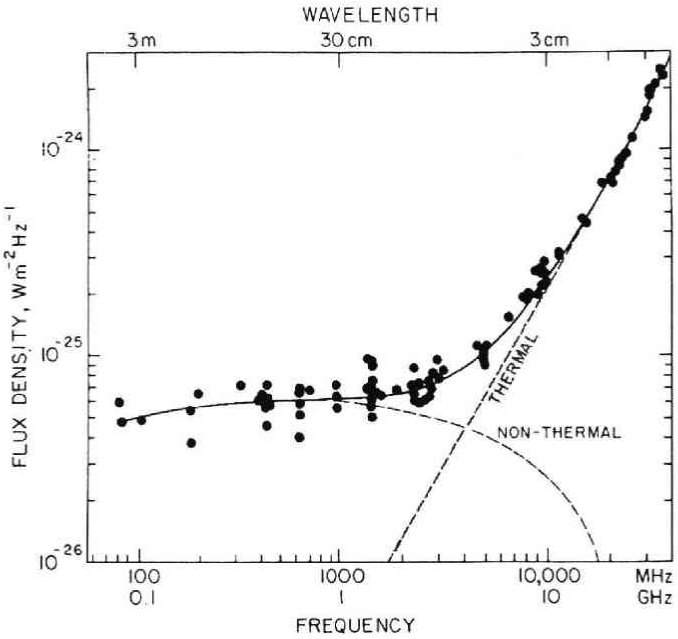

Fig. 7. Typical radio spectrum of Jupiter from 70 MHz to 30 GHz (black points and solid line). The spectrum in this frequency range consists of non-thermal (synchrotron) component, which is shown by dashed line and thermal component, which is shown by dashed line (Carr *et al.*, 1983).

2.2 Spectrum

The observed average spectrum of JSR is shown in Fig. 7 (the dashed line). The dashed red line in the Fig. is the thermal emission from Jovian disk, which is described by Planck's radiation law with temperature of 135 K.

According to Equation (32), it is clear that the spectrum of JSR strongly reflects the electron energy spectrum of the Jovian radiation belt. de Pater and Goertz (1990) calculated JSR spectrum as a function of L-value assuming the energy spectrum of relativistic electrons, and compared it to the Pioneer in-situ data at $L=6$. They found that the energy spectrum of relativistic electrons is hardened between $L=3$ and 1.5, which may be caused by physical process like a degradation of energy by ring particles around Jupiter.

de Pater *et al.* (2003) carried out a brief campaign in September 1998 using 11 antennas in order to determine the spectra of JSR from 74 MHz up to 8 GHz. Comparing the spectra with that of July 1994 (just before the impacts of Comet Shoemaker-Levy 9), a significant difference was found (Fig. 8, see page 78). They pointed out as a cause of the difference that pitch angle scattering, coulomb scattering and/or energy degradation by the dust occurred in the Jovian inner radiation belt.

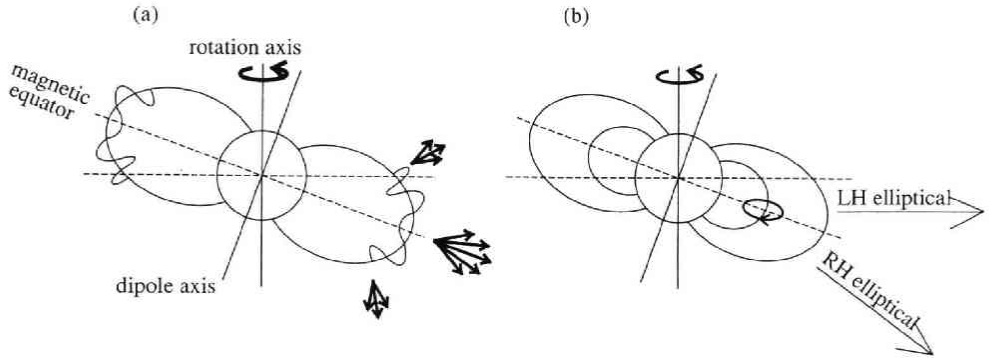

Fig. 9. Directivity of radiated power (a) and polarization (b) of JSR. Those parameters vary with the Jovian rotation, which is called beaming effect (adapted from Carr *et al.*, 1983).

2.3 Beaming curve

Because the synchrotron radiation has a strong directivity with respect to power and polarization, an observed JSR shows dependence on the Jovian rotation, which is called 'Beaming curve' (Fig. 9). Fig. 10 shows variations of total power, position angle (angle of polarization plain against rotation axis), degree of linear polarization, degree of circular polarization, and magnetic latitude as a function of System III longitude (de Pater, 1980).

As the beaming curve has a periodicity as a function of CML, it is possible to expand to Fourier series, i.e.,

$$\sum_{i=0,1,2,\cdots} A_i \cos[i(\lambda_{CML}+\lambda_i)] \tag{34}$$

where A_i and λ_i are the amplitude and phase concerning to period of i times, i.e., A_0 means average intensity over the Jovian rotation. For example in the case of the total power S, the component of A_2 is superior, because it has two peaks at the Jovian equator aligned to an observer.

Because synchrotron radiation has a directivity perpendicular to the magnetic field, beaming curve is very sensitive to the direction of the Jovian magnetic field and declination of the Earth (D_E). Dulk *et al.* (1999a, b) evaluated the Jovian magnetic field model using beaming curve, in which they used the 3D imaging data of JSR to exclude the effect of line of sight.

2.4 Spatial distribution

The apparent radius of Jupiter is about 25 arc second at opposition. Then, an antenna with diameter of nearly 80 km is required to resolve the spatial distribution of 0.1 R_J at 327 MHz due to the diffraction limit, which is calculated from λ/D, where D is a diameter of antenna and λ is wavelength. An interferometer whose diffraction limit is calculated from λ/Ds, where Ds is the separation of antennas, can achieve the spatial resolution to resolve the distribution of JSR. Calculated diffraction limits of the inter-

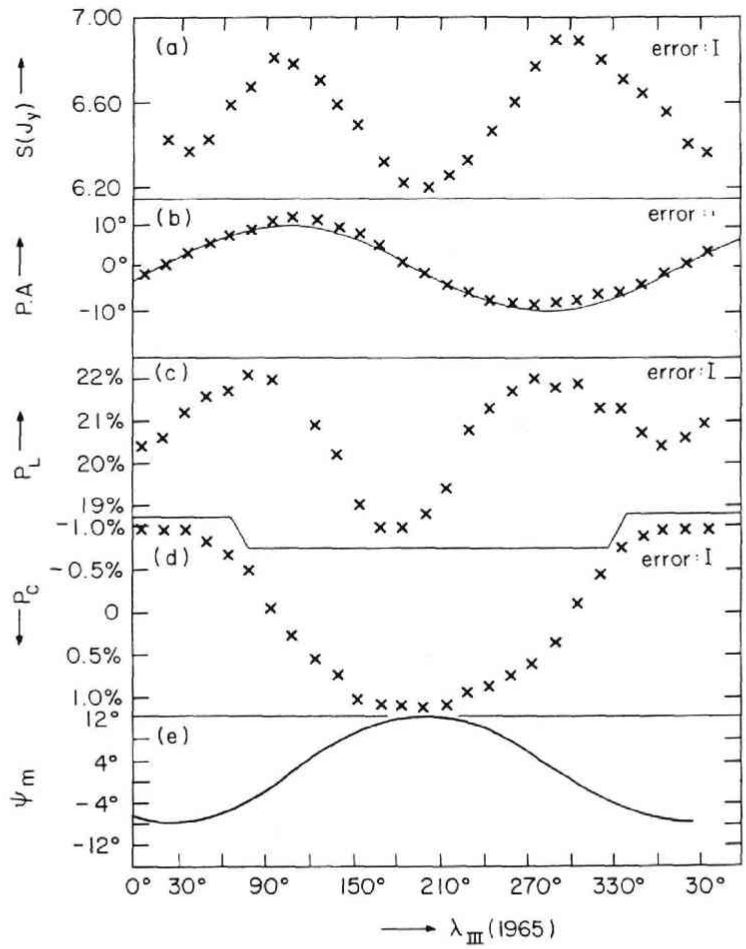

Fig. 10. Beaming curve (geometrical variations of parameters) of JSR as a function of central meridian longitude (λ_{III}) for total flux (S), angle of polarization plain against rotation axis ($P.A.$), degree of linear polarization (P_L), degree of circular polarization (P_C), and magnetic latitude (ψ_m) (de Pater, 1980).

ferometer system for various frequency and Ds are shown in Fig. 11.

Radhakrishnan and Roberts (1960) and Morris and Berge (1962) resolved JSR source for the first time using an interferometer. They used two 90 feet (27 m) antennas at 960 MHz and 1.4 GHz and reported that the source region of JSR extended within 1 (polar direction) and 3 (equatorial direction) planetary diameters by using the Gaussian fitting for the observed data.

Berge (1966) first produced a source map (two-dimensional brightness distribution) by combining the data observed at Owens Valley Radio Observatory (Fig. 12). The result was almost consistent with the recent observation. He assumed that the brightness distribution was azimuthally symmetric with respect to the dipole magnetic axis which tilted about 10° against the spin axis, and fitted Gaussian functions to the observed

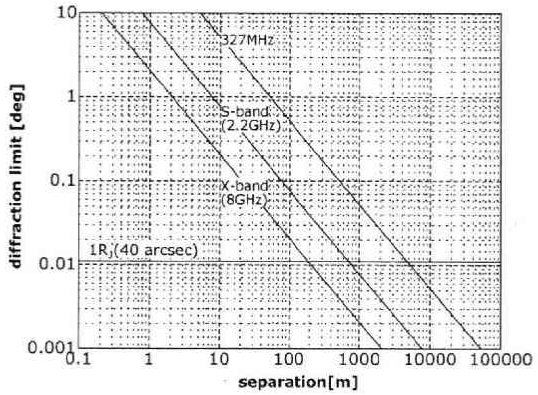

Fig. 11. Diffraction limits (λ/D) for various frequencies, where D is a diameter of antenna for a single antenna or separation of antennas for an interferometer.

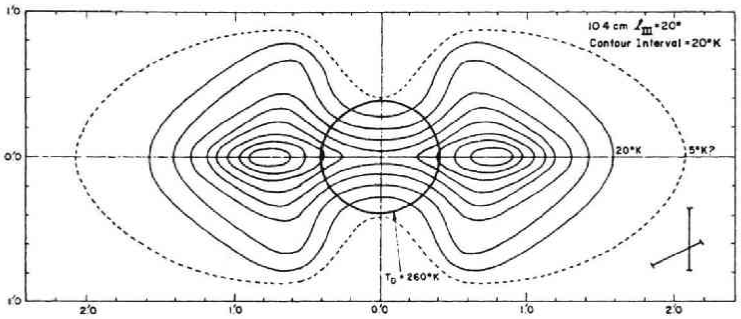

Fig. 12. Two-dimensional brightness distribution of JSR at CML=20° at a wave length of 10.4 cm. The spatial scales are in minutes of arc (Berge, 1966).

visibility functions.

Gulkis (1970) obtained one-dimensional equatorial brightness distribution using lunar occultation on October 19, 1968. The acquired distributions along the equator showed a clear double-peaked structure with a slight asymmetry and rather extended to far from Jupiter in lower frequency.

The Very Large Array (VLA) built in 1981 at New Mexico, USA has made a great improvement on imaging observation of JSR compared with observations in 1970s (e.g. de Pater, 1980 ; de Pater, 1981). VLA consists of 27 antennas with each diameter of 25 m, which are mounted on the "Y" formed rail with the farthest distance of 21 km long. Fig. 13 shows a two-dimensional brightness distribution obtained by VLA (de Pater, 1991).

The Australia Telescope Compact Array (ATCA) is another facility that can obtain two-dimensional brightness distribution of JSR, which consists of 6 antennas with 22 m diameter each, located along east-west baseline whose span range from 153 m to 6 km. Leblanc *et al.* (1997) and Dulk *et al.* (1997) produced the first three-dimensional brightness distribution of JSR from two-dimensional brightness distributions observed with ATCA using the tomographic technique. Three-dimensional brightness distribution can

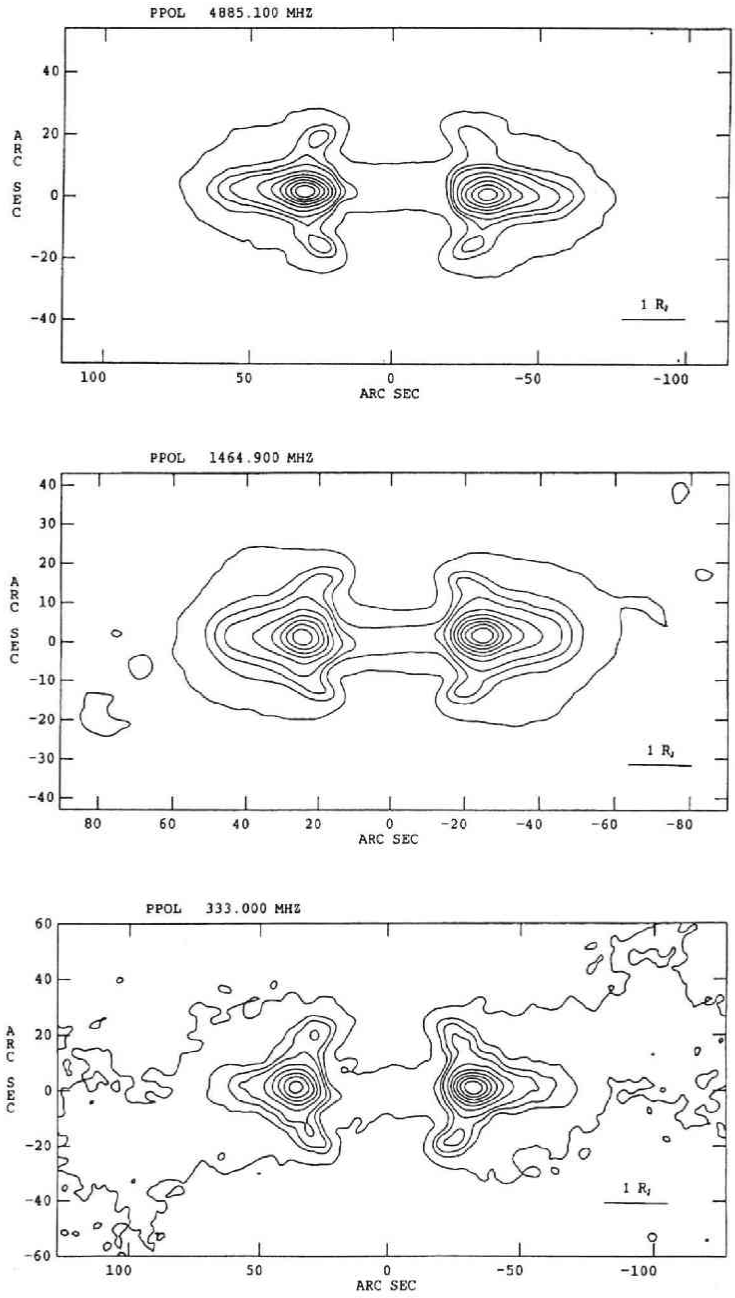

Fig. 13. Two-dimensional brightness distributions obtained by VLA at 6 cm (top), 21 cm (middle), 90 cm (bottom). The maps show only a linealy polarized flux density (de Pater, 1991).

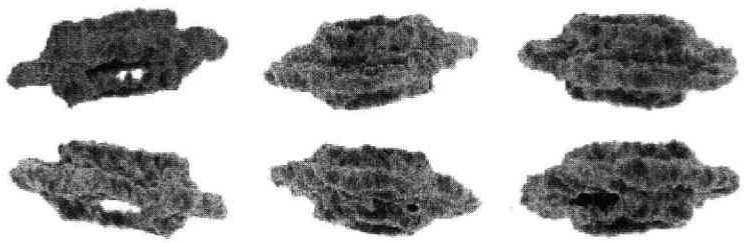

Fig. 14. Three-dimensional brightness distributions of JSR at 13 cm obtained by ATCA using the tomographic technique. The viewing CML values are is 90°, 150°, 210°, 270°, 330° from left to right, top to bottom (Sault *et al.*, 1997).

be obtained when adequate views from the different rotational aspects are taken and the optical thickness of the emission is assumed to be thin. Sault *et al.* (1997) showed that a visibility, which is a function of projected baseline vector ($V(u, v, w)$) and a three-dimensional brightness distribution ($I_0(x, y, z)$) at normalized distance (R_0), form a Fourier pair ; i.e.,

$$V(u, v, w)=\left(\frac{R_0}{R}\right)^3\int I_0(x, y, z)\exp\left(\frac{-2i\pi(xu+yv+zw)}{\lambda R}\right)dxdydz, \tag{35}$$

where R is distance to source, and λ is wavelength. Fig. 14 shows examples of three-dimensional brightness distribution of JSR observed with ATCA (Sault *et al.*, 1997).

In a three-dimensional brightness distribution of JSR, it is considered that the flux peak is in the magnetic equator, because under the following reasons ; (1) most electrons have pitch angle near 90° (2) most intense radiation is almost perpendicular to the magnetic equator. Using this relation, Dulk *et al.* (1999a) evaluated the H4 and VIP 4 magnetic field models (Connerney *et al.*, 1998), and Dulk *et al.* (1999b) showed that changes of two-dimensional brightness distribution between different declination angles of the Earth (D_E) can be explained by warping of the magnetic equator originating from higher order terms of the intrinsic magnetic field.

de Pater *et al.* (1997) showed influences of the Jovian ring and inner moon on particle distribution by comparing models with high-resolution radio images obtained by VLA (Fig. 15, see page 78). The best-fit model among 16 models is shown in Fig. 16. From the model, it is confirmed that electron pitch angle distribution becomes isotropic at Amalthea's orbit around 2.5R_J (Fig. 16(b)), which makes 'shoulder' structure (flattening in intensity curve) in East-West cross section (Fig. 16(d)), and that 80%-100% of electrons are absorbed by the ring around 1.7R_J (Fig. 16(a)), which makes discrete peaks at high latitude in the radio map (Fig. 16(c)).

Bolton *et al.* (2001) produced a radio map of JSR based on the Divine Garret model (Divine and Garret, 1983) of the electron distribution, and compared with observed radio maps made with the VLA data. They suggested that the Divine-Garret model significantly underestimates the number of relativistic electrons(>1 Mev) as a factor of 6 in the Jovian radiation belt, and that pitch angle distribution is more anisotropic

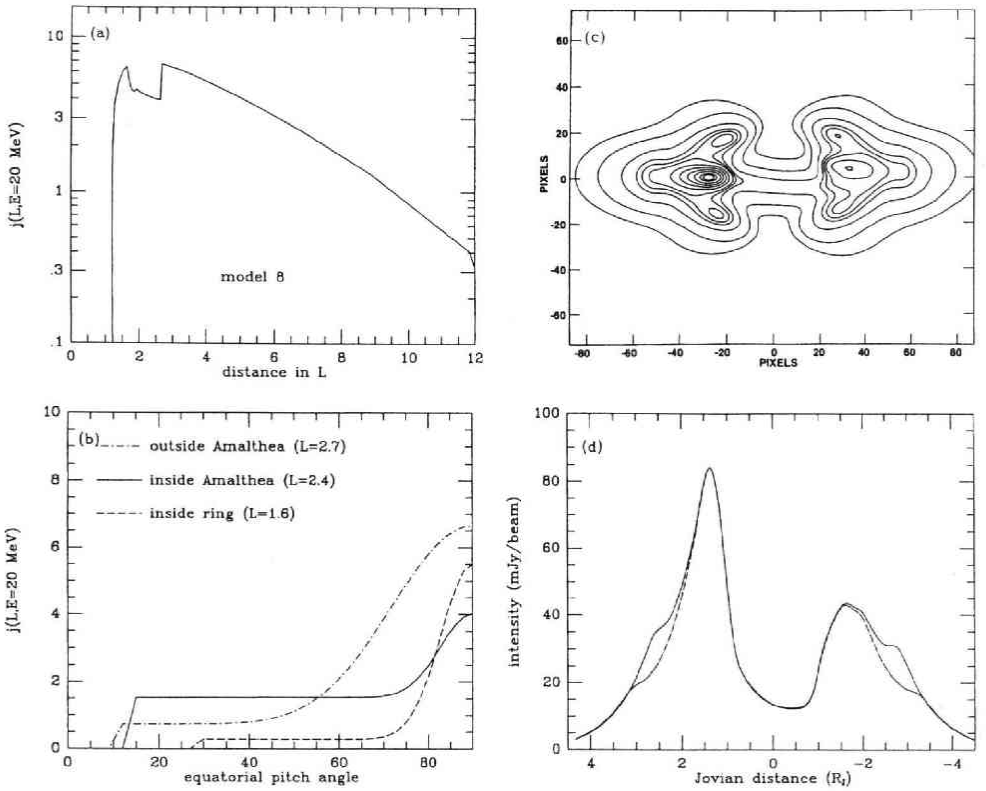

Fig. 16. Best fit model to the VLA observation. (a) Electron flux at the magnetic equator (E=20 MeV), (b) pitch angle distribution, (c) modeled intensity distribution, and (d) cross section of modeled intensity distribution along the magnetic equator (de Pater *et al.*, 1997).

(concentrating to the magnetic equator) than the Divine-Garret model to account for the observed radio maps. Furthermore, Levin *et al.* (2001) constructed a model of the electron distribution to account for the observed radio maps, in which the electron density was assumed to have a following form

$$n_e(a, L, B)=A_L\sin^{n1}(\alpha_{eq})+B_L\sin^{n2}(\alpha_{eq}), \tag{36}$$

where α_{eq} is equatorial pitch angle, parameters of A_L, B_L, $n1$, $n2$ are functions of L, which are determined from the observed radio maps. Produced JSR maps using the model showed a good agreement with the observed radio maps and beaming curve.

Recently an attempt to search the fine structure in JSR was performed using Very Long Baseline Interferometer (VLBI) in 2001 (Kondo, private communication).

2.5 Time variation

While the 'Beaming curve' originates from the viewing geometry between Jupiter and the Earth as described in Section 2.3, variations which are thought to be originated

from time variations of the Jovian radiation belt itself have been disclosed in recent years. The time variation can be roughly classified into three categories ; (1) long term variation having time scale of decade (top panel in Fig. 17, see page 79), (2) short term variation having time scale of days or weeks (bottom panel in Fig. 17), and, while peculiar case, (3) time variation at the time of the impacts of comet Shoemaker-Levy 9 (on July, 1994 in Fig. 17).

2.5.1 Long term variation

Since 1971, the antennas of the NASA Deep Space Network (DSN) have been used to measure JSR flux density several times in a month, which is known as 'Jupiter patrol'. Bolton *et al.* (1989) analyzed time serial data from 1963 to 1985 (for about two solar cycles), which include both the 'Jupiter patrol' data and before 'Jupiter patrol' data, and showed that JSR flux density had a correlation with solar wind parameters (the data prior to 1974 had been already reported by Klein (1976)). Fig. 18 shows a time variation of JSR flux density and solar wind ram pressure shifted forward 2.0 years, which has the highest correlation coefficient of 0.87 with 2.0 years lag. From the figure, it has been believed that solar wind controls the flux density of JSR.

de Pater and Goertz (1994) explained the correlation by means of a simulation. They assumed that the primary mode of the electron transport is the radial diffusion driven by the neutral winds in Jupiter's upper atmosphere/ionosphere, and that the diffusion coefficient is proportion to L^3 based on the discussion by Brice and McDonough (1973). In these assumptions, the phase space density $f(\mu, L, t)$ is written by the Fokker-Planck type diffusion equation, i.e.

$$\frac{\partial f(\mu, L, t)}{\partial t} = L^2 \frac{\partial}{\partial L}\left(\frac{D_{LL}}{L^2}\frac{\partial f(\mu, L, t)}{\partial L}\right) + Source - Loss \tag{37}$$

$$D_{LL} = D_n L^n, \tag{38}$$

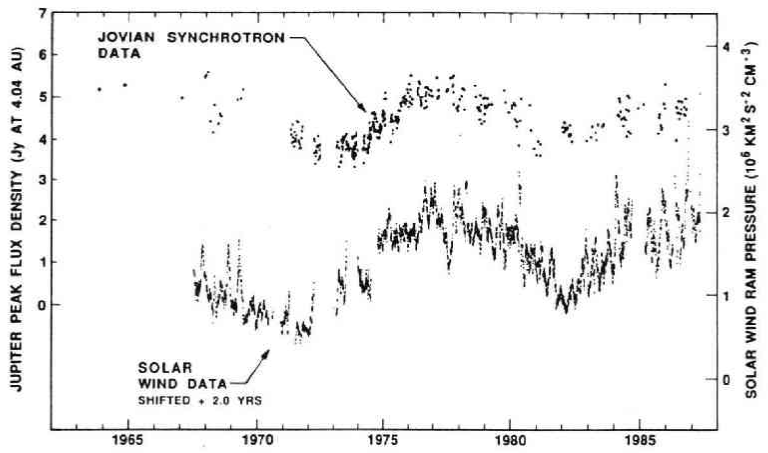

Fig. 18. Time variation of JSR (top and left axis) and solar wind ram pressure shifted 2.0 years (bottom and right axis). Clear correlation was shown (Bolton, 1989).

where D_{LL} and D_n are diffusion coefficient and diffusion constant concerning L^n ($n=3$ is adopted after Brice and McDonough, 1973). *Source* indicates an injection of particles at the outer boundary, and *Loss* includes synchrotron loss formed by Birmingham *et al.* (1974), and loss by dust, coulomb scattering, and pitch angle scattering as a function of L-value.

They assumed that the time variation is not caused by the change of D_{LL} but by the change of outer boundary condition, because the change of D_{LL} will cause the change of radiation peak position, which had not been observed (de Pater and Goertz, 1990). In this calculation, the outer boundary was set to be $L_1=50$, which did not make significant differences in the case of $L_1=20$–50, and the time-dependent phase space density at the boundary was given in proportion to square root of the solar wind ram pressure,

$$f|_{L=L_1} \propto \sqrt{N_{sw} \cdot v_{sw}^2}, \tag{39}$$

where N_{sw} and v_{sw} are the number density and velocity of solar wind, respectively. They, then, searched the best-fit D_3 which reproduce observed time variations of JSR. The assumption of Equation (39) was empirical, but it might be explained if the electron energy spectrum is power law with-1 because the ratio of energy to magnetic field strength (first invariant) is constant and the magnetic field strength at plasma pause is proportional to square root of solar wind ram pressure.

The result is shown in Fig. 19, in which the calculated time variation of JSR agrees with the observation very well. From the χ^2 test, D_3 was obtained to be $1.3\pm0.2\times 10^{-9}\ s^{-1}$ which was consistent with the observed lag time of 2 year. They also pointed

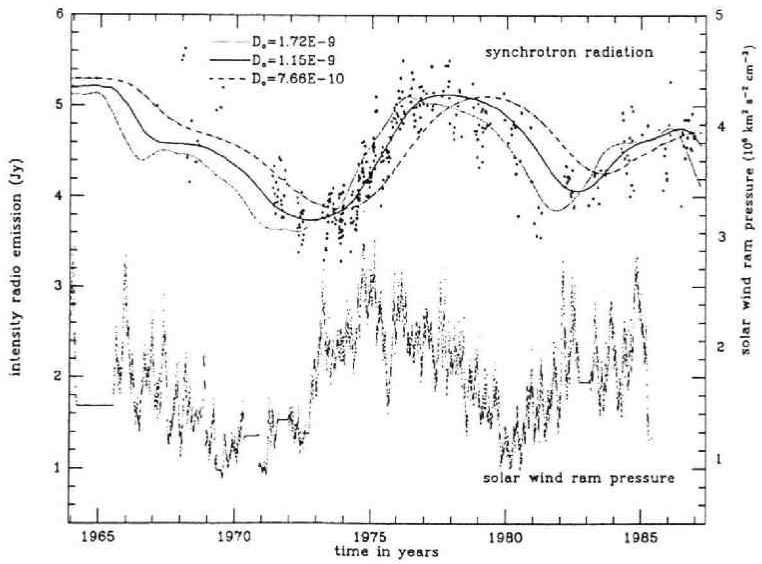

Fig. 19. Calculated time variation of JSR (solid, dot, and dashed lines). The others are the same as Fig. 18 but solar wind ram pressure is not shifted (de Pater and Goertz, 1994).

out that the short term (days-weeks) time variation in JSR could not be explained by the radial diffusion.

2.5.2 Events on the impacts of comet Shoemaker-Levy 9

Shoemaker-Levy 9 (hereafter referred as SL9) was a comet consisting of over 20 nuclei aligned as string, which impacted into Jupiter during the period from July 17, 1994 to July 22, 1994. Because SL9 was crushed into nuclei by the Jovian tidal force at previous closest approach in 1992, SL9 had dust clouds and larger materials, which were thought to be injected into the Jovian magnetosphere having influence on not only the Jovian atmosphere but also environment of the inner magnetosphere.

Prior to the impacts, de Pater (1994) estimated influence of dust on JSR using numerical simulation, which accounted for the increasing of dust by the same way as de Pater and Goertz (1990). It was predicted by the simulation that the total power of JSR would be reduced more than 10% by means of the absorption of relativistic electron by the dust, and that the spectra of JSR would become hard, and the influence of SL9 would continue for many months.

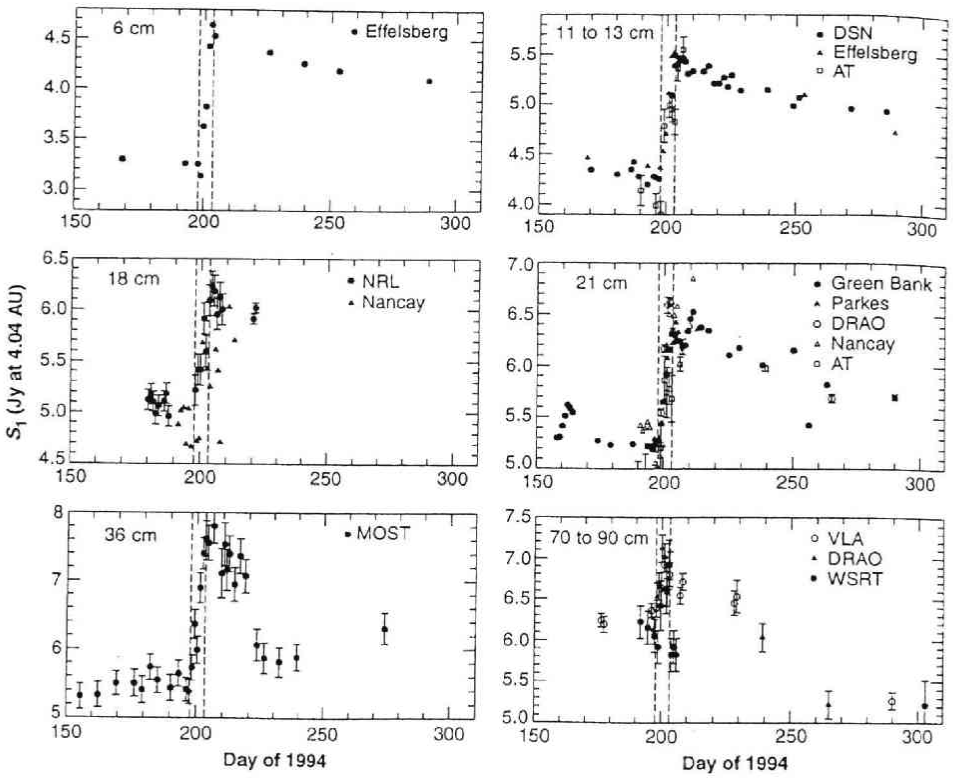

Fig. 20. JSR flux variation during the SL9 impacts (between dashed line) for various frequencies. Flux intensifications are found for all frequencies, but time scale of flux decay is longer in the higher frequency (de Pater *et al.*, 1995).

The period before, during, and after the collision, intensive observation was carried out using 11 antennas in the world. The assemble of observations of total flux in various frequencies is shown in Fig. 20 (de Pater *et al.*, 1995). The total flux increased in all frequencies against the prediction, but the time constant of dumping of flux was comparable to the prediction. The hardening of the spectrum (de Pater *et al.*, 1995), change of beaming curve (Bolton *et al.*, 1995), and the brightening of certain location corresponding to the impacts of large cores (Sault *et al.*, 1997) were also observed. Moreover from the high-resolution image by VLA, inward shift (toward the planet) of the peak and, the decrease of the brightness at the instant of the first impact, delay of brightening between equational peak and high latitude peak, the shift of high latitude peak toward the equator were observed (de Pater and Brecht, 2001a).

As mentioned above, the drastic change was occurred during the SL9 impacts. However explanations for all observation results, even increasing of flux density, are not agreed at all. The complex of following three mechanisms is thought to be possible (Brecht *et al.*, 2001b); sudden increase of the radial diffusion by the electromagnetic turbulence (de Pater and Brecht, 2001b), acceleration by the collisionless shock in the same manner as in the interplanetary shock (Brechet *et al.*, 1995), and pitch angle scattering due to the wave-particle interaction with whistler mode waves (Bolton and Thorne, 1995).

2.5.3 Short-term variation

The short-term variations having time-scale of few days or weeks had been reported in early 1960's. However those most reports were not confirmed because of background confusion effects and/or instrumental instabilities (Carr *et al.*, 1983). The former originates from structure of radio galaxy behind Jupiter, the later is due, for example, to the variation of the power supply and to ambient temperature fluctuations. In particular, gain fluctuations can not be distinguished from signal power variations of a radio star (Kraus, 1986).

Gerard (1970a, b) reported the time variation of JSR quantitatively for the first time, and suggested the correlation with solar F10.7 variation using the Nançay radio telescope at 2695 MHz during the period from December 1967 to August 1968. Gerard (1976) also reported two bursts (probably four), especially the greatest one was enhancement of flux density of 9% (9 times of rms error), and continued for about a week. Klein, however, reported that there was no short-term time variation using NASA Deep Space Instrumentation Facility at Goldstone at 2388 MHz (12.6 cm) between May and October, 1971 (Klein *et al.*, 1972).

Recent observations have been revealing the feature of short-term time variations of JSR. The observations based on precise calibrations enable to detect the natural variation of JSR.

Miyoshi *et al.* (1999) reported the short-term variation of JSR using the 34 m radio telescope of Kashima Space Research Center at 2.2 GHz between November 12 to 24, 1996. The reported increase of JSR was 14% during 4 days (Fig. 21). The absolute flux

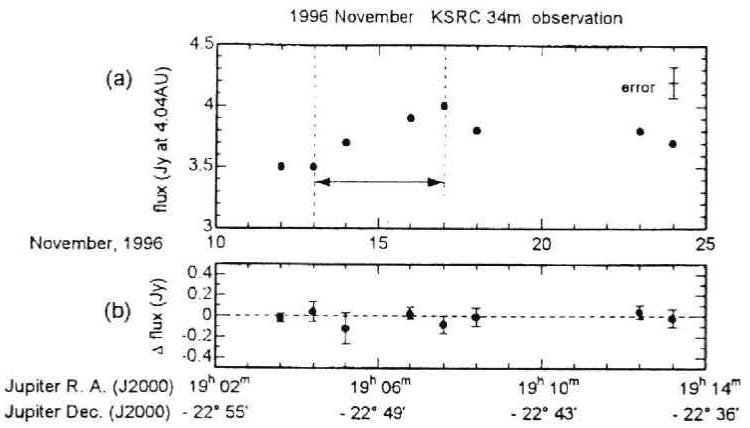

Fig. 21. (a) Daily variation of JSR at 2.2 GHz observed at Kashima Space Research Center. Increase of about 14% is clearly shown, which is significantly larger than error bar ($\pm\sigma$). (b) Background confusion level for the sky behind Jupiter measured 11 month later (Miyoshi *et al.*, 1999).

density was measured using calibration sources of 3C286, 3C295, 3C48, and 3C309.1, and evaluating the pointing error, extinction by terrestrial atmosphere, gain fluctuation, distance between Jupiter and Earth, thermal radiation, beaming curve, and background structure behind Jupiter (shown in Fig. 21(b)).

Because the detected variation had a correlation with solar F10.7 with a 9 day shift, which corresponds to azimuthal difference between Jupiter and Earth with respect to the solar rotation, they assumed the variation originated from activation of radial diffusion induced by UV/EUV heating of Jupiter's upper atmosphere. This idea was originally predicted by Brice and McDonough (1973). They also performed the numerical simulation which reproduced the observed flux enhancement by increasing 2.5 times of radial diffusion coefficient (D_{LL}) during 5 days (Fig. 22).

During the encounter of the Cassini spacecraft with Jupiter, the 'Jupiter patrol' was intensified and JSR observation was made. Then, the existence of short-term variation was confirmed (Fig. 17(b)).

Gelopeau and Gerard (2001) monitored JSR at 21.3, 18.0, and 9.1 cm from April 1994 to June 1999 using the Nançay Radio telescope. The data clearly revealed the presence of time variation with the time scale of months and year (Fig. 23), and they call these 'medium-term' variation. Moreover, they reported that spectral index of JSR was strongly correlated with the 9.1 cm flux density, and time variation was correlated with almost all solar wind parameters with a lag time of 245 days but dynamic and ion thermal pressure showed a correlation with a lag time of 615 day.

The existence of short-term variation has been revealed, while the mechanism of short-term variation is not clarified yet. This is because there are few continuous data having time resolution of few days because of lack of machine time to observe JSR. So, it is necessary to develop an antenna exclusively adopted for JSR observation to clear

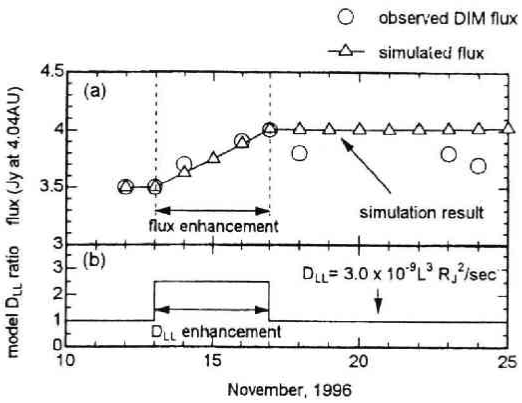

Fig. 22. (a) Comparison of model simulation (line with triangle) with observation (open circle). (b) Time variation of radial diffusion coefficient (D_{LL}) used in the simulation (Miyoshi *et al.*, 1999).

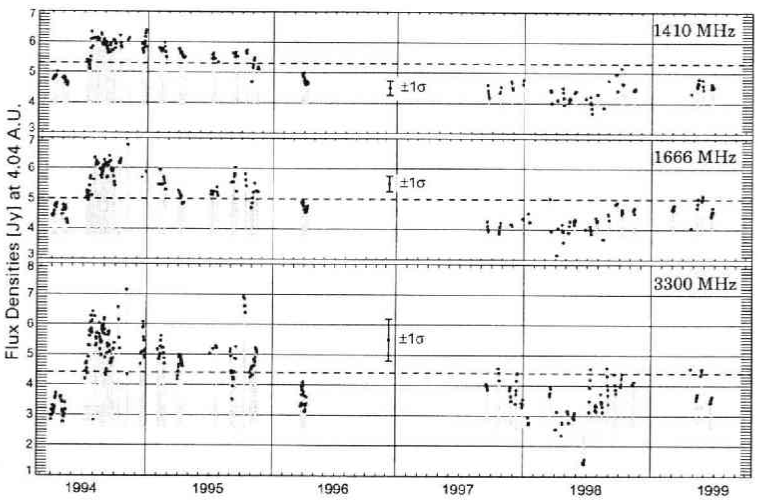

Fig. 23. Flux densities of JSR at 1410 MHz (top), 1666 MHz (middle), and 13300 MHz (bottom), and typical error bar. Dashed line is a references level before the SL9 impacts and start point of gray-shaded line represents the minimum value of flux defined as 3% of histogram of flux (Gelopeau and Gerard, 2001).

characteristics of the short-term variation and the physical processes.

3 Remote sensing of the Jovian magnetosphere

3.1 Summary of in-situ observation of the Jovian radiation belt

Until now, 7 spacecrafts visited Jupiter as listed in Table 1.

The orbits of the spacecrafts projected onto the magnetic meridian plain are shown in Fig. 24 (see page 79). The spacecrafts which passed the inner radiation belt were

Table 1. The spacecraft visited Jupiter.

	Closest approach	type
Pioneer 10	Dec., 1973	fly by
Pioneer 11	Dec., 1974	fly-by
Voyager 1	Mar.,1979	fly-by
Voyager 2	Jul., 1979	fly by
Ulysses	Feb., 1992	fly-by
Galileo	Dec., 1995-Sep.,2003	satellite
Cassini	Dec., 2000	fly by

Pioneer 10, 11, and Galileo probe. The orbits of other spacecrafts were designed to avoid radiation damage.

The features of the Jovian radiation belt observed by the spacecrafts are discussed in the following section.

Flux distribution of the Jovian radiation belt

Fig. 25 shows the contour of iso-counting rate of omni-directional electron with E> 21 MeV, which represents the structure of the radiation belt (Van Allen, 1974). The contour is extrapolated from the observed points along the Pioneer 10 and 11 paths assuming that the structure is uniform for the dipole magnetic field. There is no slot region which divides the inner and outer radiation belts as can be seen on the earth.

The cross section of Fig. 25 at the magnetic equator is shown in Fig. 26 (Van Allen, 1976). The inner edge of the radiation belt measured by Galileo probe was 1.35 R_J for all

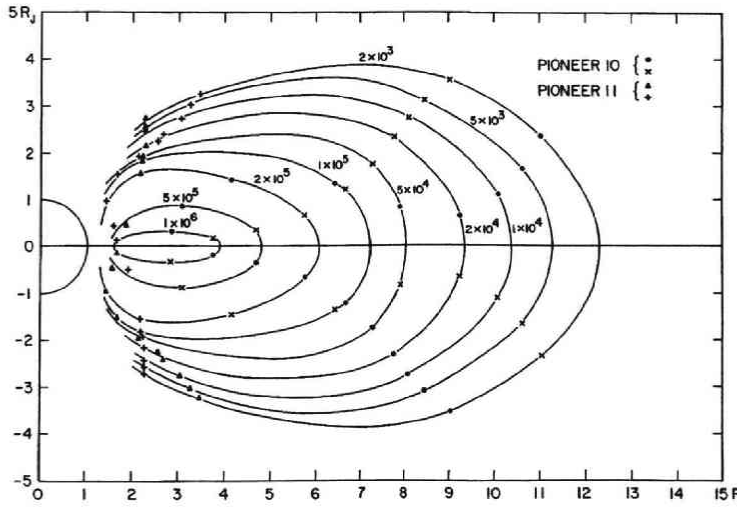

Fig. 25. Iso-counting rate contour of omni-directional electrons with E>21 MeV, which represents the structure of the radiation belt (Van Allen, 1976).

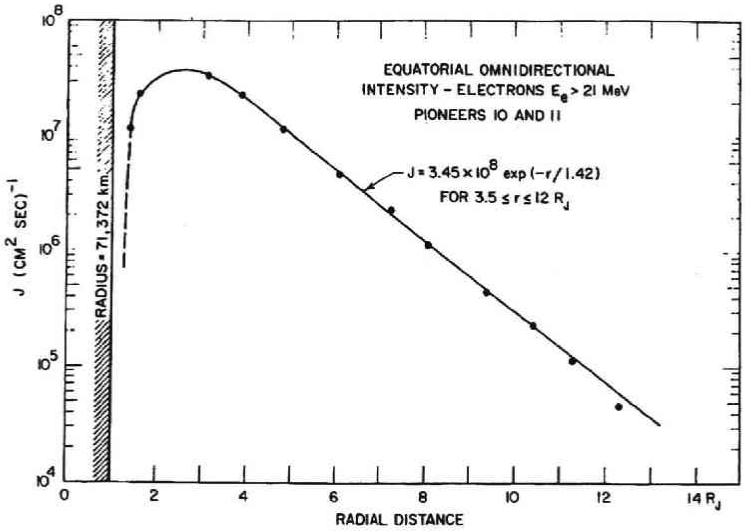

Fig. 26. Cross section of Fig. 25 along the magnetic equator (Van Allen, 1976).

particle species (Fischer *et al.*, 1996).

Energy spectrum of the Jovian radiation belt

The energy spectrum at various L-values is shown in Fig. 27 (Baker and Van Allen, 1976). The hardening of energy spectrum as the L-values decreases represents the existence of some strong acceleration mechanism in the inner magnetosphere.

Time variation of hot electron

Galileo spacecraft observed some time-variations of energetic particles with energies of several hundreds keV, which are injected from the outer magnetosphere and become possible to be detected at the satellite orbit around Jupiter. For example, dynamic injection and dispersion of the energetic particles at $L=11$ (Mauk *et al.*, 1997) and longitudinally confined charged particle injection like substorm on the Earth (Mauk *et al.*, 1999) are reported and argued in the relation with the dynamics of the Jovian magnetosphere.

In-situ observation of JSR

The *in-situ* observation of Jovian synchrotron radiation was carried out by repeating raster scans of Cassini primary communication antenna from the distance of 149 R_J by Bolton *et al.* (2002) (Fig. 28, see page 80). The observed frequency was 13.8 GHz, which corresponds to the concerning electron energy of 50 MeV as can be obtained from Equation (28). The existence of these ultra relativistic electrons with higher energies than previously believed, was confirmed for the first time.

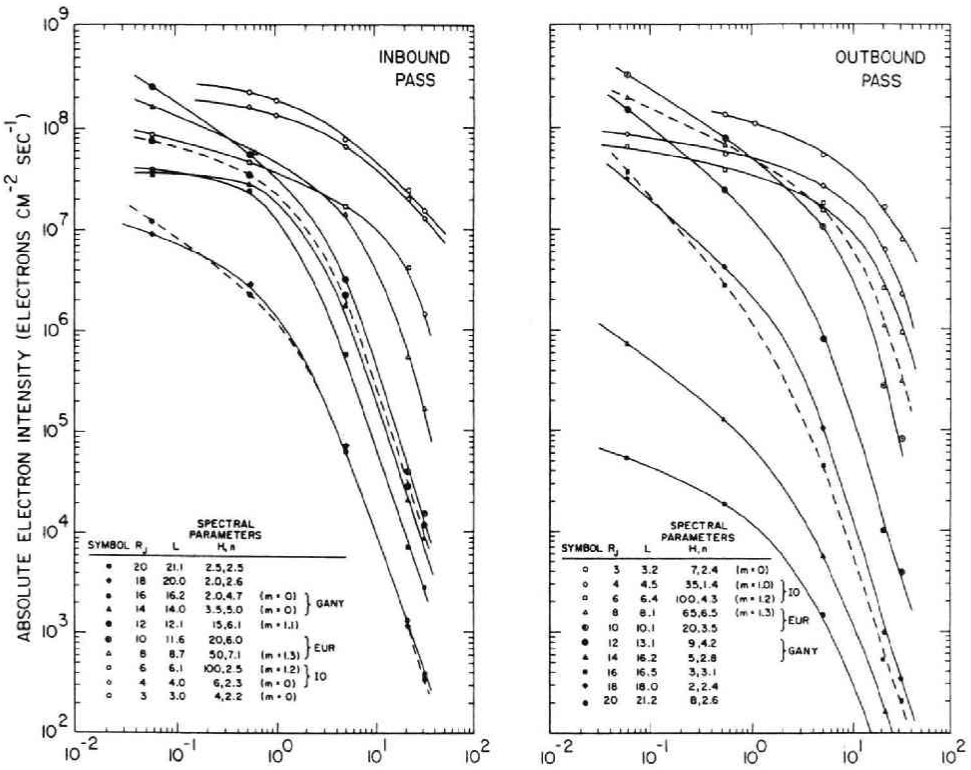

Fig. 27. Energy spectrum for various L-values for inbound pass (left) and outbound pass (right) of Pioneer 10. The hardening of spectrum as L-value decreases represents the existence of acceleration (Baker and Van Allen, 1976).

3.2 Necessity of remote sensing of the Jovian radiation belt

In-situ observation of the distribution and its dynamics of the energetic particles has a fundamental difficulty of separating time variation from special distribution. So many observation reports treated that there is no time variation with respect to velocity of spacecraft. the Galileo spacecraft, which became a satellite of Jupiter, can reveal the time variation separating from special distribution by means of accumulation of a lot of orbit data around Jupiter. However the detected features are restricted to the vicinity of the satellite orbit. In particular for the case of Jupiter, it is impossible to measure relativistic particles by *in-situ* observations due to the radiation damage by the relativistic particles themselves. Thus it is important for the study of the Jovian radiation belt to perform the ground-based remote sensing of the Jovian synchrotron radiation (JSR) emitted from the relativistic electrons.

In order to discuss the time variation of JSR with the time scale of days to weeks, a continuous observation is necessary. However it is generally impossible to make continuous observations by using a common use antenna because of the machine time. This is because we develop an exclusive observation system for the the Jovian

synchrotron radiation. To develop the observation system by ourselves has also an importance to establish basic techniques for a future interferometric observation which can image the 2-dimensional Jovian synchrotron radiation distribution.

Note that the inner radiation belt on the Earth also has a time variation of few days. Up to 90's the radiation belts on the Earth have been thought to be static and stable. However, recent *in-situ* observations have been revealing the dynamical feature of the radiation belts. The dynamic feature of the inner and outer radiation belts observed by the CRRES spacecraft is shown in Fig. 29 (see page 80) (Baker *et al.*, 1994).

3.3 Antennas for JSR

3.3.1 Required specifications for the JSR observation

The observation system must have a sufficient sensitivity to detect the time variation of JSR. Minimum detectable sensitivity of a receiving system is defined by comparing the levels between the fluctuation of the signal, ΔT_{RMS}, and the amplitude increased from the average level of a star, ΔT_{star}, (Fig. 30), where T in Kelvin. The signal power is represented in wattes/Hz as;

$$w=kT \tag{40}$$

where k is Boltzmann's constant (1.38×10^{-23} [J/K]). The output power of kT is equal to the output power of the resistor with the temperature of T and also equal to the output power of an antenna surrounded by blackbody with the temperature of T.

Fluctuation of signal (ΔT_{RMS}) is proportional to the background level (T_{sys}) and inversely proportional to $\sqrt{\Delta f\tau}$ by statistical effect, where Δf and τ are the bandwidth of the signal and time constant of the signal integration of the receiver, respectively. The product of Δf and τ becomes an single quantity because the signal of bandwidth Δf has a correlation with a time of $1/\Delta f$. So ΔT_{RMS} can write as

$$\Delta T_{RMS}=\frac{T_{sys}}{\sqrt{\Delta f\tau}} \tag{41}$$

Increased signal level of the star with flux density of S is described as,

$$w=\frac{SA_e}{2} \tag{42}$$

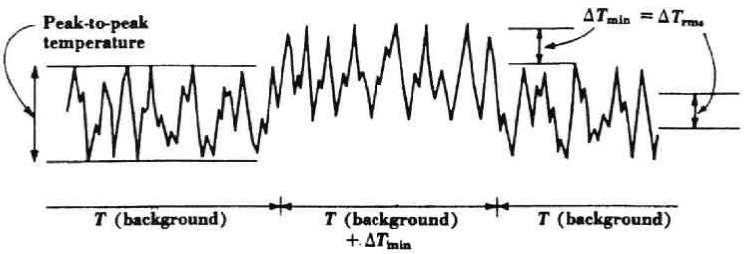

Fig. 30. The basic idea of minimum sensitivity. The minimum sensitivity is determined by comparing ΔT_{RMS} and T_{star} (Kraus, 1986).

where S and A_e are the source flux density in Jy ($=10^{-26}$ watts $m^{-2}Hz^{-1}$) and the effective aperture of antenna in m^2, respectively, and the factor of 1/2 means the output of one polarization component of the radio wave. So ΔT_{star} can be expressed from Equation (40) and (42) as

$$\Delta T_{star}=\frac{SA_e}{2k} \tag{43}$$

From Equation (41) and (43), the minimum detectable sensitivity ΔS can be written by the following equation as the source flux density is derived from $\Delta T_{RMS}=\Delta T_{star}$,

$$\Delta S|_{S/N=1}=\frac{2kT_{sys}}{A_e\sqrt{\Delta f\tau}} \tag{44}$$

Thus, the minimum detectable sensitivity of the system can be calculated.

3.3.2 Basic design of the observation system

First of all, the observation frequency was determined to be 327 MHz. The frequency range from 322 to 328.6 MHz is a protected band for 'Notification of use for the radio astronomy (Kraus, 1986). In this frequency band a line spectrum of atomic Deuterium maser is included at 327 384 352.5222 Hz (Wineland and Ramsey, 1972). Moreover, the frequency range of the observation is determined considering the energy spectrum of the Jovian radiation belt and its emission frequency. From Equation (28), the electron energy having most contribution to 327 MHz emission is obtained to be 21 MeV, which roughly corresponds to the major energy component in Jovian radiation belt.

In the following, each term of Equation (44) is discussed to estimate the required specifications of the receiving system for the observation of JSR at 327 MHz.

System noise temperature T_{sys} is originated by some noise sources, and the noise temperatures of each source depend on frequency as shown in Fig. 31. System noise temperature in our frequency range is decomposed to a galactic noise (T_{sys}) and the receiver noise (T_{RX}) in main, i.e.,

$$T_{sys}=T_{sky}+T_{RX} \tag{45}$$

The radiation from Earth's atmosphere (T_{atm}) can be negligible in this frequency range. From Fig. 31, T_{sky} is obtained to be about 100 K. As for T_{RX}, the noise temperature of the designed front-end circuit is estimated to be 80 K. Note that T_{sky} has a distinct structure as a function of the galactic coordinate (top panel of Fig. 32, see page 81), which can be convert to the celestial coordinate (bottom panel of Fig. 32). Moreover the T_{sky} has a power law relation as function of frequency as,

$$T_{sky}\propto f^{-\beta} \tag{46}$$

with $\beta=2.5$ (P. Reich and W. Reich, 1988).

The bandwidth Δf is set to be 10 MHz considering the protected band width and the actual artificial interference noise band at the Zao site.

The integration time τ is set to be 10 sec as a typical value.

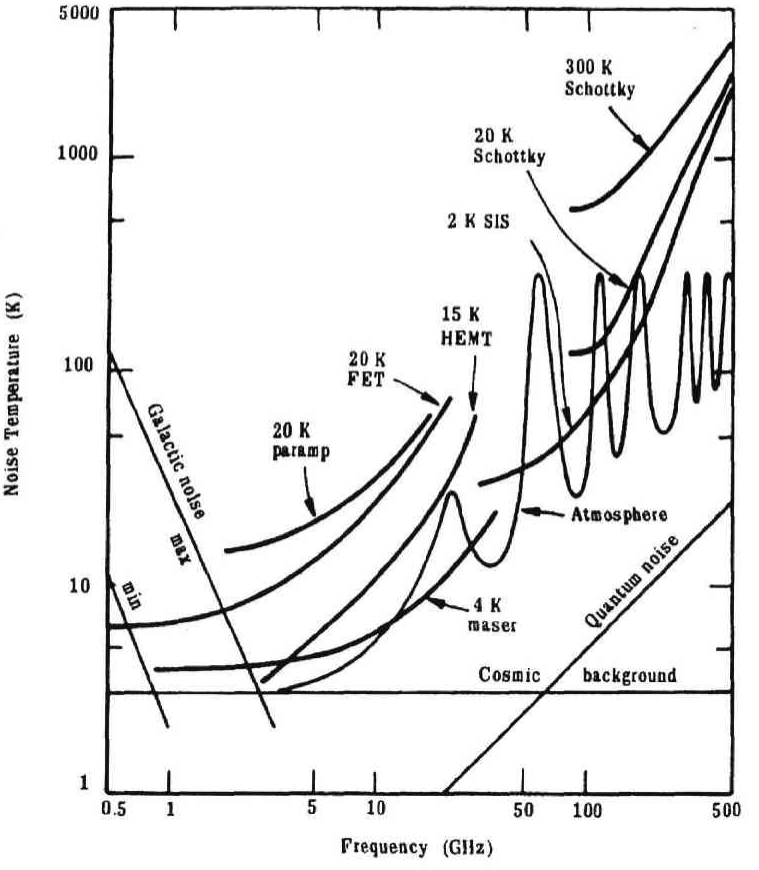

Fig. 31. The components of system temperature as a function of frequency (Kraus, 1986).

Table 2. The estimation of the term in Equation (44) to derive the sufficient antenna aperture (A_e) for JSR observation.

integration time	τ	10 sec
system temperature	T_{sys}	180 K
bandwidth	Δf	10 MHz
sensitivity	ΔS	0.2 Jy
effective aperture area	A_e	400 m^2

Based on these values, it is calculated from Equation (44), that the effective aperture area A_e of 400 m^2 is required to achieve the sensitivity of 0.2 Jy, which is about 1/5 of the amplitude of the beaming curve (Fig. 10). The specific values of designed system are listed in Table 2.

The effective aperture area A_e of 400 m^2 is equivalent to a dish parabolic antenna

with diameter of 27 m if its aperture efficiency is 0.7. In order to achieve the required aperture area of the antenna, we adopt the way of the aperture synthesis. In practice, 9 antennas whose individual effective aperture area is 40 m^2 are used to achieve the required aperture area.

The 9 antennas are allocated to form a 'Y'-formation, considering that the side-lobe comes to cancel for the direction of southern sky. The comparison between the synthesized beam pattern for 'Y' and the cross formation is shown in Fig. 33 The side lobe level

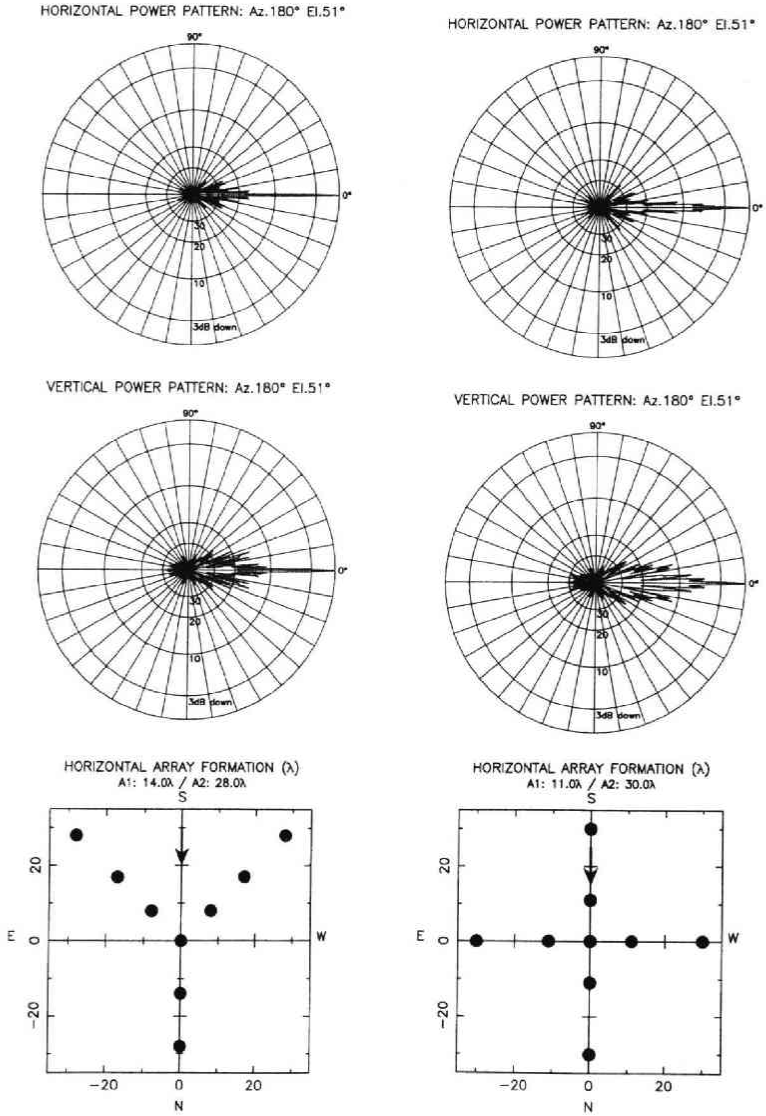

Fig. 33. The comparison of synthesized beam pattern for Y (left panel) and cross (right panel) formation. The difference is seen in the side lobe level.

Table 3. Comparison of antenna for JSR.

	Place	Type	Main object	Frequency	Aperture area
Zao	Miyagi, Japan	Aperture synthesis array	JSR	327 MHz	380 m²
IPRT	Fukushima, Japan	Two parabolic surface	JSR	325, (790)MHz	700 m²
Usuda[a]	Nagano, Japan	Dish parabora ϕ 64 m	Satellite tracking	S, X	2,252 m²
Kashima[b]	Ibaragi, Japan	Dish parabora ϕ 32 m	VLBI	S, X	564 m²
STE[c]	Nagano, Japan	Cylindrical parabora	IPS	327 MHz	1,400 m²
JPL[d]	U.S.A	Dish parabora ϕ 30 m	Satellite tracking	S	500 m²
Nancay[e]	France		Radio astronomy	1.4, 1.7, 3.3 GHz	
EISCAT[f]	Norway	Dish parabora ϕ 32 m	Rader	930 MHz	
VLA[g]	U.S.A	Dish parabora 25 m×27	Radio astronomy	70, 300 MHz, L, S, X	
ATCA[h]	Australia	Dish parabora ϕ 22 m×6	Radio astronomy	L, S	

[a]http://www.isas.jaxa.jp/
[b]http://www2.crl.go.jp/ka/
[c]http://www.stelab.nagoya-u.ac.jp/
[d]http://www.jpl.nasa.gov/
[e]http://www.obs-nancay.fr/
[f]http://www.eiscat.com/
[g]http://www.vla.nrao.edu/
[h]http://www.narrabri.atnf.csiro.au/

is clearly diminished in 'Y' compared with the cross formation. In designing the system, various formation was tried and finally 'Y' formation was adopted.

A calibration system is essential for the system to add the signal from each antenna in-phase.

3.3.3 Comparison with other antennas

The antenna systems which have been used for the observation of JSR are listed in Table 3. The antennas except for Zao and IPRT are not for JSR observation as the primary purpose, and have made JSR observation not continuously but intermittently. Moreover the advantage of our antenna system is its beam width. The beam width of the array type antenna has a sharp one, which is important to separate Jupiter from background galactic structure.

4 Development of the observation system

The observation system is built in the Zao observatory of Planetary Plasma and Atmospheric Research Center (latitude : 38°06′ West longitude : 140°32′ altitude : 685 m).

The observation system consists of 9 independent antennas, which are arranged to form a 'Y'-formation array. Each antenna has a front-end unit whose signal is combined with the signals from the other antennas and sent to the back-end system. The observation system also has a calibration system to keep the relatively constant gain and phase differences, by means of the loop-method. Moreover, each antenna has an antenna driver unit to control the antenna direction, and equips a communication unit to control the observational parameters between the front-end and antenna control unit.

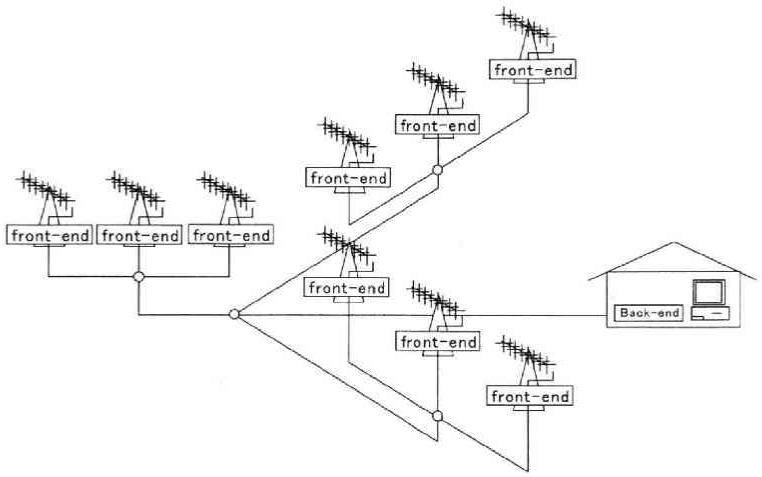

Fig. 34. Schematic view of the observation system. The system consists of 9 antennas. Each antenna has the front-end system. The signals from 9 antennas are combined and sent to the back-end. The system also equips the calibration system, antenna control unit, and communication unit.

The schematic view of the observation system is shown in Fig. 34. In the following section details of each unit are shown.

4.1 System for signal receiving

4.1.1 Antenna

The type of each antenna is 4×2 stacked 27 element cross YAGI antenna. The photo of an antenna unit is shown in Fig. 35 (see page 82), and structure and structural parameters of antenna are shown in Fig. 36.

The type of pick-up is a half wavelength folded dipole (named 'DRV' in Fig. 36), whose impedance is higher than the typical half wavelength dipole antenna (about 73 Ω).

The impedance of the antenna including the elements ('REF' and 'D01', ..., 'D25' in Fig. 36) is calculated to be about 100 Ω. The impedance matching between the Yagi antenna and the cable of 50 Ω is achieved using $1/4\lambda$ cable of 75 Ω (Fig. 37). The $1/4\lambda$ cable with impedance of Z_0' satisfies a function of converting impedance,

$$Z_0'^2 = RZ_0 \tag{47}$$

where R and Z_0 are input and output impedance values. In this case, input impedance of 100 Ω is converted to nearly equal to 50 Ω ($=75^2/100$).

The signals received by each pick-up is combined to one signal through the combiners as shown in Fig. 38 (see page 82). A cable from one pick-up to the final combiner is made to attain the same electrical length as other cables. Mutual difference of cable length is finally achieved to be less than 0.5 degree.

The calculated beam pattern of the antenna unit referring to the antenna configuration shown in Fig. 36 is shown in Fig. 39. The half power beam width (HPBW)

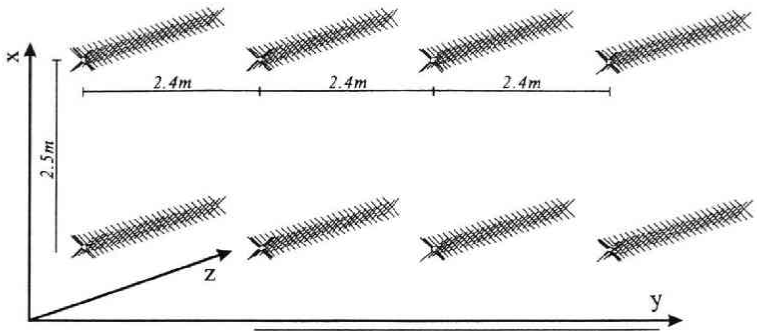

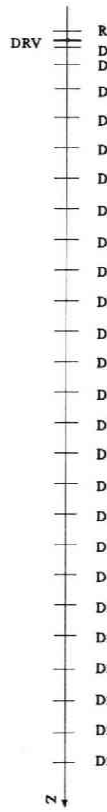

Element	length[mm]	spacing[mm]
REF	450	–
DRV	432	104
D01	419	77
D02	410	180
D03	398	267
D04	393	310
D05	393	327
D06	386	332
D07	386	332
D08	383	332
D09	376	332
D10	376	332
D11	376	332
D12	376	332
D13	376	332
D14	359	332
D15	359	332
D16	359	332
D17	351	332
D18	351	332
D19	351	332
D20	351	332
D21	351	332
D22	351	332
D23	351	341
D24	351	352
D25	351	319

Fig. 36. Form of each antenna unit in the rectangular coordinates The x, y, and z are the horizontal, vertical, and beam directions, respectively.

of the antenna unit is obtained to be 4.8° for the azimuth direction and 9.6° for the elevation direction. The antenna gain for the isotropic antenna G is 27.7 dBi, which is equivalent to an effective aperture A_e of 39.4 m², where G and A_e have a relation of

$$G=\frac{4\pi}{\Omega_A} \tag{48}$$

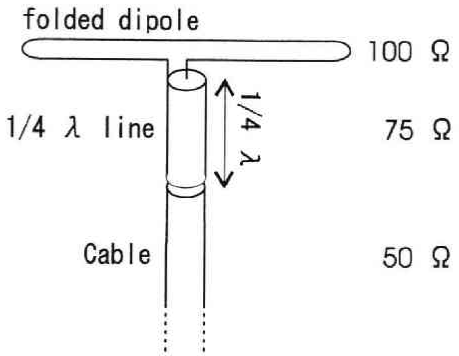

Fig. 37. Schematic plot of a pick-up, which converts the radio wave signal to the electric current in the coaxial cable. The type of pick-up is a folded dipole with $1/4\lambda$ impedance conversion line to match the antenna impedance to the coaxial cable impedance of 50 Ω.

$$=\frac{4\pi A_e}{\lambda^2} \tag{49}$$

where Ω_A is a solid angle of main beam and has a relation of

$$\lambda^2=A_e\Omega_A \tag{50}$$

4.1.2 Front-end

The front-end is an assembly of electric circuits consisting of following 4 units. The each circuit is made using micro strip line with 3 mm width on an glass-epoxy board whose thickness is 1.6 mm. The characteristic impedance of the micro strip line is 50 Ω and characteristic wavelength on the board is 48.9 cm. Fig. 40 (see page 82) shows the photo of the front-end, and Fig. 41 shows the schematic of the front-end.

(a) Relay unit

Relay unit has a function to select an input port such as signal from antenna, signal from calibration circuit, and termination of input port. Switching of signal is performed by a mechanical relay ARK111/ARK131 (MATSUSHITA), which is driven by an open-corrector logic IC. Relays (1)-(5) are driven by the control signal through the communication unit as listed in Table 4.

(b) Low noise amplifier unit

The function of Low noise amplifier (LNA) unit is to amplify the input signal with extremely low noise level, and to select the particular RF bandwidth. The first amplifier, which determine the whole noise of the system, is made of NE7618A (NEC) which is Gallium-Arsenic field effect transistor (GaAs FET), having the lowest noise characteristics in the UHF frequency range. Also we use 2SC4093 (NEC) and μPC2709 (NEC) as second and third amplifiers.

The circuit diagram of the low noise amplifier unit consisted of NE7618A and its peripheral devices is shown in Fig. 42.

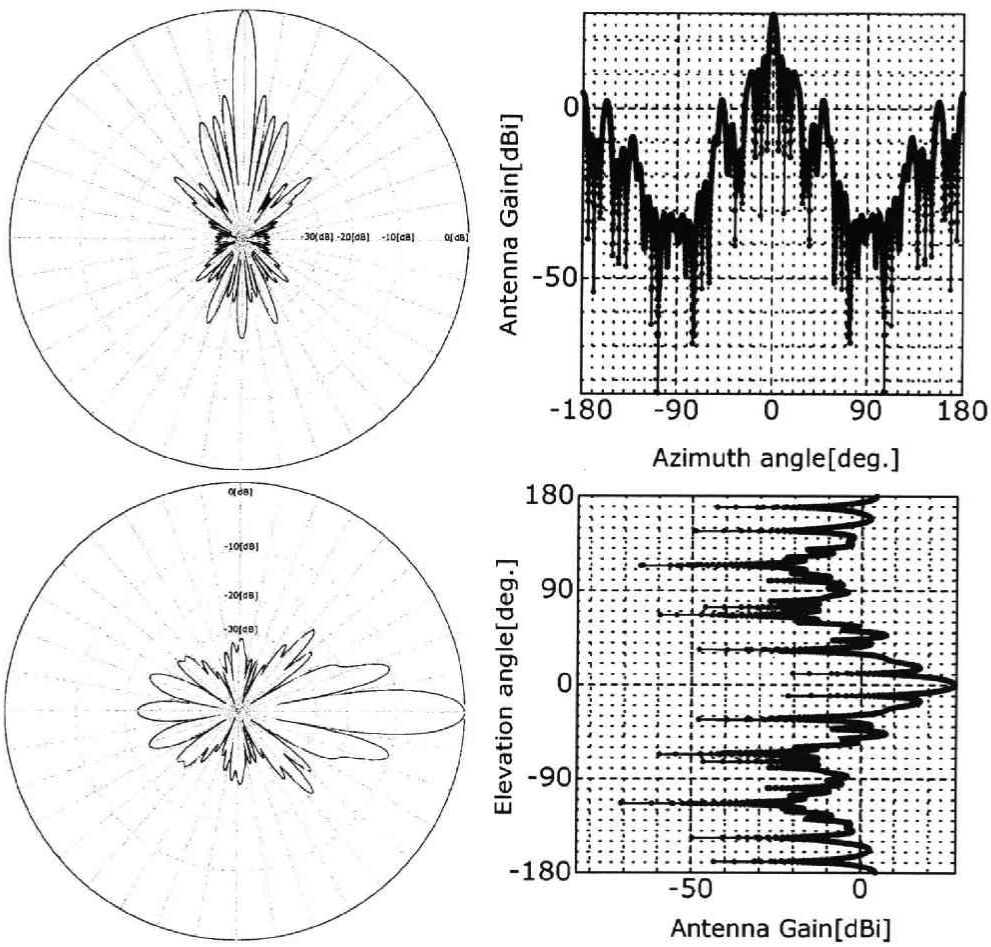

Fig. 39. Calculated beam patterns for the azimuth (top panels) and elevation (bottom panels) directions in the polar coordinates (left panels) and the rectangular coordinates (right panels). In the polar coordinates, the power is normalized by main beam. In the rectangular coordinates, the power is displayed in dBi unit.

(c) Programable attenuator unit

Programable attenuator unit is designed to control the total gain of the front-end unit with 4 bit resolution.

The unit consists of 4 attenuators and pairs of attenuators are arranged in the following geometric ratio, i.e.,

$$\left|\begin{matrix}-0.2\text{ dB}\\ 0\text{ dB}\end{matrix}\right|+\left|\begin{matrix}-0.4\text{ dB}\\ 0\text{ dB}\end{matrix}\right|+\left|\begin{matrix}-0.8\text{ dB}\\ 0\text{ dB}\end{matrix}\right|+\left|\begin{matrix}-1.6\text{ dB}\\ 0\text{ dB}\end{matrix}\right| \tag{51}$$

Thus, arbitrary attenuation can be selected up to 3 dB with 0.2 dB step. Switching of the attenuators is performed by pin diode switch.

The programable attenuator unit is controlled by the communication unit in the

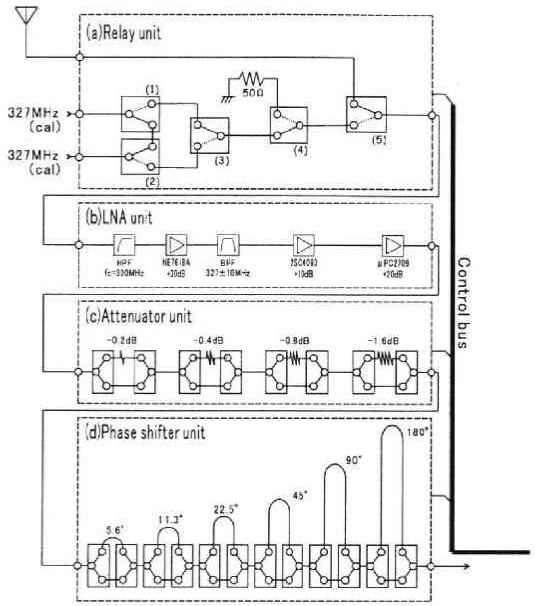

Fig. 41. Schematic plot of front-end. The front-end unit consists of (a) relay unit, (b) LNA unit, (c) programable attenuator unit, and (d) programable phase shifter unit.

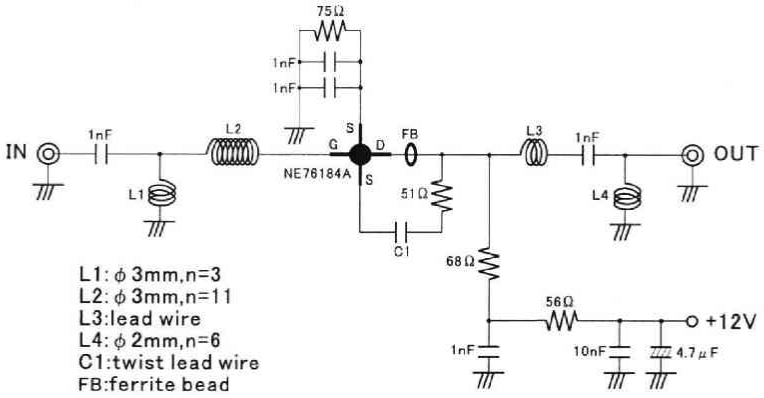

Fig. 42. Circuit diagram of the LNA unit consisted of a low noise transistor NE7618A and its peripheral devices.

digital way as listed in Table 4.

(d) Programable phase shifter unit

Programable phase shifter unit is designed to control the phase of the front-end unit with 6 bit resolution.

Phase shift is achieved by using the micro strip line as the delay line. The line length is selected to correspond to the phase delay of the wavelength on the board.

Table 4. Control items of front-end by way of Amphenor 36 pin connector. Control signal is driven by TTL level digital signal from the communination unit.

Pin	device	+5V/open	0V/short
1	PS 180	through	active
2	PS 90	through	active
3	PS 45	through	active
4	PS 22.5	through	active
5	PS 11.3	through	active
6	PS 5.6	through	active
7	AT −0.2	through	active
8	AT −0.4	through	active
9	AT −0.8	through	active
10	AT −1.6	through	active
11	relay 5	stable	active
12	relay 4	stable	active
13	relay 2, 3	stable	active
14	relay 1	stable	active
15	NC	-	-
16-36	ground	-	-

Pairs of delay lines are arranged in the following geometric ratio, i.e.,

$$\left|\begin{matrix}5.6^\circ\\0^\circ\end{matrix}\right|+\left|\begin{matrix}11.3^\circ\\0^\circ\end{matrix}\right|+\left|\begin{matrix}22.5^\circ\\0^\circ\end{matrix}\right|+\left|\begin{matrix}45^\circ\\0^\circ\end{matrix}\right|+\left|\begin{matrix}90^\circ\\0^\circ\end{matrix}\right|+\left|\begin{matrix}180^\circ\\0^\circ\end{matrix}\right| \tag{52}$$

Thus arbitrary phase delay can be selected in the range of 360° with 5.6° step. Switching is performed by pin diode switches as same as the programable attenuator unit.

The programable phase shifter unit is controlled by the communication unit in the digital way listed in Table 4.

The most important characteristic of the front-end unit is its Noise Fig. Noise Fig. (NF) is generalized value to characterize the excess noise generated in electric devices, which is defined as the degree of getting worse of SN ratio as the signal transmit the devices, i.e.,

$$NF=\frac{S_{in}/N_{in}}{S_{out}/N_{out}} \tag{53}$$

NF has a value of more than 1 in ratio or more than 0 in dB.

Under this definition, NF can also be written using intrinsic noise N_a and gain G of an amplifier as

$$NF=\frac{S_i/N_i}{GS_i/(N_a+GN_i)} \tag{54}$$

$$=\frac{N_a+GN_i}{GN_i} \tag{55}$$

Input noise power N_i is expressed using thermal noise temperature of T_0 as

$$N_i=k_BT_0B \tag{56}$$

where k_B and B are Boltzmann constant and bandwidth respectively, and T_0 is the temperature fixed to be 290 K. Also additional noise N_a which is converted to the equivalent input level can be expressed using thermal noise temperature of T_e as

$$N_a=Gk_BT_eB \tag{57}$$

where product of G means the conversion to an actual input level. Here, T_e is called (input equivalent) noise temperature. Put Equation (56) and (57) into (55),

$$T_e=(NF-1)T_0 \tag{58}$$

which describes a relationship between noise temperature T_e and NF.

Characteristics of reflection, transmission (measured by using HP: 8712B), and Noise Fig. (measured by using Agilent: N8972A) as a function of frequency are shown in Fig. 43. Distinctions of all 18 front-end unit are shown in Table 5. The typical NF is 1.22 dB which is equivalent to the noise temperature of 94 K.

Table 5. Characteristics of NF, Gain, reflection and transmission of each front-end unit.

	NF mater		Network analyzer		Install	
No.	NF [dB]	Gain [dB]	Refl. [dB]	Trans. [dB]	Ant	Pol
1	1.27	43.11	−17.38	43.32	E1	X
2	1.28	40.56	−16.28	40.63	E3	Y
3	1.31	42.60	−17.07	42.91	W1	X
4	1.26	41.29	−17.88	41.24	00	X
5	1.10	43.30	−15.71	43.36	E3	X
6	1.11	43.40	−28.00	43.44	E2	X
7	1.12	41.14	−15.25	41.04	W3	X
8	1.12	41.51	−25.59	41.14	W2	X
9	1.12	41.15	−30.19	40.98	00	Y
10	1.14	40.07	−15.22	40.01	E2	Y
11	1.34	40.62	−15.90	40.30	W1	Y
12	1.30	42.92	−16.74	42.97	W2	Y
13	1.16	41.65	−19.37	41.73	S2	X
14	1.26	42.59	−25.56	42.10	S1	X
15	1.20	42.55	−14.52	42.37	S2	Y
16	1.26	41.61	−17.84	41.81	E1	Y
17	1.10	43.30	−26.54	43.45	W3	Y
18	1.49	42.58	−18.79	42.17	S1	Y
avg	1.22	42.00	−19.66	41.94		

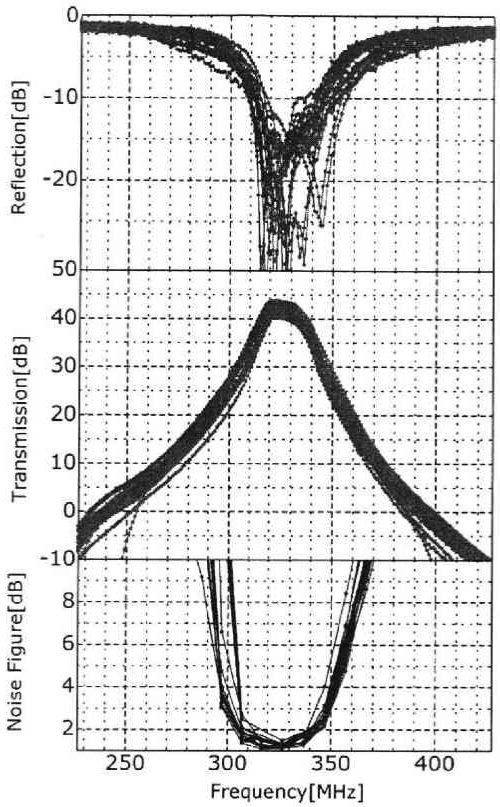

Fig. 43. Gain, Reflection, and Noise Fig. of 18 front-end units as a function of frequency.

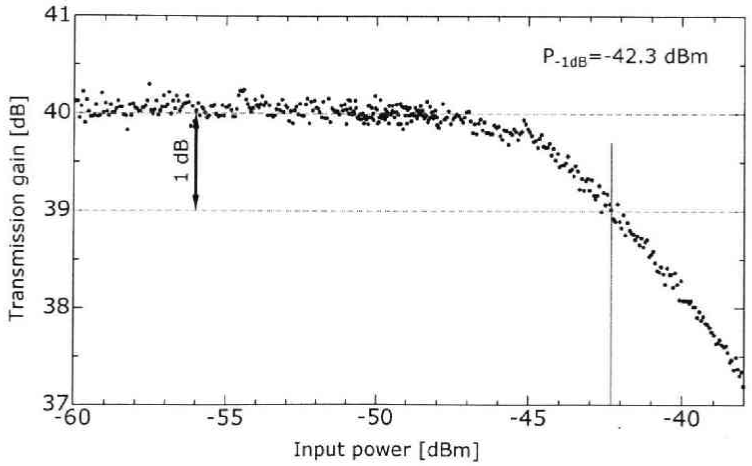

Fig. 44. Gain characteristics of the front-end unit as a function of input level, which is measured by suppression against flat gain. Saturation level (suppressed −1 dB for the flat gain) is −43 dBm.

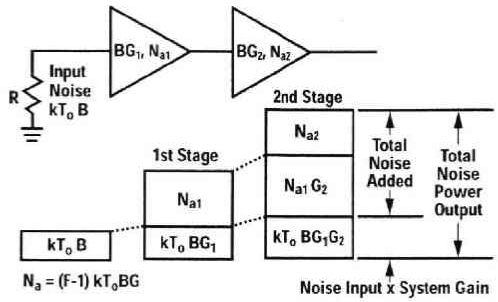

Fig. 45. Combined Noise Fig. for the cascade connection of devices. The effect of the 1st stage is most important because the effect of the 2nd stage is reduced to inverse of gain of the 1st stage [after "Fundamentals of RF and Microwave Noise Fig. Measurement" (AN 57-1), Agilent Technologies].

Characteristic of the gain as a function of input level is shown in Fig. 44. From the figure, saturation level (suppressed -1 dB for flat gain) is obtained to be -43 dBm.

4.1.3 Combination of signals

For the case of series connection of two devices, the total noise temperature of the system T_{sys} is given by

$$T_{sys}=T_1+\frac{T_2}{G_1} \tag{59}$$

where T_1 and T_2 are noise temperature values of the 1st and 2nd stage, and G_1 is the gain of the 1st stage. Because the contribution of T_2 is reduced to $1/G_1$, if G_1 is large enough, T_{sys} is almost determined by T_1. This relation can be expanded for any multi-stage system, i.e., the total T_{sys} for the n-stage system is

$$T_{sys}=T_1+\frac{T_2}{G_1}+\frac{T_3}{G_1G_2}+\cdots+\frac{T_n}{G_1G_2\cdots G_{n-1}} \tag{60}$$

or total NF is

$$NF_{sys}=NF_1+\frac{NF_2-1}{G_1}+\frac{NF_3-1}{G_1G_2}+\cdots+\frac{NF_n-1}{G_1G_2\cdots G_{n-1}} \tag{61}$$

For an attenuator with gain G $(0<G<1)$,

$$N_a=(1-G)k_BT_{LP}B \tag{62}$$

Put Equation (56) and (62) into Equation (55)

$$NF=1+\frac{T_{LP}}{T_0}\left(\frac{1}{G}-1\right) \tag{63}$$

For the case of $T_{LP}=T_0$,

$$NF+\frac{1}{G} \tag{64}$$

The loss before the amplifier is significant, because the noise temperature concerning to

Table 6. Details of system gain, *NF*, and system temperature T_e. The combined system temperature is calculated to be about 120 K.

device	G/unit	unit	G [dB]	*NF* [dB]	*T*	T_e
cable1	−0.24	1	−0.24	0.24	16.48	16.48
front-end	40.00	1	40.00	1.22	93.90	99.23
cable2	−0.18	24	−4.28	4.28	486.14	0.05
3-combine	−1.03	1	−1.03	1.03	77.62	0.02
cable3	−0.18	31	−5.52	5.52	744.28	0.27
3-combine	−1.03	1	−1.03	1.03	77.62	0.10
hyb-amp	23.30	1	23.30	3.95	430.11	0.70
cable4	−0.18	75	−13.36	13.36	5997.23	0.05
sum			37.84			116.89

the loss is directly fed in the front-end.

In our system, signals from each antenna are combined as shown in Fig. 46 (see page 83). The calculated system temperature for the system is shown in Table 6. The combined system temperature is about 120 K.

4.1.4 Back-end

The back-end unit has functions of frequency down-conversion to IF frequency, filtering of the IF signal, and amplification of the IF signal. The signals are fed to the power meter (HPE4418A, Hewlett Packard). The level of the power meter is read by personal computer (PC9821RAII23, NEC) through GPIB bus. Schematic diagram of back-end is shown in Fig. 47 and measured transmission characteristics at each stage as a function of IF frequency are shown in Fig. 48. The bandwidth of back-end, which determines the bandwidth of the entire system, is 10 MHz.

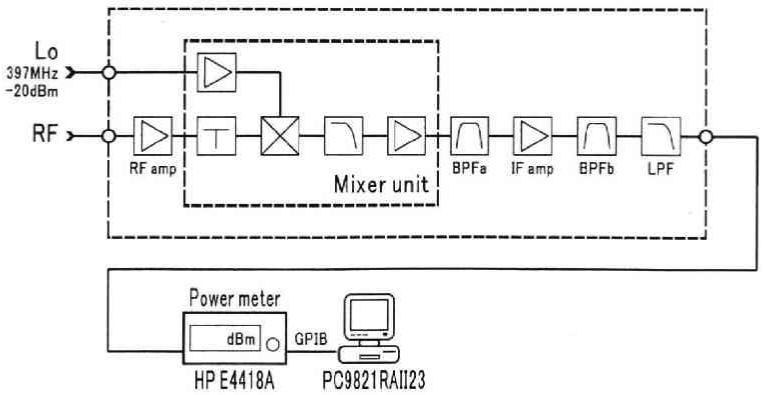

Fig. 47. Schematic diagram of back-end.

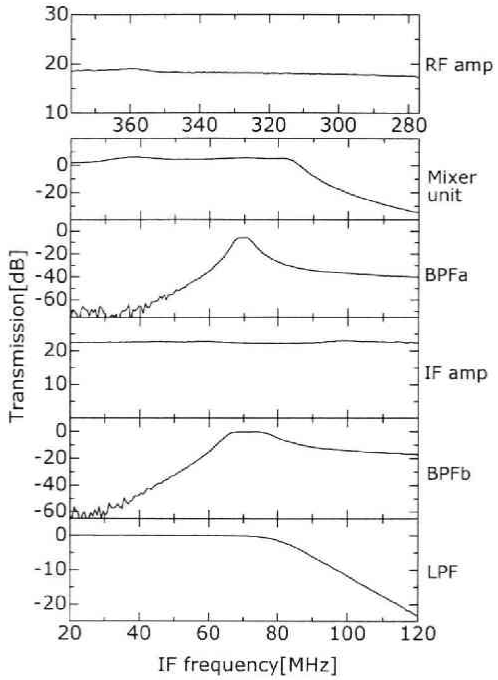

Fig. 48. Frequency characteristics at each stage of the back-end.

4.2 System for phase and gain calibrations : the loop-method

To synthesize the signals from 9 antennas in-phase (see Fig. 34), the gain and phase shift arised in the front-end unit should be calibrated.

The loop-method is a way to measure the relative phase and gain differences of signals between the amplifier and combining point. This method is possible to avoid the influence of calibration cable by means of the 4 path calibrations in the loop.

4.2.1 Principle of loop-method

Synoptic circuit for the two amplifiers is shown in Fig. 49. For this case, a calibration signal from the oscillator at 327 MHz is transmitted through 4 paths (a-b1-fe1-d1-e, a-b2-c-fe1-d1-e, a-b1-c-fe2-d2-e, and a-b2-fe2-d2-e) to the Vector Voltmeter (8508A, HP) which measures relative phase and gain (Fig. 50). Denoting the measured 4 phases as $P1$, $P2$, $P3$, and $P4$, the phase components in each path are given by

$$
\begin{aligned}
P1 &= P(a)+P(b1)+ \quad P(fe1)+P(d1)+P(e)-P(ref)\\
P2 &= P(a)+P(b2)+P(c)+P(fe1)+P(d1)+P(e)-P(ref)\\
P3 &= P(a)+P(b1)+P(c)+P(fe2)+P(d2)+P(e)-P(ref)\\
P4 &= P(a)+P(b2)+ \quad P(fe2)+P(d2)+P(e)-P(ref)
\end{aligned}
$$

where $P(x)(x=a,\ b1,\ b2, \ldots)$ is a phase value of path x.

By operation of $(P1+P2)-(P3+P4)$, the phase originating from the calibration

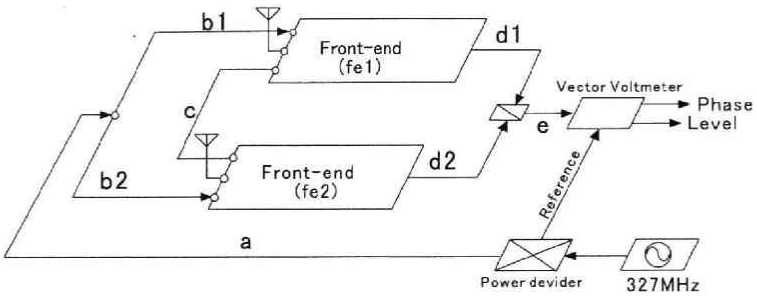

Fig. 49. Schematic circuit of the loop-method. The case of two amplifiers is illustrated for the simplicity.

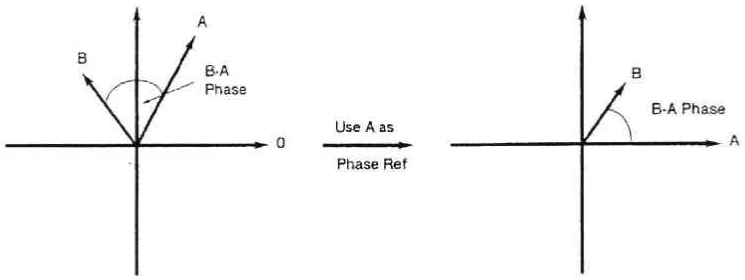

Fig. 50. Description of Vector Voltmeter. Vector Voltmeter measures the voltage of two CW signals and the phase difference between them [after "Operating and Service Manual" (HP 8508A)].

cable path (i.e., a and e) and loop path (i.e., $b1$, $b2$, and c) are canceled. Then the intrinsic phase differences due to the front-end unit (ΔP_{fe}) and the attached cable which is used to connect between the front-end unit and the power combiner (ΔP_d), are obtained from the following procedure.

$$\frac{(P1+P2)-(P3+P4)}{2}=\Delta P_{fe}+\Delta P_d \tag{65}$$

$$\Delta P_{fe}=P(fe1)-P(fe2) \tag{66}$$

$$\Delta P_d=P(d1)-P(d2) \tag{67}$$

Considering that the phase measurement includes the ambiguity of 2π and operation of divide by 2 in Equation (65), the result of the loop-method includes the ambiguity of π.

The gain difference between two front-ends is also performed by the same way as the phase calibration, i.e.,

$$\begin{aligned}
L1&=L(a)+L(b1)+ \quad L(fe1)+L(d1)+L(e)-L(ref)\\
L2&=L(a)+L(b2)+L(c)+L(fe1)+L(d1)+L(e)-L(ref)\\
L3&=L(a)+L(b1)+L(c)+L(fe2)+L(d2)+L(e)-L(ref)\\
L4&=L(a)+L(b2)+ \quad L(fe2)+L(d2)+L(e)-L(ref)
\end{aligned}$$

$$\Delta L_{fe}=L(fe1)-L(fe2) \tag{68}$$
$$\Delta L_{d}=L(d1)-L(d2) \tag{69}$$

where $L(x)$ $(x=a, b1, b2, ...)$ is a signal level of path x.

4.2.2 Application to nine antennas

The layout of the loop calibration circuit for the case of nine antenna is shown in Fig. 51. The three loops are formed for three branches (S-branch, E-branch, and W-branch). All loops include the same amplifier of antenna [00] which is the reference point to measure relative gain and phase. The attenuator of 8.5 dB is set to cancel the level difference between up and down paths.

As mentioned above, the calibration signal is fed into two opposite directions, which is described up/down in Fig. 51. For example, at the case of the time of the measurement of [S1] X front-end, the paths of calibration signal are

Up path : ([00]X)→([00]Y)→ [S1]X front-end
Down path : ([S2]Y)→([S2]X)→([S1]Y)→[S1]X front-end

where ( ) indicates a transit front-end unit.

Level diagram for each path is shown in Table 7. The maximum and minimum levels are −22 dB([S2]-down) and 43 dB([E3]-up, [00]E-down), respectively. The

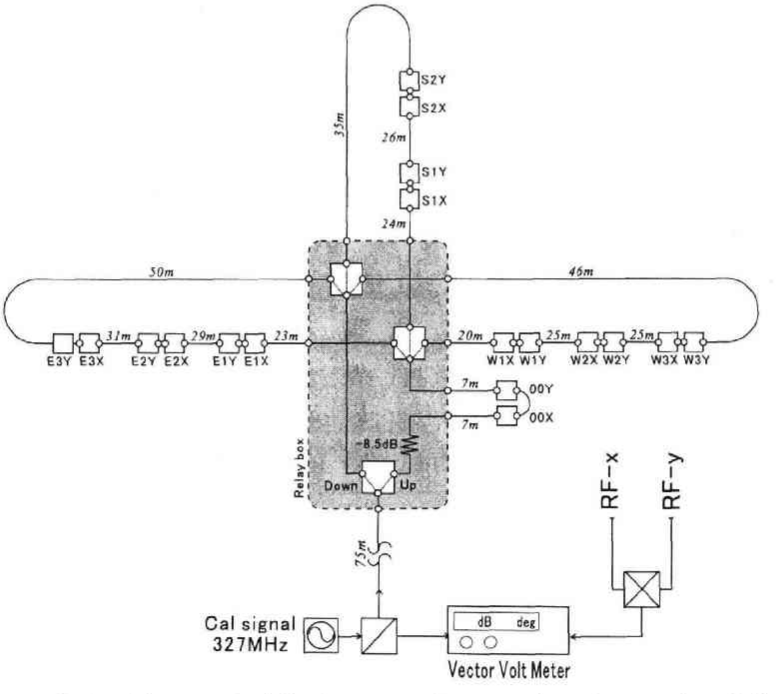

Fig. 51. Path of loop-method for 9 antenna. there are three loops and each loop includes [00] antenna as a reference.

Table 7. Level diagram for the loop-method for each path.

S branch up					E branch up					W branch up				
	gain/unit	unit	gain	sum		gain/unit	unit	gain	sum		gain/unit	unit	gain	sum
5D-2V	−0.17	5	−0.9		5D-2V	−0.17	5	−1		5D-2V	−0.17	5	−0.9	
5D-2V	−0.17	70	−12		5D-2V	−0.17	70	−12		5D-2V	−0.17	70	−12	
AT	−8.5	1	−8.5		AT	−8.5	1	−9		AT	−8.5	1	−8.5	
5D-2V	−0.17	7	−1.2		5D-2V	−0.17	7	−1		5D-2V	−0.17	7	−1.2	
@00				−22.44	@00				−22.44	@00				−22.44
5D-2V	−0.17	7	−1.2		5D-2V	−0.17	7	−1		5D-2V	−0.17	7	−1.2	
5D-2V	−0.17	24	−4.1		5D-2V	−0.17	23	−4		5D-2V	−0.17	20	−3.4	
@S1				−27.71	@E1				−27.54	@W1				−27.03
5D-2V	−0.17	26	−4.4		5D-2V	−0.17	29	−5		5D-2V	−0.17	25	−4.3	
@S2				−32.13	@E2				−32.47	@W2				−31.28
					5D-2V	−0.17	31	−5		5D-2V	−0.17	25	−4.3	
					@E3				−37.74	@W3				−35.53

S branch down					E branch down					W branch down				
	gain/unit	unit	gain	sum		gain/unit	unit	gain	sum		gain/unit	unit	gain	sum
5D-2V	−0.17	5	−0.9		5D-2V	−0.17	5	−1		5D-2V	−0.17	5	−0.9	
5D-2V	−0.17	70	−12		5D-2V	−0.17	70	−12		5D-2V	−0.17	70	−12	
5D-2V	−0.17	35	−6		5D-2V	−0.17	50	−9		5D-2V	−0.17	46	−7.8	
@S2				−18.7	@E3				−21.25	@W3				−20.57
5D-2V	−0.17	26	−4.4		5D-2V	−0.17	31	−5		5D-2V	−0.17	25	−4.3	
@S1				−23.12	@E2				−26.52	@W2				−24.82
5D-2V	−0.17	24	−4.1		5D-2V	−0.17	29	−5		5D-2V	−0.17	25	−4.3	
5D-2V	−0.17	7	−1.2		@E1				−31.45	@W1				−29.07
@00				−28.39	5D-2V	−0.17	23	−4		5D-2V	−0.17	20	−3.4	
					5D-2V	−0.17	7	−1		5D-2V	−0.17	7	−1.2	
					@00				−36.55	@00				−33.66

proper level of reference signal is calculated to be between $P_{min}=-42$ dBm and $P_{max}=-28$ dBm based on the following estimation. The input threshold level of Vector Voltmeter and upper limit level of the front-end unit are 47 dBm and 50 dBm respectively, and the gain after the front-end unit is 38 dB (see Table 6). Thus we obtain,

$$P_{min}=-47+43-38=-42 \text{ dBm} \tag{70}$$

$$P_{max}=-50+22=-28 \text{ dBm} \tag{71}$$

4.2.3 Example of the loop-method

In the loop-method calibration procedure, the phase values for all front-end units are first adjusted using the programable phase shifter. The results are shown in Fig. 52 (see page 83) where (a) and (b) denote the measured values before and after the phase adjustment. Then, the gain values for all front-ends are adjusted using the programable attenuator. The final level and phase are shown by (c) in Fig. 52. The ambiguity of π in the phase measurement is seen in [00] and [E1] antennas. The gain values of all front-end units are adjusted to be within 0.2 dB, and the relative phase values of all front-end units are adjusted to be within 9° though the phase values include the ambiguity of π.

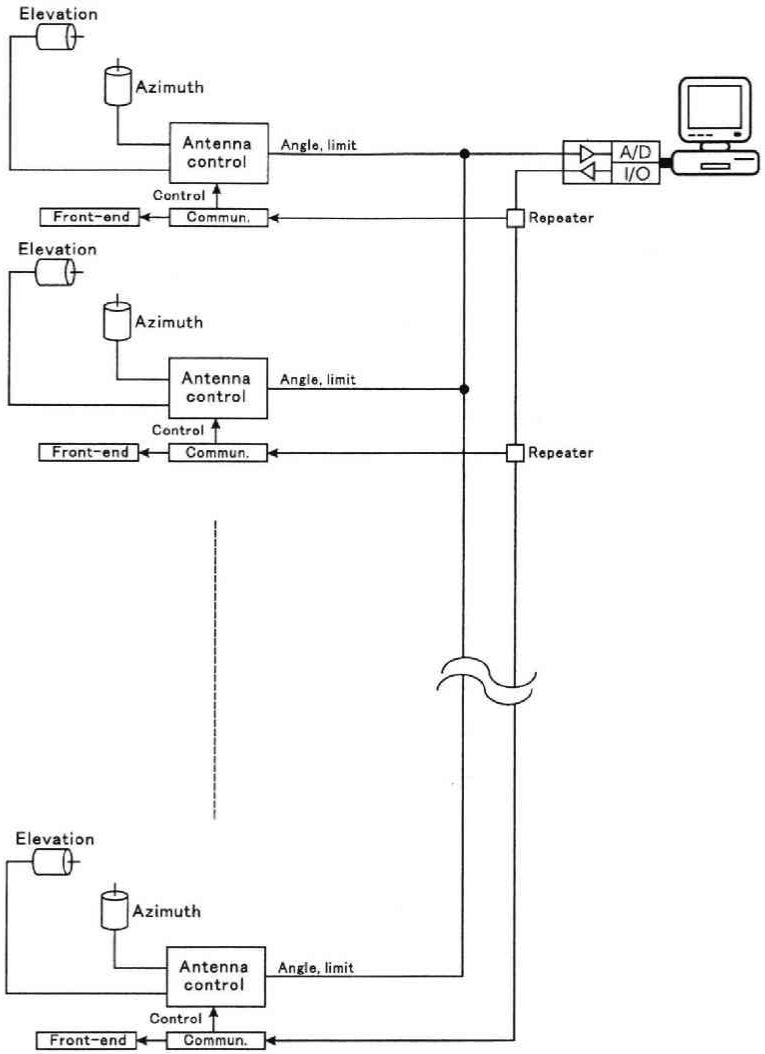

Fig. 53. Diagram of the antenna control unit and communication unit.

4.3 System for antenna control

The antenna driving unit has a function to direct the antenna to an object. The schematic of the antenna driving unit is shown in Fig. 53, which consists of units for antenna angle reader and motor driver. The antenna angle reader detects the voltage (0-10 volt) of the potentio-meter which is proportional to azimuth and elevation angles, and also detects the signal concerning to antenna limit positions. The circuit of antenna driving unit is shown in Fig. 54 (see page 84). These data are sent to the control PC. The antenna control unit controls the driving motors for azimuth and elevation via the communication unit.

Table 8. Control command format of 24 bit serial data.

Antenna	76543210	Device	76543210	Data	76543210
00	00000000	X-Relay	00000100	obs	00001011
S1	01000000	Y-Relay	00000000	50ohm	00000011
S2	01001000			cal-A	00000110
E1	00100000			cal-B	00000101
E2	00101000	X-Ps	00000110	0.0	00000000
E3	00110000	Y-Ps	00000010	5.6	00000001
W1	01100000			⋮	⋮
W2	01101000			354.4	00111111
W3	01110000	X-At	00000101	0.0	00000000
		Y-At	00000001	−0.2	00000001
				⋮	⋮
				−3.0	00001111
		azimuth	00000011	CW/UP	******* 0
		elevation	00000111	CCW/DOWN	******* 1
				speed 0	0000111 *
				speed 1	0000110 *
				⋮	⋮
				speed 7	0000000 *

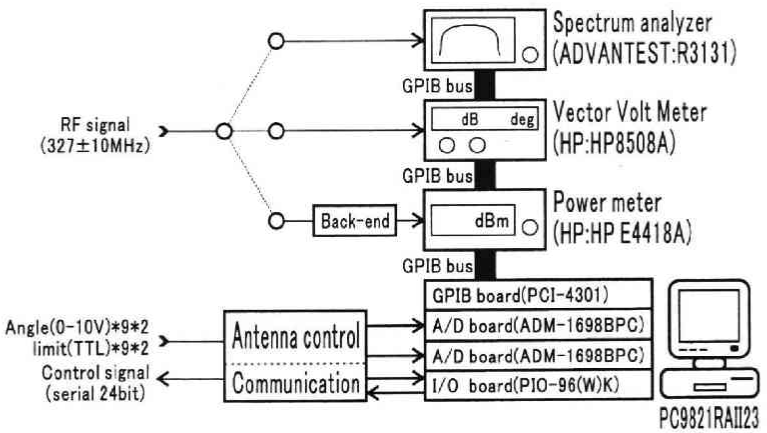

Fig. 55. Schematic diagram of control of the system using a personal computer. The PC system is adopted to control all the system intensively.

4.4 System for communication

The communication unit is a digital system to control the front-end and antenna driving units. The data set on I/O address port of control PC is converted to a serial signal of 24 bit, and send to each antenna. The serial signal of 24 bit consists of antenna address (8 bit), device address (8 bit), and data (8 bit), whose details are listed in Table 8.

The data received at each antenna is decoded to a parallel signal, and compared with each antenna address. If the data match to the address of an antenna unit, the control signals are read out as a significant one for the antenna unit.

4.5 Control by software on PC

All the systems including the antenna control, communication, and data acquisition

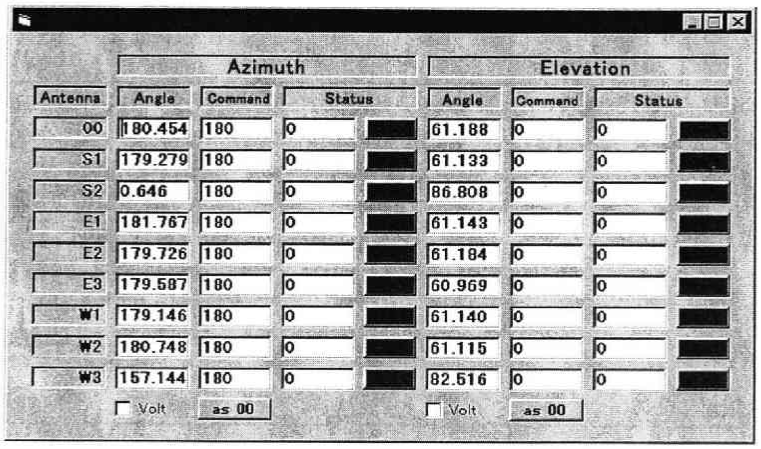

Fig. 56. The screen capture of the software to control the antenna direction. Each row corresponds to each antenna and each column indicates the current angle, commanded angle, and current status for azimuth and elevation, respectively.

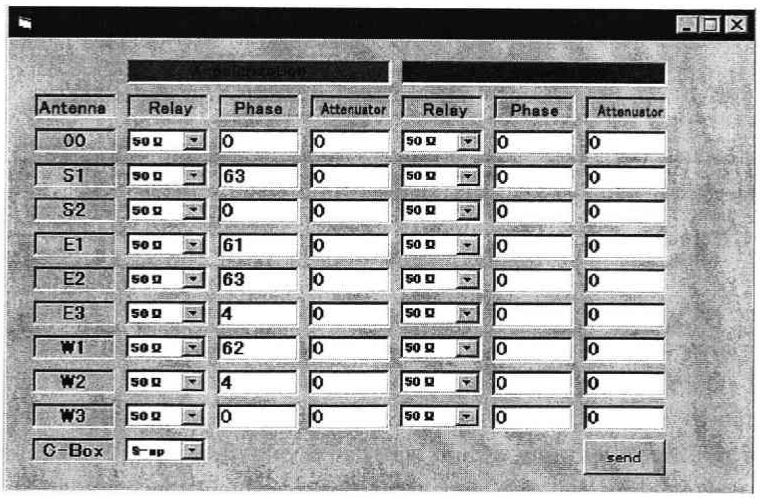

Fig. 57. The screen capture of the software to control signal. Each row corresponds to each antenna and the column indicates the relay control, programable phase shifter control, and programable attenuator control for each polarization, respectively.

unit are controlled by a personal computer (PC9821RAII23, NEC). The PC and peripherential configuration are shown in Fig. 55. Examples of control function on PC are shown in Fig. 56 for the antenna direction control and Fig. 57 for the front-end parameter control. On the controlling an antenna direction, the program calculates the difference between current angle and commanded angle, and drives the motor to close to the commanded angle with varying speed of the motor ('trapeziform control').

5 Measurements of intrinsic parameters for synthesizing of signals

In order to combine signals from 9 antennas in-phase, it is necessary to measure intrinsic parameters involved in the system. For the simple case of 2 antennas, combination of signals from each antenna is written as

$$P(\theta)=p(\theta)\left\{\left\langle\frac{\cos\omega t+\cos(\omega t+\phi)}{2\cos\omega t}\right\rangle\right\}^2 \tag{72}$$

$$=p(\theta)\left(\frac{1+\cos\phi-\langle\tan\omega t\,\sin\phi\rangle}{2}\right)^2 \tag{73}$$

$$=p(\phi)\left(\frac{1+\cos\phi}{2}\right)^2 \tag{74}$$

where $P(\theta)$, $p(\theta)$, and ϕ are synthesized beam pattern, single antenna beam pattern, and phase difference between two antennas, respectively, and $\langle\ \rangle$ means to take time average of the value. The term $\cos\phi$ is called an array factor. The schematic plot of Equation (72) is shown in Fig. 58 (see page 84).

Each antenna beam $p(\theta)$ must be direct to a target radio source accurately. The axial calibration of the antenna will be described in section 5.1.

The array factor $\cos\phi$ also must be direct to a target radio source. The phase differences ϕ can be decomposed into four terms; geometric delay (ϕ_{geo}), eigen phase

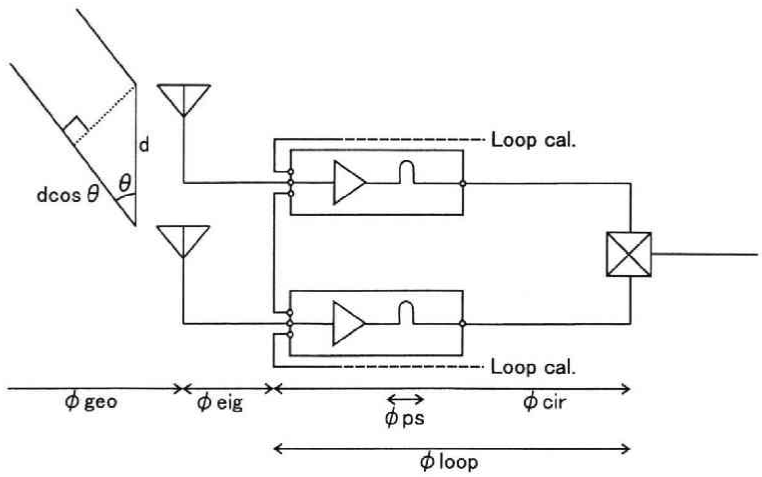

Fig. 59. Phase differences between an incoming radio wave and the signal output at the combination point.

(ϕ_{eig}), circuit (ϕ_{cir}), and phase shifter (ϕ_{ps}). $\phi_{cir}+\phi_{ps}$ can be measured by the loop-method (ϕ_{loop}). The relations of ϕ_{geo}, ϕ_{eig}, ϕ_{cir}, ϕ_{loop}, and ϕ_{ps} are written as

$$\phi=\phi_{geo}+\phi_{eig}+\phi_{cir}+\phi_{ps} \tag{75}$$

$$\phi_{loop}=\phi_{cir}+\phi_{ps} \tag{76}$$

where delay (ϕ_{geo}) is optical path difference, eigen phase (ϕ_{eig}) is phase difference due to the cable path difference in the antenna sections, circuit (ϕ_{cir}) is phase difference of the front-end circuit, phase shift (ϕ_{ps}) is shifted phase by the phase shifter. The ϕ value is taken to be positive, when the wave front arrives earlier compared with the reference antenna. The relation is illustrated in Fig. 59.

ϕ_{geo} can be geometrically calculated based on antenna position and position of target source in the sky, i.e.,

$$\phi_{geo}=\frac{delay}{\lambda}2\pi \tag{77}$$

$$delay=\vec{n}\cdot\vec{B} \tag{78}$$

$$=|\vec{B}|\cdot\cos\theta \tag{79}$$

$$=l\cdot x+m\cdot y+m\cdot z \tag{80}$$

where $\vec{n}=(l, m, n)$ and $\vec{B}(x, y, z)$ are unit vectors directed to the star and baseline vectors respectively. $\vec{n}$ can be written using direction cosine of the azimuth angle (az) and elevation angle (el) of a radio source as

$$\begin{bmatrix} l \\ m \\ n \end{bmatrix}=\begin{bmatrix} \cos el\cdot\cos az \\ \cos el\cdot\sin az \\ \sin el \end{bmatrix} \tag{81}$$

Thus the accurate measurement of antenna position ($\vec{B}=(x, y, z)$) is required, which will be described in section 5.2.

The eigen phase angle ϕ_{eig} is not constant for all antennas because the cable length between the signal pick-up element of the antenna and the signal input point to the front-end is not always same due to variation of environmental temperature and the relative position of the antenna mounting is not constant among 9 antennas. The determination of ϕ_{eig} will be described in section 5.3.

Once ϕ_{geo}, ϕ_{eig}, and ϕ_{cir} are determined, phase differences caused by our system itself are canceled using the phase shifter (ϕ_{ps}) in the front-end.

5.1 Calibration of antenna axis

The calibration of antenna axis adjusts the output voltage of angle measuring instrument of the antenna (hereafter 'angular voltage') with antenna beam direction, which is required to control the antenna direction accurately. Because each beam of elevation and azimuth direction of the antenna is broad, it is possible to calibrate the azimuth and elevation direction axes independently.

Table 9. Result of axial calibration for azimuth and elevation. The relation between the angle and angular voltage is coordinated by linear function of $y=ax+b$, where y and x are angle and angular voltage, respectively.

	Elevation		Azimuth	
Antenna	a	b	a	b
00	10.205	−2.51	−38.937	384.04
S1	10.291	−2.77	−39.073	368.08
S2	9.975	−19.49	−39.375	385.34
E1	10.219	−18.02	−39.995	364.56
E2	10.041	−10.85	−40.194	379.94
E3	10.157	−15.43	−39.586	374.73
W1	10.134	−20.53	−40.430	380.14
W2	10.140	−15.47	−38.808	377.31
W3	10.272	−8.88	—	—

Elevation direction

Axial calibration for the elevation direction was made using a slant gauge, i.e., we measured the antenna direction against gravitational vertical. The angle of 2 pipes (east and west side), which aligns along the beam direction, was measured at 4 elevation angles including upper and lower limit positions. The obtained angle versus output angular voltage is shown in Fig. 60 (see page 85).

The deviation from the fitted line is within 1°, which is negligible compared with the elevation beam width (about 8°). Moreover, it is confirmed that the electrical beam also directs to a target source, from the observation of the sun at the time of its culmination.

The obtained relations between elevation angle and angular voltage are shown in Table 9.

Azimuth direction

After the axial calibration of elevation, the axial calibration for azimuth was made using the sun as a reference radio source. At first, the azimuth angle is roughly arranged. Then, we directed the antenna to the direction of −30 minutes and +30 minutes with respect to the sun culmination, when the sun moves in the almost horizontal direction. By fitting the observed beam profile to the Gaussian function, we can determine the accurate time when the sun past the center of the antenna beam. Using the calculated two azimuth angles at the time of culmination ±30 minutes, the relation between azimuth angle and output angular voltage was obtained. The case of antenna [00] is shown in Fig. 61.

The obtained relations between azimuth angle and voltage are shown in Table 9.

5.2 Measurement of antenna position

We used a 3-D surveying instrument, Total Station (TOPCON corporation), to

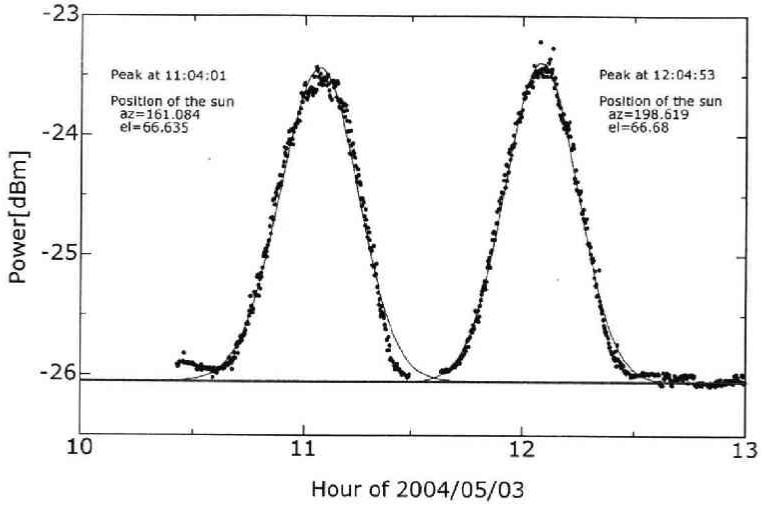

Fig. 61. Example of the azimuth axis calibration for [00] antenna. Using two measurements near culmination ±30 minutes for the sun, the relation between the azimuth angle and angular voltage is coordinated by linear function.

measure each antenna position. Total Station derives the position of a target-reflector in x, y, and z coordinate from the measured azimuth, elevation, and radial distance of the target, by means of the propagation time measurement of near-infrared beam reflected from the target.

The measurement was carried out by following two steps to obtain the relative position of each antenna with respect to the [00] antenna and to align the coordinate of the antenna array to geometrical north-south line.

For the first step, the position of the top of the azimuth axial pipe aligned the zenith (z) direction was measured in relative x, y, and z coordinate, with the target reflector. This measurement was carried out four times, by which the RMS error became less than 1 mm. Height differences (Δz) between the top of the azimuth axial pipe and antenna mount point were also measured.

For the second step, the angle between the geometrical north and [00] [S2] line, θ, was measured using Polaris. This was made by measuring the azimuth angle between Polaris and the direction of the line forming by a couple of target reflectors at the tops of [00] and [S2] antennas.

The coordinate obtained by the two step measurements can be written using matrix as

$$\begin{bmatrix} x' \\ y' \\ z' \end{bmatrix} = \begin{bmatrix} \cos\theta & -\sin\theta & 0 \\ \sin\theta & \cos\theta & 0 \\ 0 & 0 & 1 \end{bmatrix} \begin{bmatrix} x \\ y \\ z \end{bmatrix} + \begin{bmatrix} 0 \\ 0 \\ \Delta z \end{bmatrix} - \begin{bmatrix} x_0 \\ y_0 \\ z_0 \end{bmatrix} \tag{82}$$

where (x_0, y_0, z_0) is position of [00] antenna, which is defined as the origin of the coordinate. The result is shown in Table 10 and Fig. 62.

Table 10. Positions of nine antennas in the x, y, and z coordinate.

	x'	y'	z	Δz	z'
00	0.000	0.000	0.000	−0.185	0.000
S1	12.813	−0.006	0.446	−0.215	0.416
S2	27.492	−0.094	0.825	−0.115	0.895
E1	−9.692	8.746	0.180	−0.247	0.118
E2	−19.285	17.473	0.296	−0.200	0.281
E3	−28.877	26.174	0.226	−0.020	0.391
W1	−9.616	−8.686	0.143	−0.164	0.164
W2	−19.261	−17.347	0.397	−0.267	0.315
W3	−28.868	−26.009	0.881	−0.597	0.469

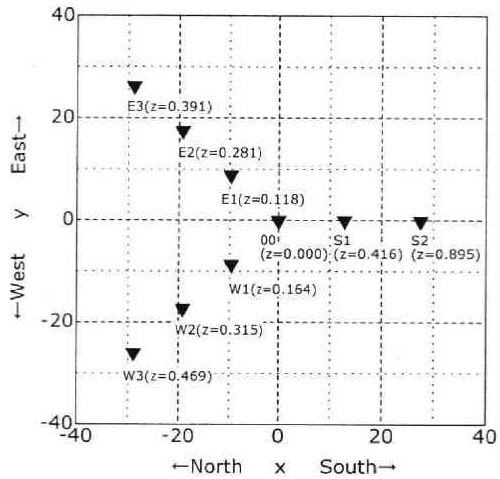

Fig. 62. Positions of 9 antennas in the x(South) - y(East) plain. The zenith positions (z) are also shown beside each antenna (filled triangles). The angle between South and [00]-[S2] line is 0.2° ([S2] is located slightly west).

5.3 *Measurement of eigen phase of each antenna*

The measurement of eigen phase was made using the sun. Basically we have only to measure the relative eigen phase with respect to the reference antenna. Thus, the fundamental way to measure the eigen phase is as follows. The two antennas were directed to the sun and phase shifter was swept from 0° to 360°. When the signals from two antennas become in-phase with some phase-shift angle, the output power has a maximum. Then we can determine the relative eigen phase value between two antennas, after the subtraction of the phase difference ϕ_{geo} due to the optical path difference between two antennas.

In practice, the correlation analysis between $P(t)$ and cos $\phi(t)$ was carried out, where $P(t)$ is an observed fringe, cos $\phi(t)$ is a calculated fringe, and $\phi(t)$ is a term of time

variable phase;

$$\phi(t)=\phi_{geo}+\phi_{ps} \tag{83}$$

$$\phi_{ps}=-\mathrm{PCM}/64\times 2\pi \tag{84}$$

where PCM is a decimal number (0-63) to determine amount of the phase shift. The negative sign of Equation (84) means that the delay line is inserted. Because the best correlated phase offset ϕ_0 has a relation of

$$\phi(t)+\phi_0=2n\pi \tag{85}$$

ϕ_{eig} is obtained using the relation of Equation (75)

$$\phi_{eig}=\phi_0-\phi_{cir} \tag{86}$$

where ϕ_{cir} is the measured value by the loop-method when ϕ_{ps} is zero (PCM=0).

The correlation function $R(\phi)$ can be defined as

$$R(\phi)=\int P(t)\cos(\phi(t)+\phi)dt \tag{87}$$

which is cosine transform of $P(t)$. Thus we can rewrite this equation using Fourier transform as

$$R(\omega)=\int_{-\infty}^{\infty}P(t)e^{-j\omega t}dt \tag{88}$$

$$=\int_{-\infty}^{\infty}P(t)\cos\omega t dt+j\int_{-\infty}^{\infty}P(t)(-\sin\omega t)dt \tag{89}$$

The amplitude $|R(\omega)|$ and the phase offset $\phi(\omega)$ are

$$|R(\omega)|^2=\left(\int_{-\infty}^{\infty}P(t)\cos\omega t dt\right)^2+\left(\int_{-\infty}^{\infty}P(t)(-\sin\omega t)dt\right)^2 \tag{90}$$

$$\phi(\omega)=\arctan\frac{\int_{-\infty}^{\infty}P(t)(-\sin\omega t)dt}{\int_{-\infty}^{\infty}P(t)\cos\omega t dt} \tag{91}$$

respectively. The correlation measurement was made by 5° step, and the best phase offset was obtained.

The pairs of antennas to measure the relative eigen phase were selected to construct the nearest baseline, in order not to resolve the sun, because the sun is not a point source but has a structure of bright limb at 327 MHz (see Fig. 63). The shortest baseline is about $13\lambda(\lambda/D=4.4°)$, which is enough to treat the sun as a point source. However, when we use the [00]-[E3] baseline of $43\lambda(\lambda/D=1.3°)$, it resolves the sun whose diameter is about 0.5°. Thus, we select combinations of the nearest baseline pair and then converted the measured value to the comprehensive eigen phase value.

An example of the measurement is shown in Fig. 64. The measurement was carried out by switching the phase shifter with 22.5° step sequentially by means of the PC control and storing the combined signal level to PC in parallel. The result of the measurements of eigen phase is shown in Table 11.

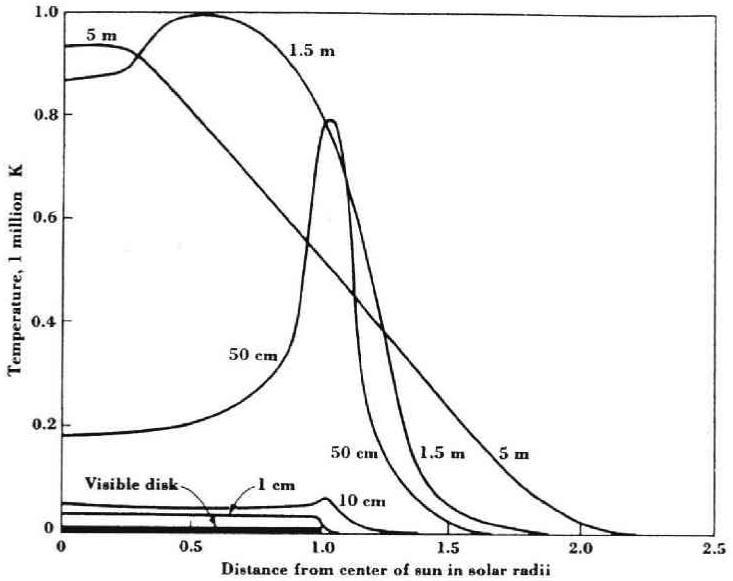

Fig. 63. Brightness distribution of the sun for various wavelength values. From wavelength of 50 cm to 1 m, the limb of the sun is brightest (Kraus, 1986).

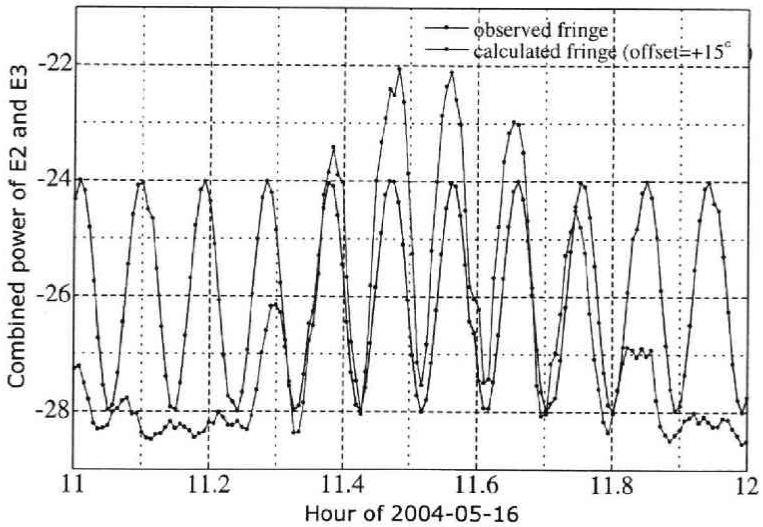

Fig. 64. Example of the observation to measure a eigen phase between the [E2] and [E3] antennas. From correlation analysis between observed fringe and calculated fringe, phase offset is acquired.

Table 11. Measured eigen phase using the sun. The denotation "A−>B" means the relative phase of antenna B against antenna A.

phase offset				ϕ_{loop}	ϕ_{eig}
00−>S1	−60	00−>S1	−60	9	291
S1−>S2	—	00−>S2	—	—	—
00−>E1	−25	00−>E1	−25	50	285
E1−>E2	−5	00−>E2	−30	50	280
E2−>E3	+15	00−>E3	−15	55	290
00−>W1	−40	00−>W1	−40	49	271
W1−>W2	+25	00−>W2	−15	66	279
W2−>W3	-	00−>W3	—	—	—

5.4 Calculation of synthesized beam

Synthesized beam pattern $P(\theta)$ as a function of angle θ can be calculated by summation of signals from each antenna taking account for phase differences, i.e.,

$$P(\theta)=\left[\sum_{n=1}^{9} e_n(\theta)\right]^2 \tag{92}$$

where $e_n(\theta)$ is a electric field for a signal of n^{th} antenna in complex number.

The complex components of $e_n(\theta)$ is weitten as

$$R_e[e_n(\theta)]=e(\theta)\cdot\cos[\phi_n(\theta)-\phi_n(0)] \tag{93}$$

$$I_m[e_n(\theta)]=e(\theta)\cdot\sin[\phi_n(\theta)-\phi_n(0)] \tag{94}$$

where $e(\theta)$ is a electric field pattern of each antenna and $\phi_n(\theta)$ is a phase difference for n^{th} antenna, which can be derived from Equation (77)-(81). For the direction of beam center ($\theta=0$), phase difference is always zero for all antenna, i.e. in-phase. This corresponds to the adjustment of phase by the set of phase shifter. The example of calculation of synthesized azimuth beam at 45° elevation is shown in Fig. 65 (see page 86).

6 Performance test of the observation system

6.1 Noise temperature of receiver (T_{RX})

The Y-factor method is a way to measure the receiver noise temperature (T_{RX}). The measurement is performed using the standard noise source (346B, Agilent), which outputs two temperatures by ON/OFF of power supply of 28 Volt (Fig. 66).

The two temperatures of the noise source ON (T_h) and noise source OFF (T_c) which is equivalent to ambient temperature T_{amb}, have relation as

$$ENR=\frac{T_h-T_c}{290} \tag{95}$$

where *ENR* is called excess noise ratio. The accurate calibrated value of ENR is provided from the manufacturer for every product. The ENR value (in dB) of 346 B

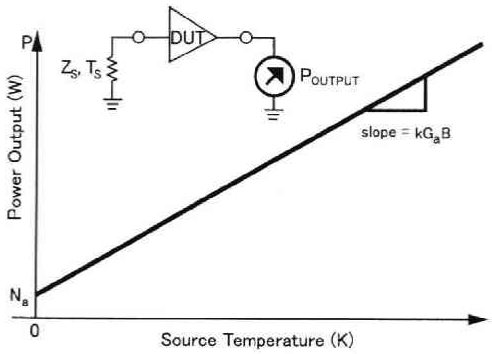

Fig. 66. Principle of the Y-factor method. The line in the graph is determined by the two independent measurements; i.e., measurements for noise source ON and OFF. The slope and section of the acquired line represent the gain and additional noise of measured device, respectively [after "Fundamentals of RF and Microwave Noise Fig. Measurement" (AN 57-1), Agilent Technologies].

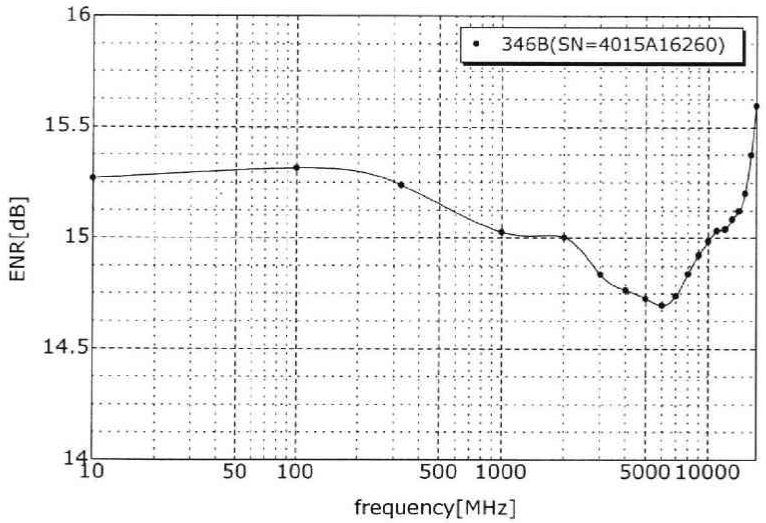

Fig. 67. The ENR value of 346 B (SN=4015A16260) as a function of frequency, which is calibrated every product.

(SN=4015A16260) is shown in Fig. 67 as a function of frequency. By interpolation, the ENR value at 327 MHz is derived to be 15.238 dB, and then $(T_h - T_c)$ is estimated to be 9,687 K. The inputted power of T_h is estimated to be about -160 dBm/Hz.

In the Y-factor method, the measurement is made for the cases of T_h and T_c inputs. The output power for T_h-input is set to P_h, which can be written as

$$P_h = kG\Delta f(T_h + T_{RX}) \tag{96}$$

also the output power P_c for T_c input can be written as

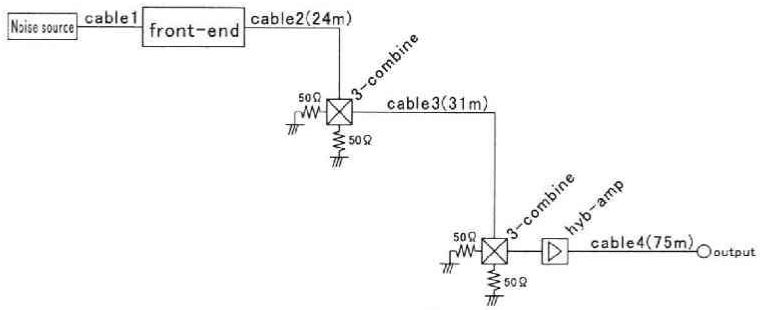

Fig. 68. Configuration of NF measurement at the front-end with the Y-factor method.

$$P_c = kG\Delta f(T_c + T_{RX}) \tag{97}$$

where G and Δf are the gain and bandwidth of the whole system (including back-end), respectively. By taking the ratio of Equation (96) and (97),

$$T_{RX} = \frac{T_h - YT_c}{Y-1} \tag{98}$$

where Y is

$$Y = \frac{P_h}{P_c} \tag{99}$$

The calculation of T_{RX} (Equation (98)) is not dependent on G and Δf, but determined only by measurement of Y. Also by taking the difference of Equations (96) and (97),

$$G = \frac{P_h - P_c}{k\Delta f(T_h - T_c)} \tag{100}$$

In application to the system, the measurement of Y-factor was carried out as shown in Fig. 68 revised from Fig. 46. Unused ports of 3-port combiners are terminated with pure resistor of 50 Ω.

In this measurement, the level diagram changed because the gain and Noise Fig. of the 3-port combiner is displaced to 5.8 dB and 6.4 dB, respectively. By this effect, the derived system temperature T'_{RX} comes to 26 K higher than T_{RX} because of the loss before the front-end (16 K) and the loss at the 3-port combines (10 K), i.e., T'_{RX} is expressed as

$$T'_{RX} = T_{RX} + 26K \tag{101}$$

The result of the measurements is shown in Table 12. T_{RX} is consistent with the value measured in the laboratory within a deviation of about 10 K. The deviation may be originated from the weak artificial noise at the time of measurements because the measurement to determine the line in Fig. 66 is very sensitive even for small level fluctuation. Gain is also consistent with the value measured by the loop-method within a deviation of 0.5 dB. Gain by the loop-method is exactly measured at 327 MHz but the gain measured by the Y-factor method is averaged in the pass-band. The difference

Table 12. Noise temperature and gain measured with the Y-factor method, and comparison with the laboratory NF measurement and the loop-method measurement. T'_{RX} is apparent receiver noise temperature including cable loss. G_a, G_r, and G_l are absolute gain, relative gain against [00], and gain by the loop-method, respectively.

		T'_{RX}	T_{RX}	T_{RX} (lab)	G_a	G_r	G_l
00	X	116.1	90.1	97.4	67.11	0.00	0.00
00	Y	112.8	86.8	85.3	67.07	−0.05	−0.77
S1	X	139.5	113.5	97.4	65.61	−1.50	−1.56
S1	Y	1668.3	1642.3	118.4	52.34	−14.78	−14.58
E1	X	117.1	91.1	98.2	66.81	−0.31	−0.63
E1	Y	124.6	98.6	97.3	66.14	−0.97	−1.15
E2	X	122.8	96.8	84.8	66.68	−0.44	−1.10
E2	Y	124.5	98.5	86.7	66.14	−0.97	−1.72
E3	X	113.0	87.0	84.0	67.11	0.00	−0.33
E3	Y	118.9	92.9	99.1	66.82	−0.29	−0.83
W1	X	107.0	81.0	101.9	67.47	0.35	
W1	Y	112.2	86.2	104.5	66.92	−0.19	
W2	X	108.2	82.2	85.4	67.42	0.30	
W2	Y	119.4	93.4	101.2	66.50	−0.61	

between G_r and G_l is, thus, due to the frequency dependence of gain in the pass-band.

6.2 *Effective aperture area (Ae)*

In order to confirm the validity of synthesization of signals, we measured an effective aperture area A_e of each antenna using the sun as a reference signal source on May 22 and June 2, 2004. The sun at 327 MHz has a strong flux (about 200,000 Jy) in quiet states. The frequency spectrum consists of low frequency edge of thermal emission of 6,000 K and radiation from the solar corona (Fig. 69). The sun at 327 MHz is not always stable, but has time variations. We carried out, therefore, the simultaneous observation with IPRT (Iitate Planetary Radio Telescope) to measure the absolute flux of the sun on June 2, 2004.

The effective antenna aperture area, A_e, is derived using the relation

$$\Delta T_{star}=\frac{A_e S}{2k} \tag{102}$$

where ΔT_{star}, S, and k are the change of the antenna temperature caused by the star, source flux of the target star, and Boltzmann's constant, respectively. The conversion from measured power in dBm to temperature in Kelvin is made by taking the ratio with inputted ambient temperature. In this case, the measurement is sequentially made by switching the input signals of the front-end unit (antenna or 50 Ω), which is shown in Fig. 70. The output level (P_{obs}) at "OUT" in Fig. 70 for the 50 Ω resistor with ambient temperature is

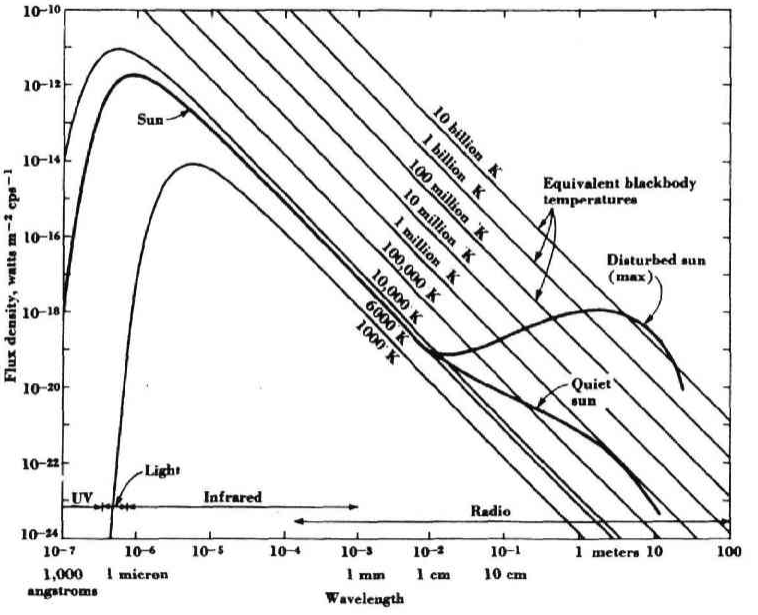

Fig. 69. Spectrum of the sun in a wide frequency range including UV, Visible light, Infra-red, and Radio. In the radio frequency, non-thermal emissions around the sun is added to the thermal emission of 6,000 K. (Kraus, 1986)

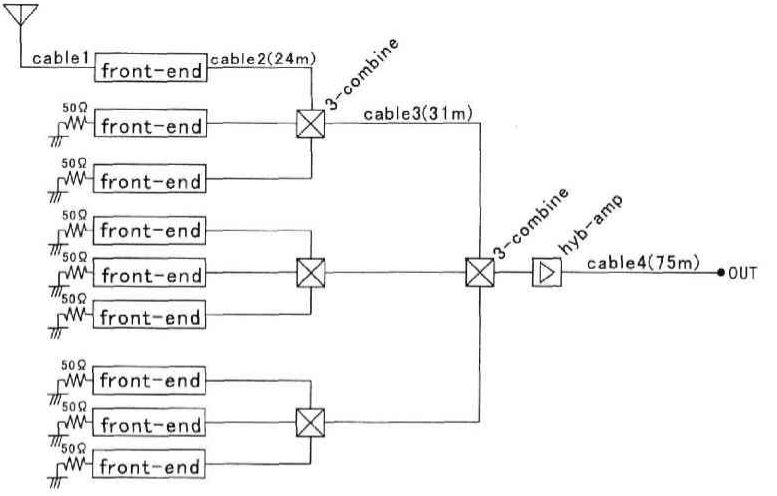

Fig. 70. Configuration of combination of signals in measuring of the aperture area of one antenna using the sun.

$$P_{amb}=\sum_{n} k\Delta f G_n(T_{amb}+T_{RXn}) \tag{103}$$

and output level (P_{star}) at "OUT" for signal input from the N^{th} antenna is

Table 13. Measured effective aperture area (A_e) of each antenna. The absolute flux value of the sun was 1.77×10^5 Jy, which was used as the reference radio source.

		T_{star} [K]		A_e [m^2]	
ant.	pol.	May 22	June 2	May 22	June 2
00	X	1531.8	1371.8	11.9	10.7
S1	X	1757.7	1764.4	13.7	13.8
E1	X	1329.1	1367.6	10.4	10.7
E2	X	1343.1	—	10.5	—
E3	X	1500.8	1370.0	11.7	10.7
W1	X	1320.6	1320.8	10.3	10.3
W2	X	1401.0	1272.5	10.9	9.9

$$P_{starN}=\sum_n k\Delta f G_n(T_{amb}+T_{RXn}) + k\Delta f G_n(-T_{amb}+\Delta T_{starN}+T_{sky}) \quad (104)$$

where G_n and T_{RXn} are the gain and receiver noise temperature of the N^{th} front-end, which are given by the Y-factor method. Taking the ratio of Equation (103) and (104), ΔT_{starN} can be derived using the ratio of P_{starN}/P_{amb}.

The measured power profile of the sun is shown in Fig. 71 (see page 87). The calculated A_e values for each antenna from this measurement are listed in Table 13. In calculation of A_e, outdoor temperature measured with the weather monitor at the Zao observatory is adopted as the ambient temperature T_{amb}. The background temperature of T_{sky} is estimated to be 51 K using the all sky map of Haslam *et al.* (1982) at the frequency of 408 MHz. The estimation of T_{sky} at 327 MHz from 408 MHz data is performed applying the power low of Equation (46). The absolute flux of the sun measured on June 2, 2004 with IPRT is 1.77×10^5 Jy. This value was adopted to the calculation on May 22, 2004, because it is confirmed that the solar radio flux is the same between May 22 and June 2 from the data published by the Space Environment Center (SEC)[1]. The measured A_e is about 1/4 of that calculated from the simulation (Fig. 39). The reasons why the measured A_e is diminished compared with the designed value are discussed in next section.

6.3 *Observations of radio stars*

The test observation was carried out to examine the synthesized characteristics of the system using radio stars listed in Table 14. Observations were continuously made for a week. The all observations were carried out by the drift scan method at the culmination of the star. In the drift scan method, the antenna is directed ahead the target star. As the star moves through the antenna beam, the output signal increases, and then decreases after the passage of the antenna-beam peak. The averaging point number of power meter is 512 points (corresponding to the integration time of 13 sec),

[1] http://www.sec.noaa.gov/ftpmenu/lists/radio.html

Table 14. List of stars used in the test observations.

	Right ascension	Declination	Flux	Elevation
3C274 (Vir-A)	$12^h28^m18^s$ (1950)	12°40.0′ (1950)	742Jy	64.3°
3C227	$09^h45^m09^s$ (1950)	07°39.3′ (1950)	~23Jy	59.3°
Jupiter	10^h46^m-48^m	09°12′-2′	~5Jy	61°

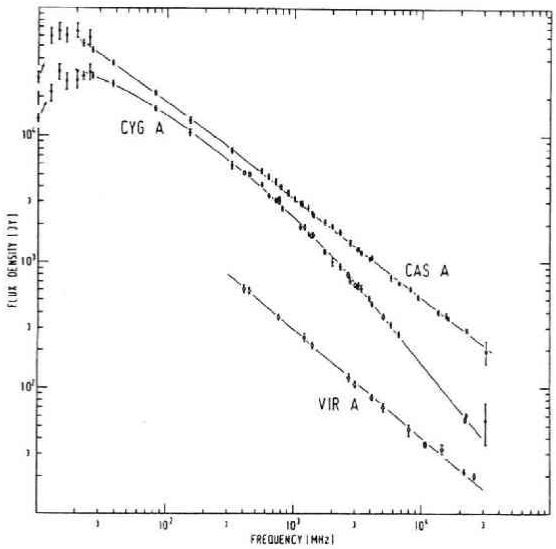

Fig. 72. Spectra of calibration stars; Cas-A, Cyg-A, and Vir-A (Baars *et al.*, 1977).

Table 15. The model parameters in Baars *et al.*, 1977 and calculated radio flux at 327 MHz.

				$\log S$ [Jy] $= a + b\log f$ [MHz] $+ c\log^2 f$ [MHz]						f [MHz]
Source	interval			a	error	b	error	c	error	327
Cas-A (1965.0)	22	300	MHz	5.625	0.021	−0.634	0.015	−0.023	0.001	7679.8
Cas-A (1965.0)	300	31,000	MHz	5.880	0.025	−0.792	0.007			7735.3
Cas-A (1980.0)	300	31,000	MHz	5.745	0.025	−0.770	0.007			6438.7
Cyg-A	20	2,000	MHz	4.695	0.018	0.085	0.003	−0.178	0.001	6070.9
Cyg-A	2,000	31,000	MHz	7.161	0.053	−1.244	0.014			10787.0
Tau-A	1,000	35,000	MHz	3.915	31.000	−0.299	0.009			1456.0
Vir-A	400	25,000	MHz	5.023	0.034	−0.856	0.010			742.2

The power meter output is sampled in digital in every 1 second. The test observations were made using 7 antennas except [W3] and [S2], in which some mechanical troubles have arisen.

The absolute flux value of Vir-A is given from the approximation proposed by data by Baars *et al.* (1977). The absolute spectra of Cas-A, Cyg-A, and Vir-A are shown in Fig. 72, and parameters for the model spectrum and calculated flux at 327 MHz are listed

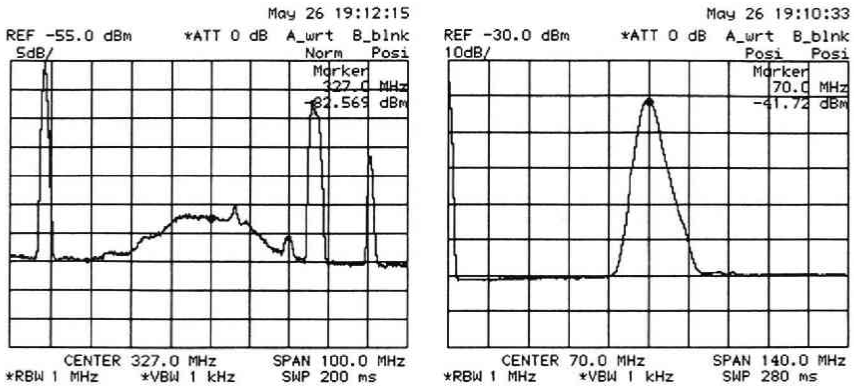

Fig. 73. Typical spectra of RF (left) and down converted IF (right) frequencies in the test observation.

in Table 15.

The X-polarization component is used for the test observation. The typical spectra of RF and down converted IF signals are shown in Fig. 73.

The observational sequence is planed to make an efficient test observation, which is almost as same as the actual observation;

1. almanac calculation of the target star position and optical path differences (delay time) among antennas
2. alignment of antenna direction to the target radio source
3. system calibration by the loop-method
4. setting the phase shifter
5. measurement of 50 Ω level
6. start of the observation

The acquired data, which is the time profile of the received power [dBm], is converted to the right ascension versus temperature [K] domain. The conversion from power to temperature is done by taking the ratio with 50 Ω input level which is measured in sequence 5, i.e,

$$\frac{P_{obn}}{P_{amb}}=\frac{\Delta T_{star}+T_{sky}+T_{RX}}{T_{amb}+T_{RX}} \tag{105}$$

In practice, however, P_{obs} becomes higher than an expected value and fluctuates due to the artificial noise outside the observation bandwidth and due to the gain differences arisen during the measurement of T_{amb} and measurement of the star. Thus, a factor α is multiplied to make T_{sys} reasonable level, i.e.,

$$\Delta T_{star}+T_{sky}+T_{RX}=\alpha\frac{P_{obn}}{P_{amb}}(T_{amb}+T_{RX}) \tag{106}$$

Accordingly, the reference level of the temperature (vertical axis) is relative, but the dispersion level is valid for the discussions to measure the ΔT_{star}.

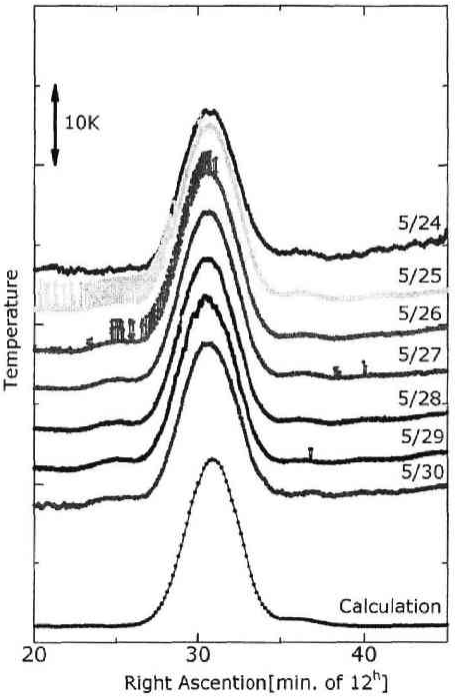

Fig. 74. Results of the test observations for Vir-A for May 24 May 30, 2004 and calculated synthesized beam (bottom). The offset level of temperature axis is relative, but the one division is 10 Kelvin.

3C274(Vir-A) observation

The result of 3C274 observations is shown in Fig. 74. The nominal flux of the star is 742 Jy. The pulse noises, for example before the culmination on May 25, whose duration is much shorter than the beam width, are artificial noises. The increasing trend of background indicates the structure of galaxy. The fluctuation of level on May 29 is caused by the wind, which swings antennas randomly.

In Fig. 74, calculated synthesized beam with 7 antennas is also shown (bottom). The observed beam profiles are quite reasonable with the calculated. Half power beam width is about 1°.

The height between the background level and the temperature peak of the star showed 19.4 K except for the data on May 24, whose deviation is larger than other days. The constant value of ΔT_{star} means the system is stable during the observation span. Set the value into ΔT_{star} in Equation (102), we obtain the effective aperture area of antenna, A_e, as 72.2 m^2. The effective aperture area per antenna is estimated to be 10 m^2(=72.2/7), which is consistent with the effective aperture area of one antenna measured using the sun. This means that signals are well synthesized in the in-phase condition.

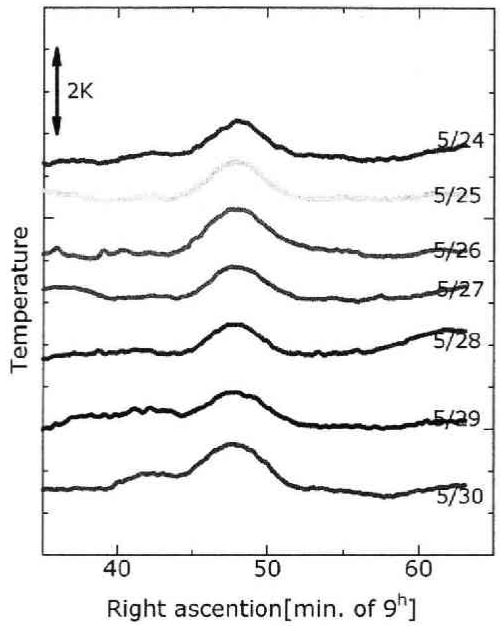

Fig. 75. Same as Fig. 74 but for 3C227.

3C227 observation

The result of 3C227 observations is shown in Fig. 75. The nominal flux of the star is about 23 Jy. As the data reduction, obvious artificial noises were removed, and gradient of background was calibrated, and running average with 10 points were made.

From the figure, the ΔT_{star} by 3C227 is about 0.5 K, which is consistent with the antenna aperture area of 72.2 m² in Equation (102). Fig. 76 (see page 87) shows a proportional relation between source flux and increase of antenna temperature calculated from Equation (102) for various antenna apertures areas. The red line is the case of A_e=72.2 m², which is derived from the Vir-A observation. Scaling of input level is confirmed because the observed value is on the line.

Jupiter observation

The result of the test observation for Jupiter on May 25 and May 29, 2004 is shown in Fig. 77, which is the first-light of Jupiter by our system.

In the same way as 3C227, the running average with 45 points are made after removal of apparent artificial noises and gradient of background is calibrated as the data reduction.

The increase of temperature for 45^m-47^m is attributed to Jupiter, whose height (ΔT_{star}) is 0.07 K obtained from the Gaussian function (black solid line) with slant background (black doted line in Fig. 77). The JSR flux derived from the ΔT_{star} is 3 Jy. The distance between the earth and Jupiter is 5.3 AU in this time, The standardized value at 4.04 AU is 5 Jy, which is consistent with typical value of previous observation.

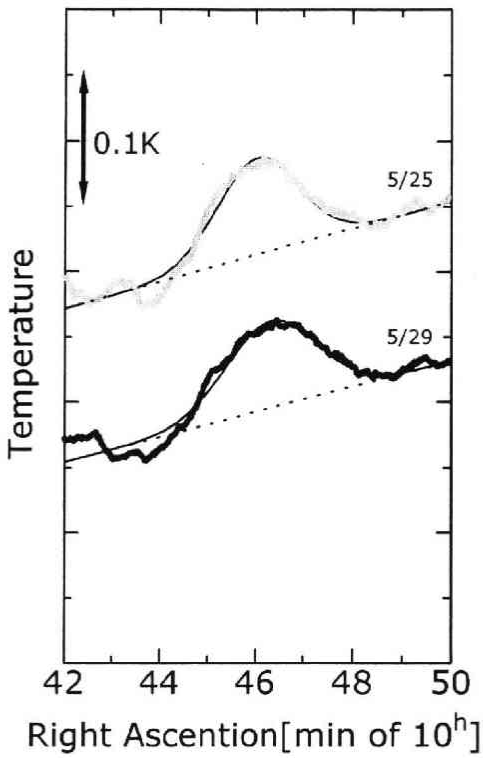

Fig. 77. The results of the test observations for Jupiter on May 25 and 29, 2004 and the fitted Gaussian functions with slant background to the observed profiles.

7 Discussions

7.1 Effective antenna aperture area

The effective aperture of the developed antenna was measured to be 11.2 m^2 in average (Table 13), which is 28%(−5.53 dB) of the expected value (39.4 m^2) from the calculation. Three possible causes are discussed.

7.1.1 Impedance mismatch between antenna and feeding cable

Impedance mismatch of the antenna with feeding cable can become an origin of smaller aperture area than expected one because a part of the radio wave fed to the cable at the pick-up point is re-radiated to the source when the output impedance of antenna is not equal to the input impedance of the feeding cable. Mismatch of impedance can be measured using the antenna as a radiator. The VSWR (Voltage Standing Wave Ratio) value of the antenna including the $1/4\lambda$ cable is measured using network analyzer (8712 B, Hewlett Packard) as a function of frequency as shown in Fig. 78. VSWR is defined as a ratio of maximum and minimum voltages of standing wave, and has a relation with the voltage reflection ratio Γ as

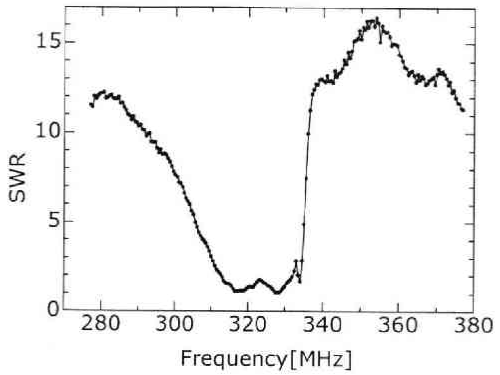

Fig. 78. Measured VSWR (Voltage Standing Wave Ratio) value of one stacked antenna including the $1/4\lambda$ impedance conversion line as a function of frequency. The VSWR value at 327 MHz is 1.21.

$$\Gamma=\sqrt{\frac{P_r}{P_f}} \tag{107}$$

$$=\frac{VSWR-1}{VSWR+1} \tag{108}$$

where P_f and P_r are forward and reflected powers, respectively. Γ has a relation with the radiation efficiency ε as

$$\varepsilon=\frac{P_f-P_r}{P_f} \tag{109}$$

$$=1-1^2 \tag{110}$$

From Fig. 78, the VSWR value is obtained to be 1.21 at 327 MHz, which means that the radiation efficiency ε is 0.99097 (-0.039 dB). These obtained values from the VSWR measurement indicate that the impedance match between antenna and feeding cable is fairly good and is not the cause of the unexpectedly small antenna aperture.

7.1.2 Ohmic loss in cables and combiners

The loss of feeding system (cable and combiner) is not included in the calculation of antenna gain (Fig. 39). Thus, this kind of loss has a possibility to become a origin of the small aperture area. The level diagram from the pick-up to the last combiner is shown in Table 16. The combiner losses in the table do not include the coupling losses of -3.01 dB($=1/2$) and -6.02 dB($=1/4$). The losses of cables (10D-SFA) are interpolated by a typical value provided from the manufacturer (shown in Fig. 79 (see page 88) and Table 17). The sum of the individual loss becomes 1.2 dB. However, the measured total loss was 1.7 dB. The difference may be caused by the loss of connecters which is not counted in Table 16. The loss of 1.7 dB reduces the antenna gain -1.7 dB, which corresponds to the antenna efficiency of 68%.

Table 16. Level diagram of the stacked antenna from the pick-up to output of 2-port combiner.

	estimation
10D-SFA (5 m)	0.26
4-port combiner	0.80
10D-SFA (2.5 m)	0.13
2-port combiner	0.01
sum	1.20

Table 17. Parameters for the loss estimation of coaxial cables. The unit of frequency x is [MHz].

	parameter in $y=ax^b$		
	a	b	y at 327 MHz [dB/10 m]
3D-2V	0.130	0.520	2.63
5D-2V	0.064	0.566	1.69
8D-2V	0.040	0.589	1.20
10D-2V	0.028	0.608	0.94
3.5-DS	0.082	0.523	1.70
5D-FB	0.053	0.532	1.16
8D-FB	0.033	0.544	0.78
10D-FB	0.024	0.562	0.63
11D-4AF	0.020	0.562	0.52
15D-4AF	0.015	0.575	0.41
23D-4A	0.008	0.627	0.29
5D-SFA	0.052	0.498	0.93
8D-SFA	0.029	0.536	0.64
10D-SFA	0.025	0.528	0.52
12D-SFA	0.019	0.542	0.43

7.1.3 Effect of phase irregularity

The phase irregularity between 8 pick-up elements also becomes an origin of small aperture. The cable length between pick-up elements and the frontend unit is adjusted to be same length each other. Therefore, the phase irregularity, if any, can be generated due to the irregular alignment of the 4×2 stacked antenna. In the following, the effect of phase error caused by the roughness of pick-up plain is estimated by applying the examination for the surface irregularities of a parabolic antenna.

For a parabolic surface with irregularity of δ' (Fig. 80), the gain factor K_g can be represented as (Kraus, 1986),

$$K_g=\left[\frac{E_0\cos\Delta\phi}{E_0}\right]^2 \tag{111}$$

$$=\cos^2\Delta\phi \tag{112}$$

where $\Delta\phi$ is the phase difference,

$$\Delta\phi=720^\circ\frac{\delta'}{\lambda} \tag{113}$$

The 720° means the phase rotation during the back-and-forth of radio waves at the parabolic surface. To apply this to a stacked antenna, Equation (113) is rewritten as

$$\Delta\phi=360^\circ\frac{\delta'}{\lambda} \tag{114}$$

Fig. 81 represents the estimated K_g(in dB) values for and $\Delta\phi$ and δ'. Here, we considered that the small antenna aperture (−5.53 dB) is originated from impedance mismatch, ohmic loss in the feeding path, and the phase irregularity due to the roughness of the alignment. The impedance mismatch is estimated to be almost negligible (section 7.1.1). The ohmic loss in the feeding pass is measured to be −1.7 dB. If the remnant of loss (−3.83 dB) is attributed to the phase irregularity due to the roughness of the

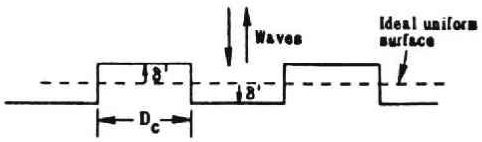

Fig. 80. Schematic view of surface fluctuation with irregularity of δ' for a reflector antenna (Kraus, 1986).

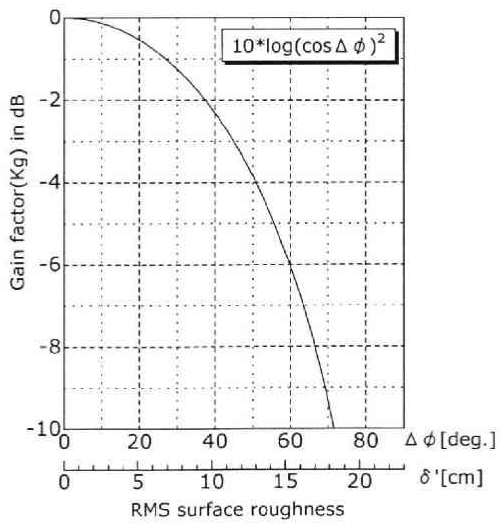

Fig. 81. Relation between loss of signals due to the surface roughness and $\Delta\phi$. δ' is surface roughness with the dimension of length for the radio wave of 327 MHz.

antenna alignment. From Fig. 81, −3.83 dB corresponds to the phase deviation of ~50° in RMS, which is equivalent to the alignment deviation of ~13 cm, as can be seen in Fig. 81.

7.2 Phase difference in the bandwidth

Radio waves with finite bandwidth have a phase difference in the band because the delay length (optical path difference) has a frequency dependence, which results the loss of coherency. The phase differences ϕ and delay length d have a relation

$$\phi(f)=\frac{d}{\lambda}2\pi \tag{115}$$

$$=\frac{f}{c}2\pi d \tag{116}$$

where λ, f, and c are the wavelength, frequency of the radio wave, and speed of light, respectively. The phase differences for the frequency of $f+\Delta f/2$ are given by,

$$\phi(f+\Delta f/2)=\frac{f+\Delta f/2}{c}2\pi d \tag{117}$$

$$=\phi(f)+\phi(\Delta f/2) \tag{118}$$

Here, the phase difference at the edge of bandwidth ($\phi(f+\Delta f/2)$) against the center frequency is set to be π, then,

$$d=\frac{c}{\Delta f} \tag{119}$$

$$=\Delta\lambda \tag{120}$$

where $\Delta\lambda$ is wavelength of radio wave with frequency Δf. Equation (120) describes the relation between the bandwidth and baseline length, which is called coherency length. For example, when the bandwidth is set to 10 MHz, the delay length becomes 30 m.

In the following, the loss of signal in the process of synthesizing is discussed quantitatively.

Coherency length has a dependence on the elevation angle, because the delay length is a projection of baseline length onto the wave normal of an incident wave. Normalized array factor as a function of elevation angle for various Δf is shown in Fig. 82. The array factor is calculated as same as the calculation of synthesized beam, while frequencies are taken to be f_0+1, f_0+2, f_0+3, f_0+4, f_0+5 MHz. The array factor becomes smaller as the elevation angle decreases, because the delay length becomes longer. The cross section along the frequency at elevation angle of 64° (corresponding to elevation angle of Vir-A at the culmination) is shown by curve (a) of Fig. 83. The Gaussian function with the half power width of 10 MHz is curve (b) in Fig. 83. The product of (a) and (b) is curve (c) in Fig. 83 which represents the realistic pass-band. The ratio between integration of (b) and (c) over frequency represents the loss by coherence, i.e., when coherency (a) and beam profile (b) are set to C(f) and B(f), respectively, the band weighted coherency is represented as

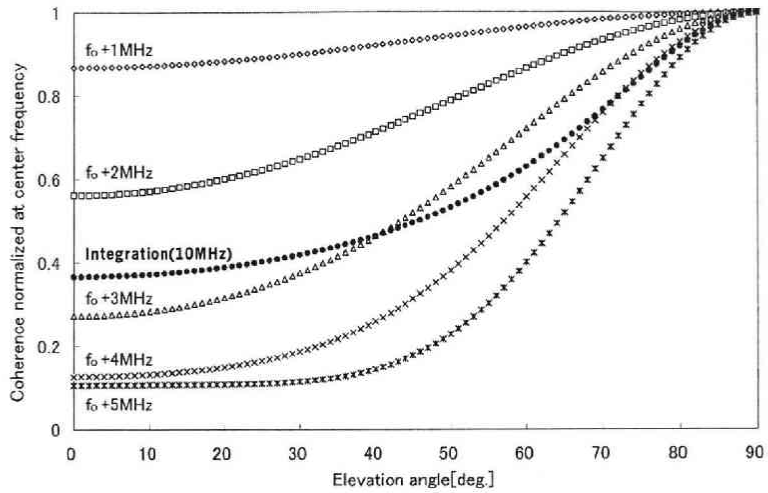

Fig. 82. Coherence of a signal as a function of elevation angle for five frequencies against the center frequency, and integrated coherence over the full pass-band (10 MHz).

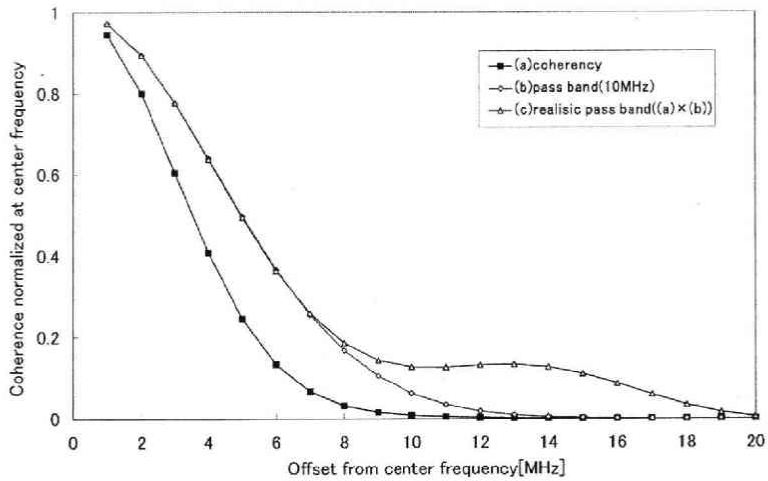

Fig. 83. Coherence of a signal as a function of offset from center frequency for elevation angle of 64° (a), the shape of passband for coherent signal (b), and product of (a) and (b) which represents the realistic pass-band (c).

$$\frac{\int_{band} B(f) \cdot C(f) df}{\int_{band} B(f) df} \tag{121}$$

which is shown as filled dots in Fig. 82.

The coherency loss ratios at elevation angle of 64° for bandwidth of 2, 5, 10 MHz are

Table 18. The relation between bandwidth and aperture efficiency for 9 antennas (full) and 7 antennas (in case of the test observation).

	2 MHz	5 MHz	10 MHz
9 antennas (full)	96%	87%	68%
7 antennas (except [W3], [S2])	98%	93%	80%

listed in Table 18 for the case of both 9 antennas and 7 antennas. From Table 18, it is thought that the bandwidth of 10 MHz is too wide for the Zao antenna particularly in the case of 9 antennas.

If we improve the loss originated from the phase difference in the bandwidth as the next step of this system, it is better to adopt electric delay lines for the cancellation of delay lengths instead of the simple phase shifters installed in the present system.

7.3 Effects of solar radio emission

Because the flux of the sun is about 200,000 Jy in quiet state (Fig. 69), which is about 40,000 times (46dB) as large as the JSR flux. It is thought that there might be contamination to the JSR observation from the sun even if the antenna is not directed to the sun. This is so called "stray light" of optical instruments.

The synthesized antenna beam pattern for the elevation of 60° is shown in Fig. 84. For the direction of not only near the main lobe (±30°) but also near back direction, the minor lobes are greater than −46 dB. Thus, attention for the solar radio emission is, therefore, required on the observation in daytime.

Moreover, the flux of solar radio bursts exceeds about 1,000 times (30 dB) compared with the quiet state (Fig. 69). The most common solar burst at 327 MHz is a fixed frequency radio burst without any frequency drift as Type II and Type IV bursts, and continues for some minutes.

The example of the detection of solar radio burst on June 14, 2003 is shown in Fig. 85. The method of the observation is the drift scan for the culmination of the sun at 11 :

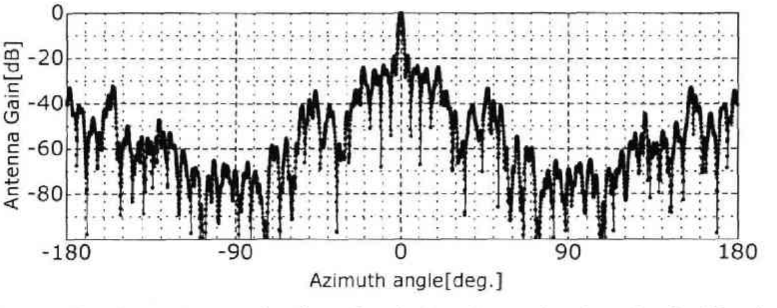

Fig. 84. Synthesized beam for the azimuth direction at 60° elevation in dB unit.

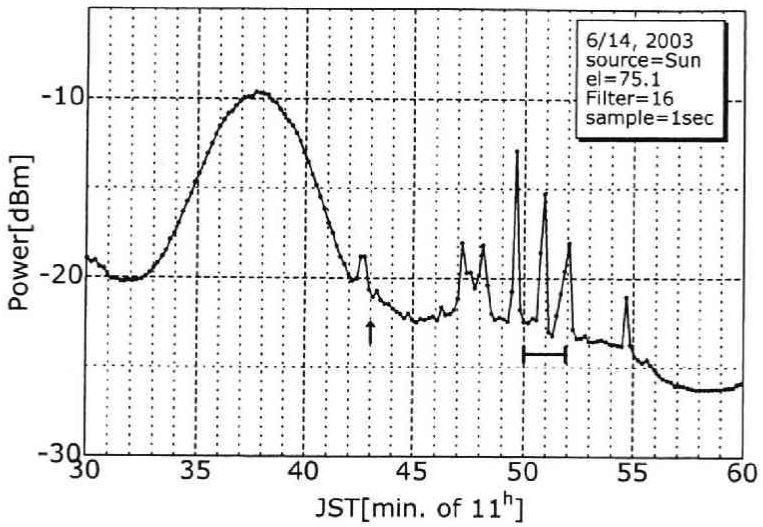

Fig. 85. Example of solar radio bursts on June 14, 2003. The method of the observation is the drift scan for the culmination of the sun at 11 : 38, when the main beam passed the sun.

38, when the main beam passed the sun. From the lists provided by the Space Environment Center (SEC)[2], it was confirmed that there were some radio bursts at 02 : 43 UT with 210 SFU[3] and 02 : 50-02 : 53 UT with 130 SFU, which were recorded at Learmonth (Australia). The radio bursts were also detected with HiRAS[4] (National Institute of Information and Communications Technology (NICT)), which is shown in Fig. 86.

The solar radio burst is strong, but the duration time is short. The solar radio bursts are, therefore, distinguishable from the JSR emission.

7.4 Monitor of loop-method calibration

In order to confirm the stability of the system, the monitoring of relative gain and phase by loop-method was performed, which is shown in Fig. 87 (see page 89). The monitor was continued during a week with a 10 minutes interval.

Obvious changes of gain and phase are seen in the time zone of dawn and dusk, where the gradient of temperature is particularly large in a day. In the worst case at dawn or dusk, the rate of the phase change is about 10°/30 min, which is negligible because a typical span of one drift scan is 30 min and can be corrected by the calibration at the start of observation.

7.5 Vision for an interferometric observation

In this section, we think possibility of an interferometric observation using the Zao

[2] http://www.sec.noaa.gov/ftpmenu/lists/radio.html
[3] 1SFU (Solar Flux Unit)=10,000 Jy
[4] http://sunbase.nict.go.jp/solar/denpa/index.html

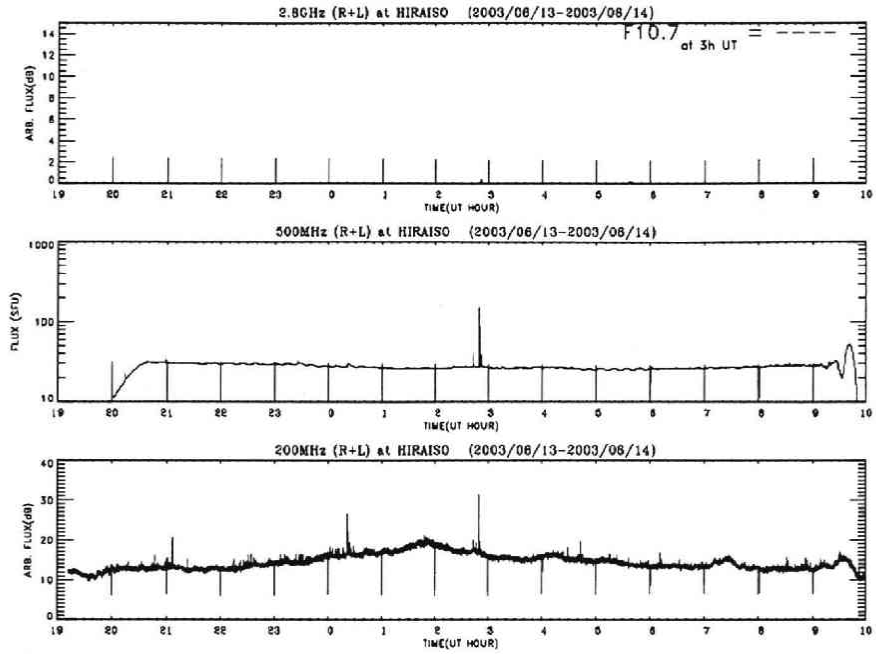

Fig. 86. HiRAS observation on June 14, 2003. Bursts are clearly seen around 02 : 50 UT.

system as one station. The developed antenna system in this study has a capability to be utilized for the interferometic observation to perform the two or three dimensional imaging observation of the Jovian radiation belt.

Fig. 88 shows a spatial resolution of the interferometer as a function of antenna separation normalized by the wavelength. The point marked ZAO in the figure indicates the case when the developed Zao-system is regarded as the interferometric system.

As the first step for an imaging observation, the east-west baseline with 5-10 km is proper, which can resolve equational structure of JSR like (d) in Fig. 16. Equational structure provides information on the shoulder structure concerning to the pitch angle scattering by Amalthea (de Pater *et al.*, 1997) and the peak position concerning to the radial diffusion parameter and electron spectra (de Pater and Goertz, 1990).

In the case of a longer baseline interferometer, such as 'Zao-Iitate' interferometer (50 km baseline), it might be too long because the characteristic scale of the JSR source region is smaller than the spatial resolution of the interferometer.

For the interferometer with the baseline of several km, it will be possible to connect each station by some wire. Recently real-time interferometric technique has been developed using fast internet connection with an optical fiber. In this technique, a fast A/D sampler is adopted in both stations, and the data are sent to one station with almost no delay. The correlation analyses are made also in real-time using the data to derive source structures of an object radio wave. The real-time interferometric technique has

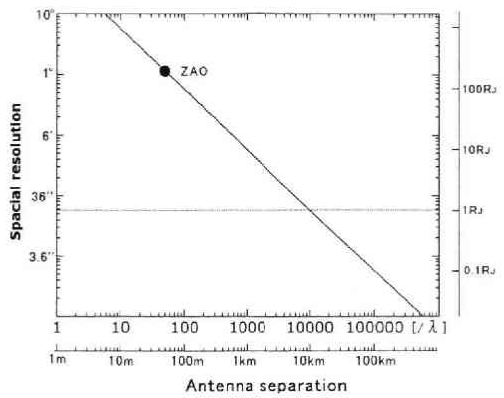

Fig. 88. The relation between antenna separation normalized by wavelength and spatial resolution. The scales of antenna separation and spatial resolution are also plotted for 327 MHz wave and radius of Jupiter around opposition (1 R_J=20 arcsec), respectively.

been mainly developed by NICT and enables us to make such processes with conventional personal computers. This recent progress of technology and the techniques of an aperture synthesis array antenna developed in this study will realize an imaging observation of JSR in no distant future.

8 Conclusion

The short-term variation of Jovian synchrotron radiation (JSR) has information of dynamical acceleration, transport, and loss processes of relativistic electrons in the Jovian radiation belt. We have developed the observation system to attain the information with continuous grand-based observation of JSR, which can not be obtained by in-situ observation because of the radiation damage of spacecraft. The concept of the development is to achieve the optimized and exclusive system for the JSR observation.

Using the developed observation system, the signal from Jupiter was successfully detected with the flux of 5 Jy, which is consistent with previous observations.

The system is designed to detect the Jovian synchrotron radiation with sufficient sensitivity. The developed system consists of following 5 units ;

1. 9 antennas arranged in the Y formation, each of which consists of 4×2 stacked 27-element cross Yagi antenna.
2. Front-end unit with low receiver noise-temperature of about 90 K which is achieved by using a low noise device of GaAs FET. The front-end unit has the relay unit for gain and phase calibrations, the programable attenuator unit with 4 bit, and the programable phase shifter unit with 6 bit.
3. Back-end whose function is to down-convert the RF signal to IF signal, and to process the detected data.
4. Loop-method calibration system, which calibrates relative phase and gain of

signal synthesizing system.

5. Units of antenna control, communication, and personal computer system. The first unit controls antenna direction, relay unit, programable attenuator, and programable phase shifter in the front-end unit. The second unit controls communication between antenna tower and back-end house. The last unit controls measurement instruments in the back-end house by the software.

To synthesize the signals from the 9 antennas in-phase, following parameters are accurately measured;

1. Axis calibration parameters of antenna direction for both azimuth and elevation directions
2. Relative antenna position to obtain optical delay length
3. Eigen phase which is constant phase offset of each antenna originated from roughness of antenna alignment

From the performance test of each antenna and front-end unit, it was confirmed that the system noise temperature is consistent with the value that was measured in laboratory, and that signals from 9 antennas are successfully synthesized. However the effective aperture area of one antenna is smaller than the designed one; i.e., the measured effective aperture area is 28% (−5.53 dB) of the designed one. From quantitative evaluation of Voltage Standing Wave Ratio for antenna elements and feeding system, ohmic loss of feeding system, and phase irregularity among antenna elements, it was suggested that the roughness of alignment with 13 cm (corresponding to the phase irregularity of 50°) can be the principal origin of the smaller aperture area.

It was also discussed that the phase difference in observational band is not negligible, which causes the smaller synthesized aperture area with the efficiency of 68% at the bandwidth of 10 MHz. It was also confirmed that the contamination effect by the solar radio wave to the JSR observation should be noticed in the day time observation.

The development of observation system in this study also has an importance for application to the future interferometric observation. As the first step of an interferometric observation, an interferometer system with the base line of 5∼10 km using the real-time interferometric technique is proposed as an exclusive system with sufficient spatial resolution for JSR. The developed system and techniques in this study will make a great contribution in such a compact, but fully functional interferometric observation near future.

Acknowledgements

The present study has been achieved in Ph.D. course of Geophysical institute, Tohoku University. We would like to thank the members of Planetary Plasma and Atmospheric Research Center (PPARC) and space physics group (C-group) of Tohoku University, farther Dr. Tetsuro Kondo (NICT) for his technical advice of radio astronomy.

The developed system refers to the IPS systems of Solar-Terrestrial Environment

Laboratory, Nagoya University and made by the factory in graduate school of science, Tohoku University. We would like to thank for their cooperation.

References

Akabane, K., N. Kaifu, H. Tahara, Space Radio Astronomy (in Japanese), Kyoritsu Shuppan, Tokyo, 1988.

Baker, D.N., J. Blake, L.B. Callis, J.R. Cummings, D. Hovestadt, S. Kanekal, B. Klecker, R.A. Mewaldt, and R.D. Zwwicki, Relativistic electron acceleration and decay time scales in the inner and outer radiation belts: SAMPEX, *Geophys. Res. Lett.*, **21**, 409-412, 1994.

Baker, D.N., J.A. van Allen, Energetic electrons in the Jovian magnetosphere, *J. Geophys. Res.*, **81**, 617-632, 1974.

Berge, G.L., An Interferometric Study of Jupiter's Decimeter Radio Emission, *Astrophys. J.*, **146**, 767-797, 1966.

Birmingham, T., W. Hess, T. Northrop, R. Baxter, M. Lojko, The electron diffudion coefficient in Jupiter's magnetosphere, *J. Geophys. Res.*, **79**, 87-97, 1974.

Bolton, S.J., M. Janssen, R. Thorne, S. Levin, M. Klein, S. Gulkis, T. Bastian, R. Sault, C. Elachi, M. Hofstadter, A. Bunker, G. Dulk, E. Gudim, G. Hamilton, W.T.K. Johnson, Y. Leblanc, O. Liepack, R. McLeod, J. Roller, L. Roth, and R. West, Ultra-relativistic electrons in Jupiter's radiation belt, *Nature*, **415**, 987-991, 2002.

Bolton, S.J., S. Gulkis, M.J. Klein, I. de Pater, T.J. Thompson, Correlation studies between solar wind parameters and the decimetric radio emission from Jupiter, *J. Geophys. Res.*, **94**, 121-128, 1989.

Bolton, Scott J., Steven M. Levin, Samuel L. Gulkis, Michael J. Klein, Robert J. Sault, Bidushi Bhattacharya, Richard M. Thorne, George A. Dulk, and Yolande Leblanc, Divine-Garrett model and Jovian synchrotron emission, *Geophys. Res. Lett.*, **28**, 907-910, 2001.

Bolton, S.J., R.S. Foster, and W.B. Waltman, Observations of Jupiter's synchrotron radiation at 18 cm during the comet Shoemaker-Levy 9 impacts, *Geophys. Res. Lett.*, **22**, 1801-1816, 1995.

Bolton, S.J., and R.M. Thorne, Assessment of mechanisms for Jovian synchrotron variability associated with comet SL-9, *Geophys. Res. Lett.*, **22**, 1813-1816, 1995.

Brecht, S.H., M.E. Pesses, I. de Pater, N.T. Gladd, and J.G. Lyon, The role of shock acceleration on synchrotron radiation following the SL9 impact., *Geophys. Res. Lett.*, **22**, 1809-1812, 1995.

Brecht, Stephen H., I. de Pater, David J. Larson, and Mark E. Pesses, Modification of the Jovian Radiation Belts by Shoemaker-Levy 9: An Explanation of the Data, *Icarus*, **151**, 25-38, 2001.

Brice, N., and T.R. McDonough, Jupiter's radiation belt, *Icarus*, **18**, 206-219, 1973.

Burke, Bernard F., Francis Graham-Smith, An introductuin to radio astronomy (2nd edition), Cambridge University Press, 2002.

Carr, T.D., M.D. Desch, and J.K. Alexander, Phenomenology of magnetospheric radio emissions, in *Physics of the Jovian magnetosphere*, edited by A.J. Dessler, 226-284, 1983.

Connerney, J.E.P., M.H. Acuna, N.F. Ness, T. Satoh, New models of Jupiter's magnetic field constrained by the Io flux tube footprint, *J. Geophys. Res.*, **130**, 11929-11940, 1998.

de Pater, I., and C.K. Goertz, Radial diffusion models of energetic electrons and Jupiter's synchrotron radiation 1. Steady state solution, *J. Geophys. Res.*, **95**, 39-50, 1990.

de Pater, I., and C.K. Goertz, Radial diffusion models of energetic electrons and Jupiter's synchrotron radiation 2. Time variability, *J. Geophys. Res.*, **99**, 2271-2287, 1994.

de Pater, I., 21 cm maps of Jupiter's radiation belts from all rotational aspects, *Astron. Astrophys.*, **88**, 175-183, 1980.

de Pater, I., Radio maps of Jupiter's radiation belts and planetary disk at lambda 6 cm, *Astron. Astrophys.*, **93**, 370-381, 1981.

de Pater, I., Radio images of Jupiter's synchrotron radiation at 6, 20, and 90 cm, *Astron. J.*, **102**, 795-805, 1991.

de Pater, I., B.J. Butler, D.A. Green, R. Strom, R. Millan, M.J. Klein, M.K. Bird, O. Funke, J. Neidhofer, R. Maddalena, R.J. Sault, M. Kesteven, D.P. Smits, and R. Hunstead, Jupiter's radio spectrum from 74 MHz up to 8 GHz, *Icarus*, **163**, 434-448, 2003.

de Pater, I., Michael Schulz, Stephen H. Brecht, Synchrotron evidence for Amalthea's influence on Jupiter's electron radiation belt, *J. Geophys. Res.*, **102**, 22043-22064, 1997.

de Pater, I., Stephen H. Brecht, SL9 Impacts: VLA High-Resolution Observations at $\lambda = 20$ cm, *Icarus*, **151**, 1-24, 2001a.

de Pater, I., Stephen H. Brecht, SL 9 Impacts and Simulations of Enhanced Radial Diffusion, *Icarus*, **151**, 39-50, 2001b.

de Pater, I., and 26 authors, Outburst of Jupiter's synchrotron radiation after the impact of comet Shoemaker-Levy 9, *SCIENCE*, **268**, 1879-1883, 1995.

Divine, N., and H.B. Garrett, Charged particle distributions in Jupiter's magnetosphere, *J. Geophys. Res.*, **88**, 6889-6903, 1983.

Dulk, G.A., Y. Leblanc, R.J. Sault, and S.J. Bolton, Jupiter's magnetic field as revealed by the synchrotron radiation belts II. Change of the 2-D brightness distribution with D_E, *Astron. Astrophys.*, **347**, 1039-1045, 1999b.

Dulk, G.A., Y. Leblanc, R.J. Sault, S.J. Bolton, J.H. Waite, and J.E.P. Connerney, Jupiter's magnetic field as revealed by the synchrotron radiation belts I. Comparison of a 3-D reconstruction with models of the field, *Astron. Astrophys.*, **347**, 1029-1038, 1999a.

Dulk, G.A., Y. Leblanc, R.J. Sault, H.P. Ladreiter, and J.E.P. Connerney, The radiation belts of Jupiter at 13 and 22 cm II. The asymmetries and the magnetic field, *Astron. Astrophys.*, **319**, 282-289, 1997.

Feynman, R.P., R.B. Leighton, M.L. Sands, The Feynman lectures on physics (vol. 2: Mainly electromagnetism and matter), Reading, Mass., Addison-Wesley Pub. Co, 1965.

Field, G.B., The source of radiation from Jupiter at decimeter wavelengths, *J. Geophys. Res.*, **64**, 1169-1177, 1959.

Fischer, H.M., E. Pehlke, G. Wibberbez, L.J. Lanzerotti, J.D. Mihalov, High-energy charged particles in the innermost jovian magnetosphere, *SCIENCE*, **272**, 856-858, 1996.

Gerard, E., Long-term variations of the decimeter radiation of Jupiter, *Radio Science*, **5**, 513-516, 1970.

Gerard, E., Variation of the radio emission of Jupiter at 21.3 cm and 6.2 cm wavelength, *Astron. Astrophys.*, **50**, 353-360, 1976.

Gerard, E., Observation of Jupiter at 11.13 cm, *Astron. Astrophys.*, **8**, 181-188, 1970.

Gulkis, S., Lunar ocultation observations of Jupiter at 74 cm and 128 cm, *Radio Sci.*, **5**, 505-511, 1970.

Haslam, C.G.T., H. Stoffel, C.J. Salter, W.E. Wilson, A 408 MHz all-sky continuum survey. II. The atlas of contour maps, *Astron. Astrophys. Suppl. ser.*, **47**, 1-143, 1982.

Jansky, K.G., Radio waves from outside the solar system, *Nature*, **132**, 66-66, 1933.

Kaiser, M.L., Time-variable magnetospheric radio emissions from Jupiter, *J. Geophys. Res.*, **98**, 18757-18765, 1993.

Klein, M.J., The variability of the total flux density and polarization of Jupiter's decimetric radio emission, *J. Geophys. Res.*, **81**, 3380-3382, 1976.

Klein, M.J., S. Gulkis, and C.T. Stelzried, Jupiter: New evidence of long-term variations of its decimeter flux density, *Astron. J.*, **176**, L85-L88, 1972.

Kraus, J.D., Radio Astronomy (2nd edition), Cygnus-Quasar Books, Ohio, 1986.

Leblanc, Y., G.A. Dulk, R.J. Sault, and R.W. Hunstead, The radiation belts of Jupiter at 13 and 22 cm I. Observations and 3-D reconstruction, *Astron. Astrophys.*, **319**, 274-281, 1997.

Levin, S.M., S.J. Bolton, Samuel L. Gulkis, Michael J. Klein, Bidushi Bhattacharya, Richard M. Thorne, Modeling Jupiter's synchrotron radiation, *Geophys. Res. Lett.*, **28**, 903-906, 2001.

Mauk, B.H., D.J. Williams, R.W. McEntire, Energy-time dispersed charged particle signatures of dynamic injections in Jupiter's inner magnetosphere, *Geophys. Res. Lett.*, **24**, 2949-2952, 1997.

Mauk, B.H., D.J. Williams, R.W. McEntire, K.K. Khurana, J.G. Roederer, Storm-like dynamics of Jupiter's inner and middle magnetosphere, *Geophys. Res. Lett.*, **104**, 22759-22778, 1999.

Miyoshi, Y., H. Misawa, A. Morioka, T. Kondo, Y. Koyama, J. Nakajima, Observation of short-term variation of Jupiter's synchrotron radiation, *Geophys. Res. Lett.*, **26**, 913, 1999.

Morris, D., and G.L. Berge, Measurements of the polarization and angular extent of the decimetric radiation of Jupiter, *Astrophys. J.*, **136**, 276-282, 1962.

Radhakrishnan, V., and J.A. Roberts, Polarization and Angular Extent of the 960-Mc/sec Radiation from Jupiter, *Phys. Rev. Letters*, **4**, 493-494, 1960.

Reich, P., W. Reich, Spectral index variations of the Galactic radio continuum emission—Evidence

for a Galactic wind, *Astron. Astrophys.*, **196**, 211226, 1988.
Sault, R.J., T. Oosterloo, G.A. Dulk, and Y. Leblanc, The first three dimensional reconstruction of a celestial object at radio wavelengths: Jupiter's radiation belts, *Astron. Astrophys.*, **324**, 1190-1196, 1997.
Sault, R.J., Y. Leblanc, and G.A. Dulk, Localized brightenings in Jupiter's radiation belts resulting from Comet SL 9 impacts, *Geophys. Res. Lett.*, **24**, 2395-2398, 1997.
Sloanaker, M. Russell, Apparent temperature of Jupiter at a wave length of 10 cm, *Astron. J.*, **64**, 346-346, 1959.
Van Allen, J.A., High-energy particles in the Jovian magnetosphere, in *JUPITER*, edited by T. Gehrels, Univ. of Arizona press, 929-960, 1976.
Wineland, D.J., N.F. Ramsey, Atomic Deuterium Maser, *Physical Review A*, **5**, 821-837, 1972.

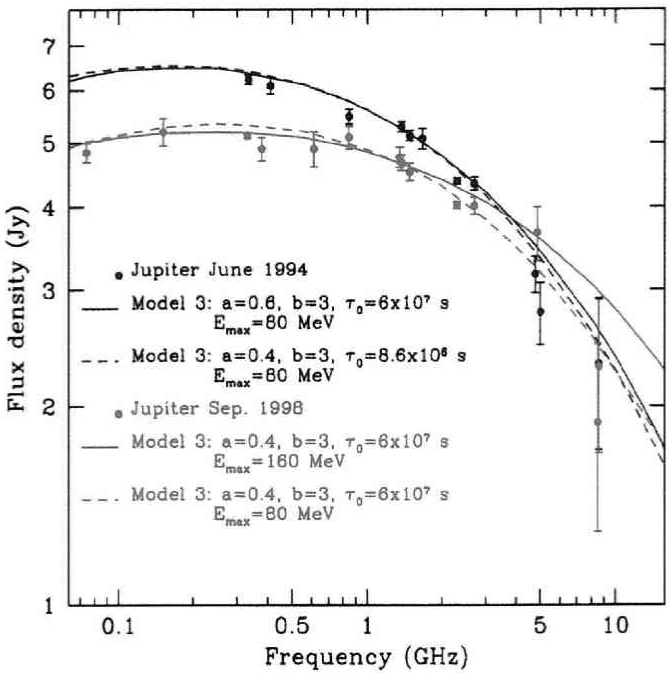

Fig. 8. JSR spectrum from 74 MHz to 8 GHz by observations (filled circles) in June 1994 (just before the SL9 impacts, blue) and September 1998 (red). The broken and solid lines are the bestfit models to the observations. (de Pater *et al.*, 2003).

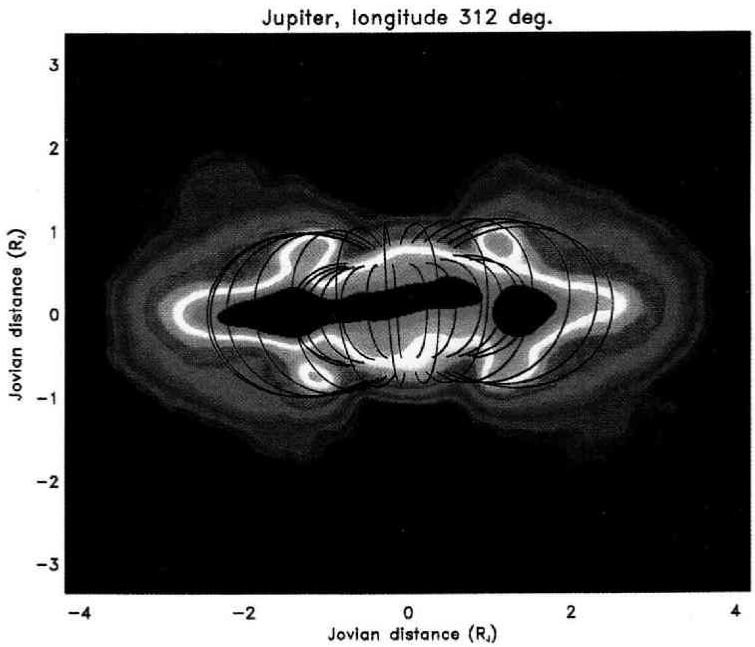

Fig. 15. High-resolved structure of JSR using VLA at 2.2 GHz. Calculated magnetic field lines at L=1.5 and 2.5 are superposed as black solid lines (de Pater *et al.*, 1997).

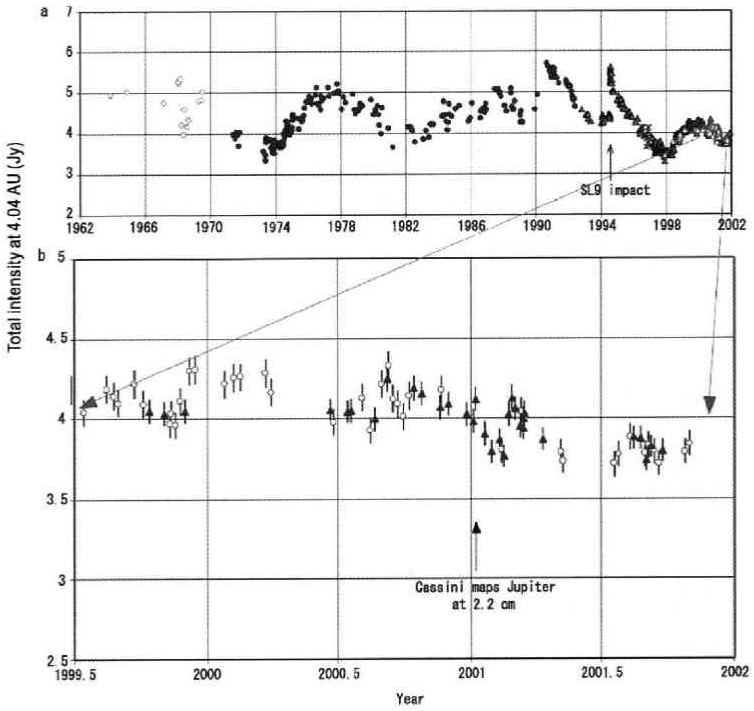

Fig. 17. Summary of the 'Jupiter patrol' observation of JSR in long-term (a) and short-term (b). Long-term has a clear periodicity of 11 years expect for the SL9 impact in July 1994. Moreover, time variations exist in short-term (Bolton *et al.*, 2002).

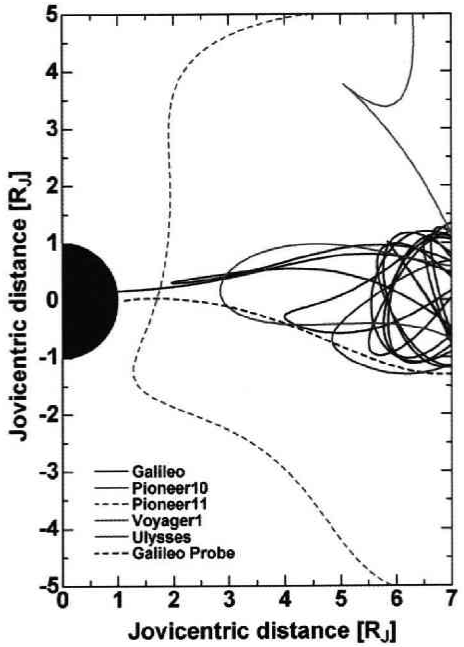

Fig. 24. The orbit paths of 7 spacecrafts visiting Jupiter projected onto the magnetic meridian plain.

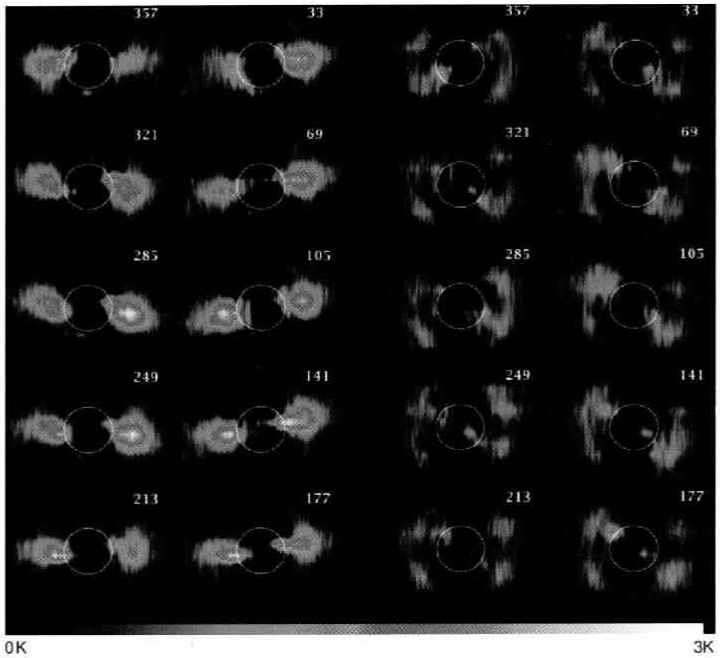

Fig. 28. Jovian synchrotron radiation observed by the Cassini spacecraft at 13.8 GHz. The maps in the left side are horizontal polarization and those in the right side are vertical polarization. The number of each map represents the CML value. The thermal components are subtracted using the Jovian atmospheric model considering radiative transfer process (Bolton *et al.*, 2002).

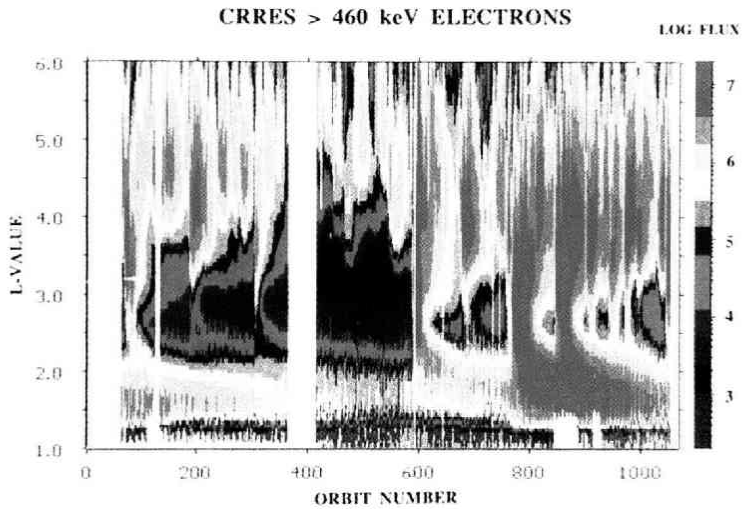

Fig. 29. The dynamical feature of radiation belts of the Earth observed by the CRRES spacecraft for E>460 keV electrons. The horizontal axis is orbit number (about 13 months span), the vertical axis is L-value, and flux is displayed by color scale, which is called L-t diagram (Baker *et al.*, 1994).

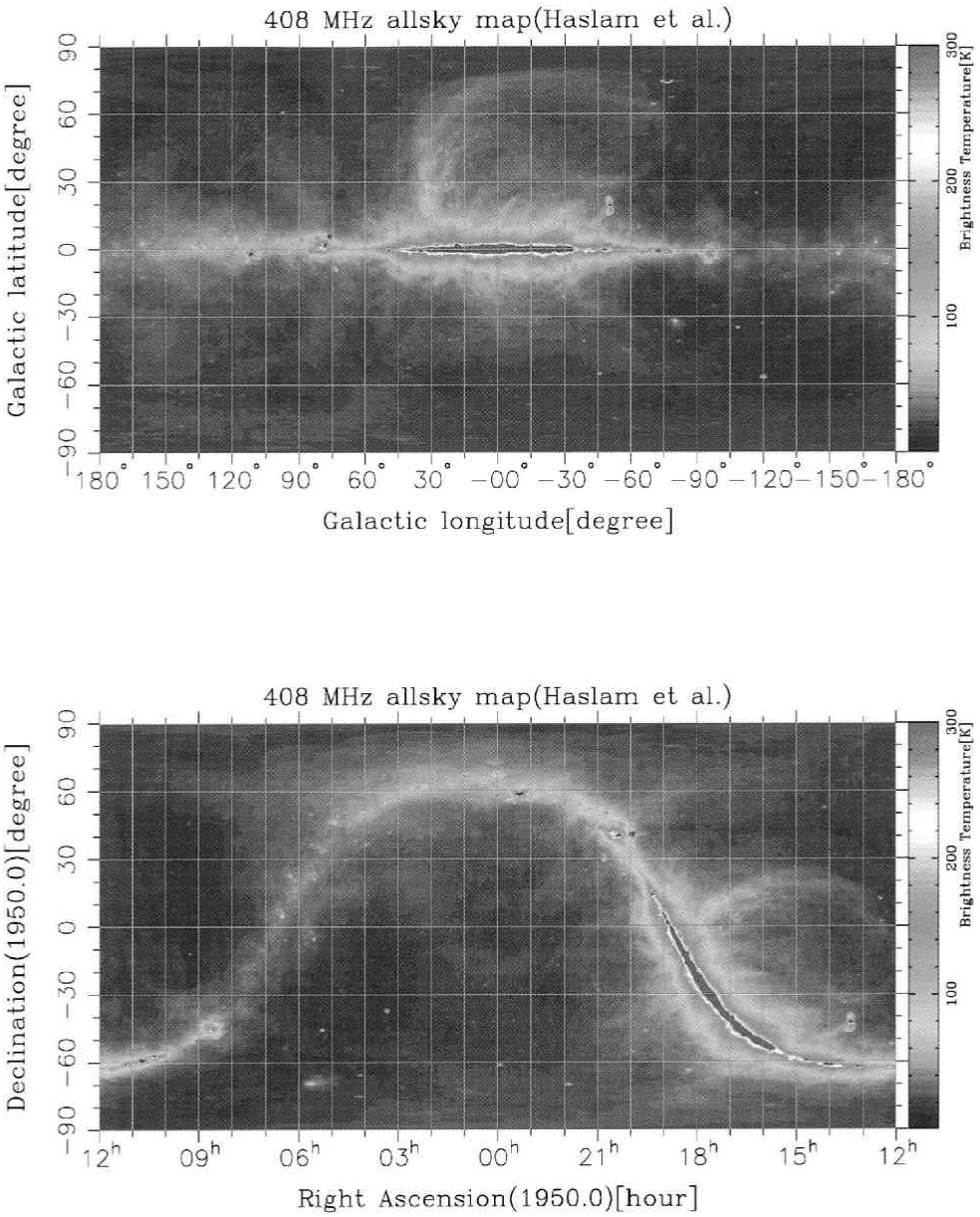

Fig. 32. The all sky map at 408 MHz in the galactic coordinate (top) and in the celestial coordinate (bottom) with angular resolution of 0.85° (Haslam *et al.*, 1982). The plotted data in digital is acquired from NASA's data center for Cosmic Microwave Background (CMB) research.
http://www.mpifr-bonn.mpg.de/survey.html

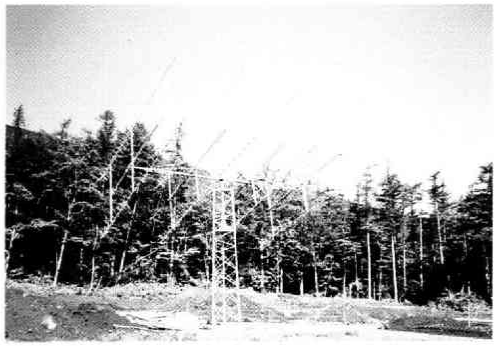

Fig. 35. Photo of an antenna unit. The type of the antenna unit is 4×2 stacked 27 elements cross YAGI antenna.

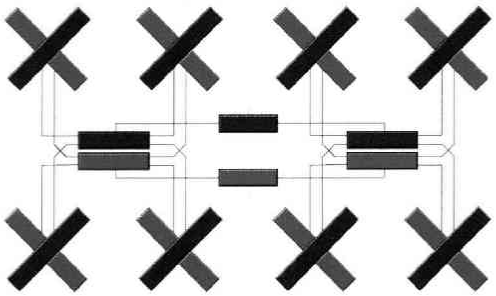

Fig. 38. Schematic plot of combination of signals from 8 pickup's. The signals from each pick-up are combined to one signal for each polarization. The pick-up's and combiners marked red are the signal unit for X polarization, and those marked blue are the signal unit for Y-polarization.

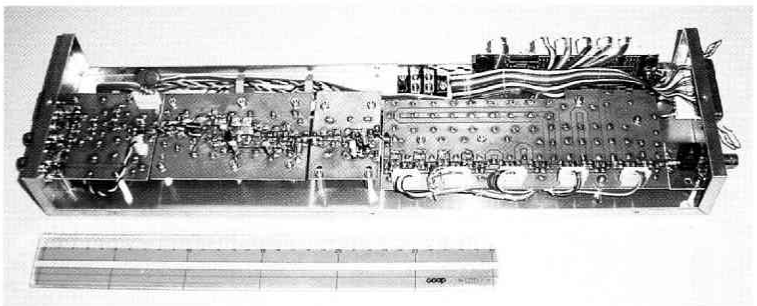

Fig. 40. Photo of the front-end unit. The signal flows from left to right through the (a) relay unit, (b) LNA unit, (c) programable attenuator unit, and (d) programable phase shifter unit.

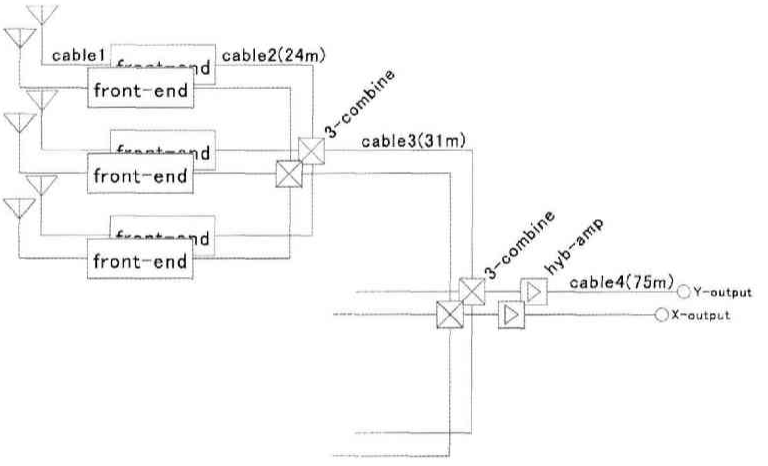

Fig. 46. Combination of signals from 9 antennas to a signal.

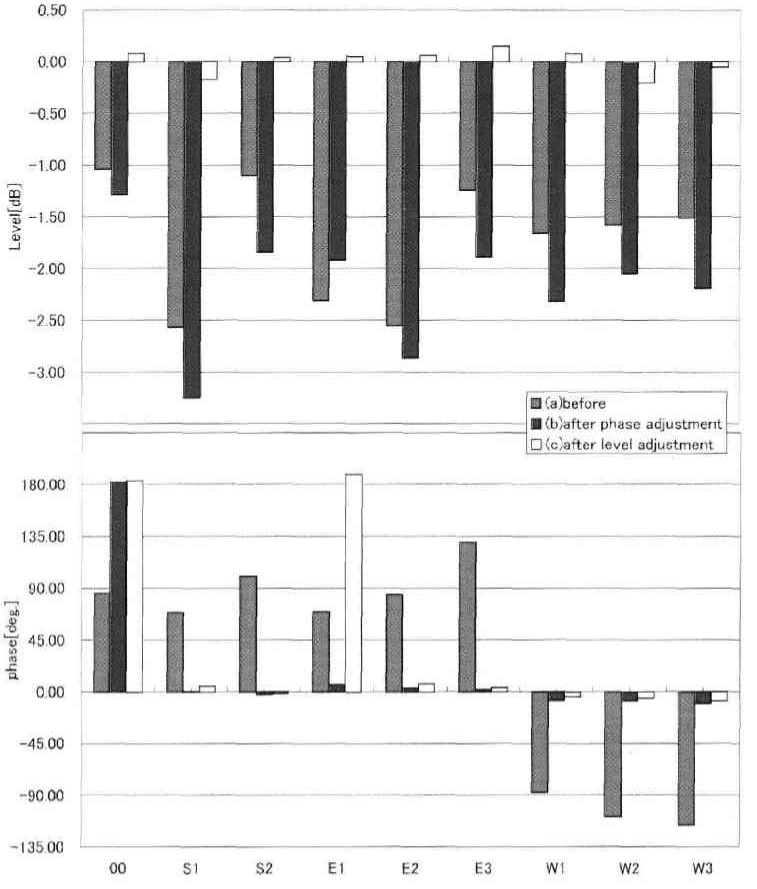

Fig. 52. Example of measurement of the loop-method for level (top) and phase (bottom) for three times ((a) before adjustments of phase and gain, (b) after only phase adjustment, and (c) after adjustments of phase and gain) in order to adjust phase and gain for all front-end units.

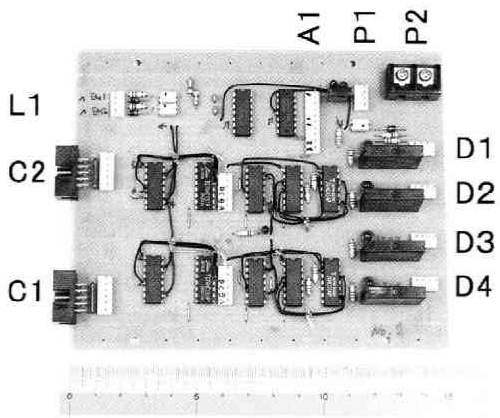

D1:Move CCW direction
D2:Move CW direction
D3:Move down direction
D4:Move up direction
C1:Control signal(elevation direction)
C2:Control signal(azimuth direction)
L1:limit signal
A1:anglar signal
P1:Power supply(DC 12V,5V)
P2:Power supply(AC100V)

Fig. 54. Photo of the antenna control unit.

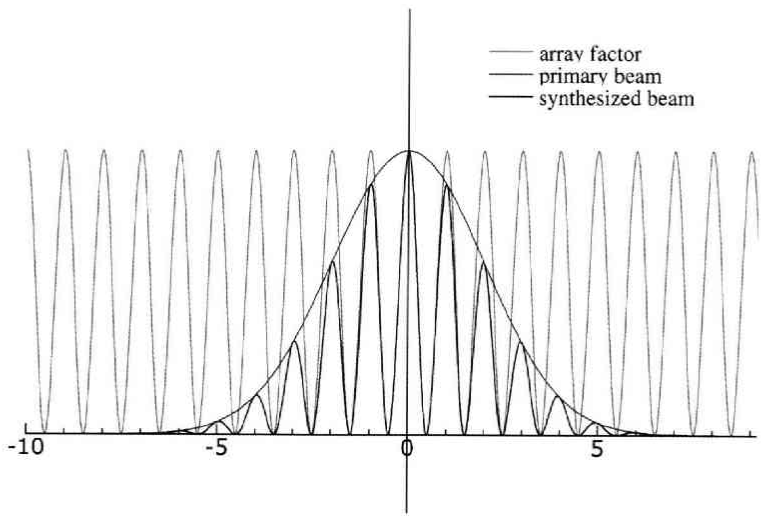

Fig. 58. Schematic plot of synthesized beam, primary beam, and array factor.

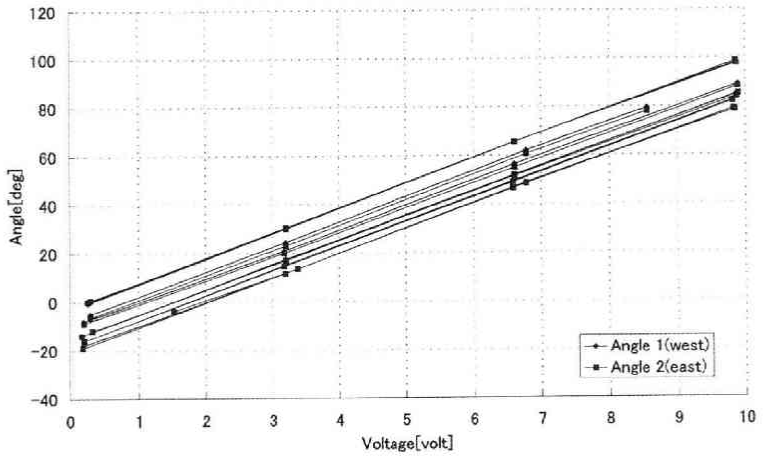

Fig. 60. Result of axial calibration for elevation. Relation between elevation angle and angular voltage is coordinated by linear function.

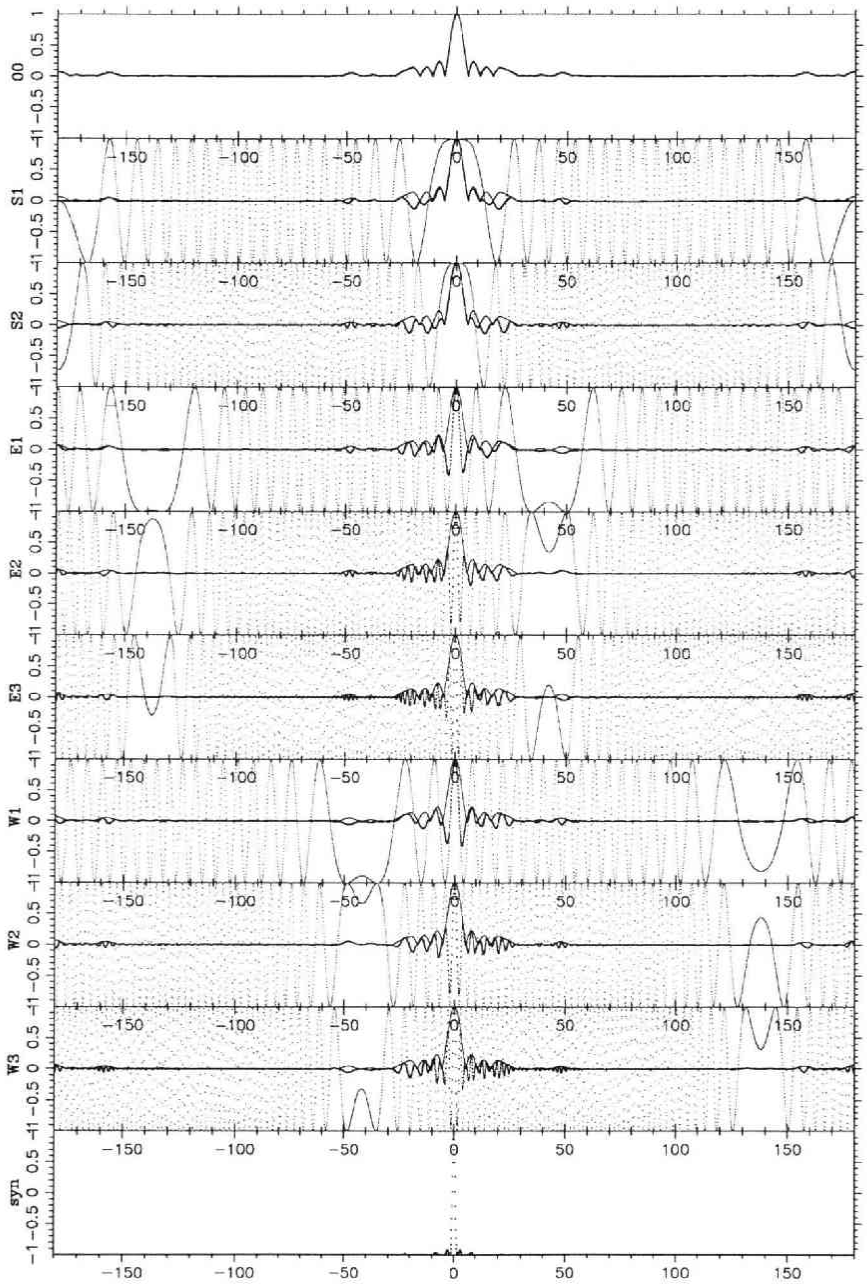

Fig. 65. Calculation of synthesized beam for azimuth direction at 45° elevation. The synthesized beam pattern is shown in the bottom panel. In the 1-9th panel, primary beam is shown by the red dots, array factor is shown by the blue dots, and products of primary beam and array factor is shown by the black dots which are real part of the electric field for each antenna.

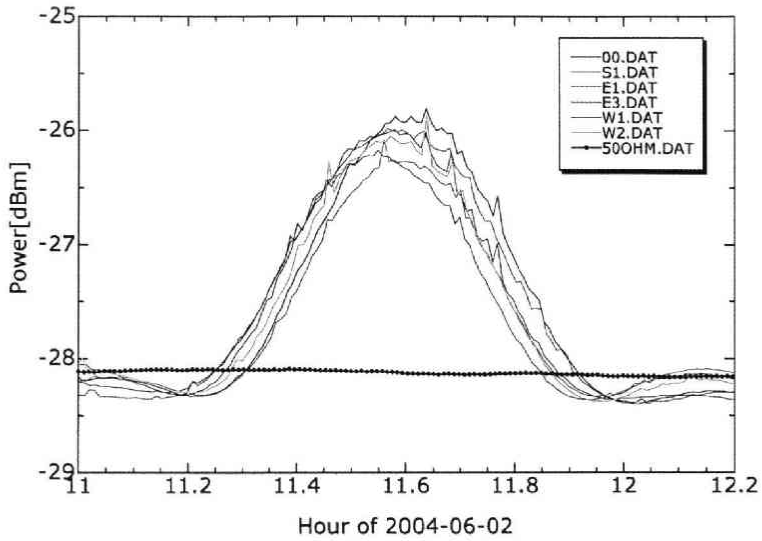

Fig. 71. The obtained data of the sun in order to measure the effective aperture area of one antenna.

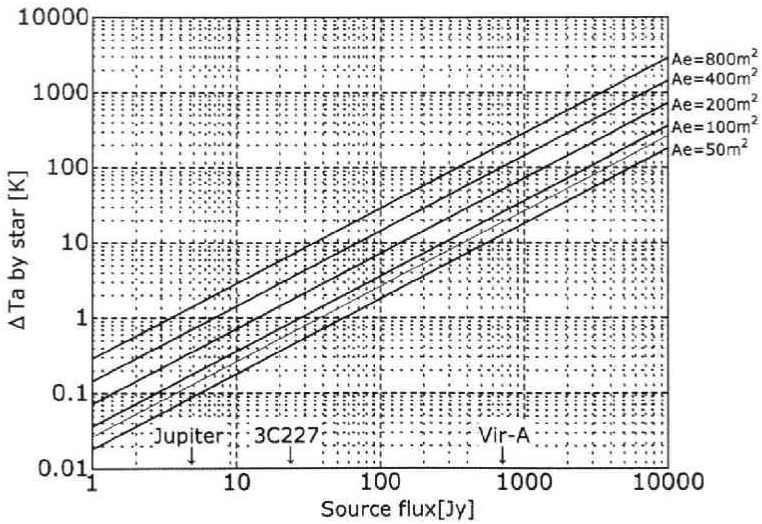

Fig. 76. The relationship between increase of antenna temperature (ΔT_a) and source flux (S) for the case of various effective antenna aperture areas (A_e) calculated from Equation (102). The red line is the case of A_e=72.2 m².

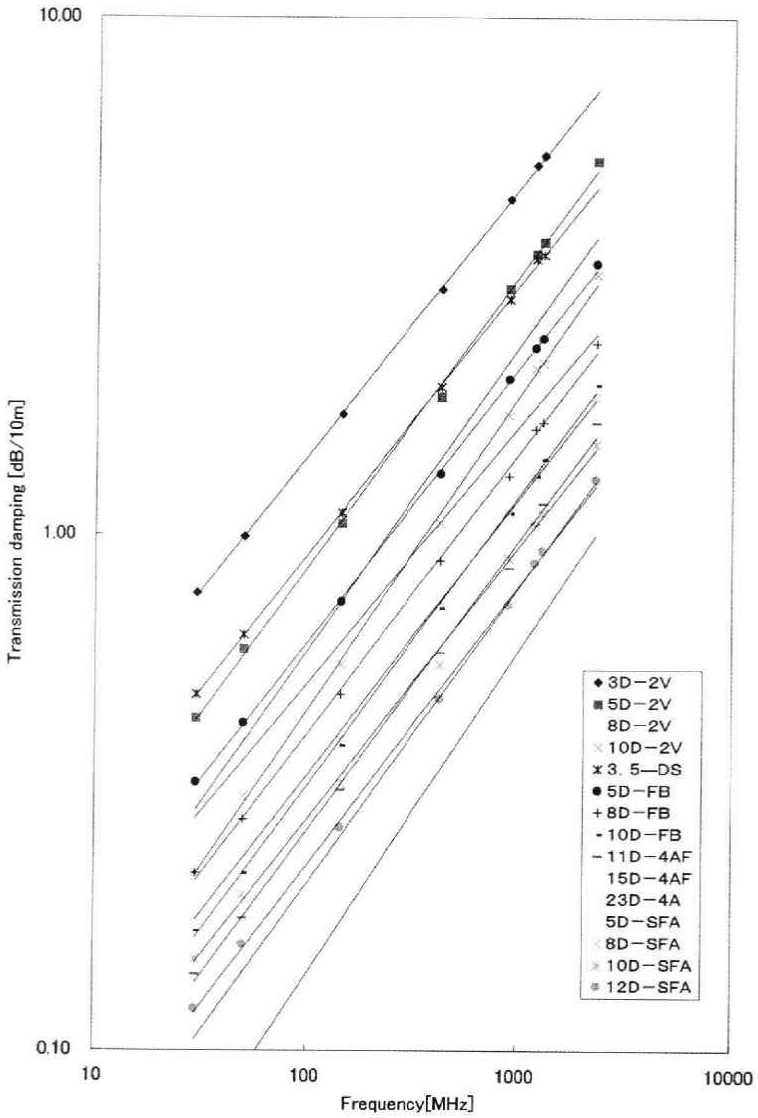

Fig. 79. Frequency dependence of cable loss in dB/10 m unit.

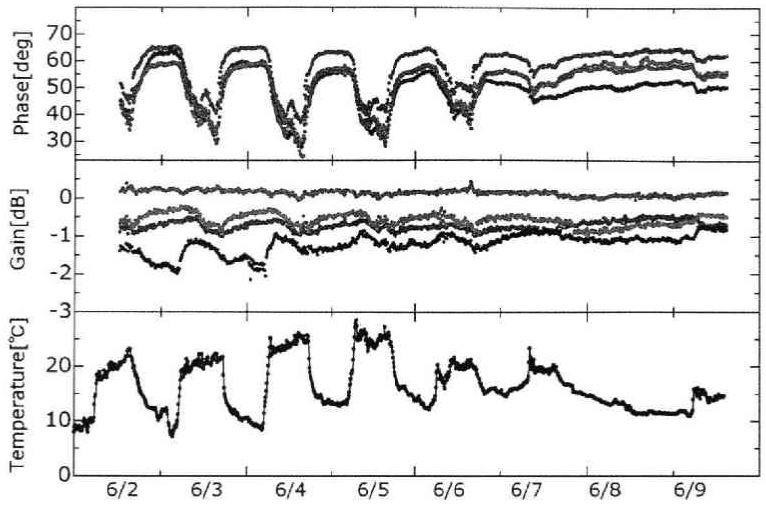

Fig. 87. The result of the system monitoring by loop-method during the period from June 2 to June 9, 2004. Phase (top) and gain (middle) measured by loop-method and ambient temperature (bottom) are shown as a function of time.